MULTIDISCIPLINARY INVESTIGATION OF SURFACE DEFORMATION ABOVE SALT DOMES IN HOUSTON, TEXAS

A Thesis

Presented to

the Faculty of the Department of Earth and Atmospheric Sciences

University of Houston

In Partial Fulfillment

of the Requirements for the Degree

Master of Science

By

Zheng Y. Huang

University of Houston

May 2012

MULTIDISCIPLINARY INVESTIGATION OF SURFACE DEFORMATION ABOVE SALT DOMES IN HOUSTON, TEXAS

Zheng Y. Huang

APPROVED:

Dr. Shuhab Khan, Chairman

Dr. Robert Stewart, Member

Dr. Ramesh Shrestha, Member

Dean Mark A. Smith, College of Natural Sciences and Mathematics

Acknowledgements

I am thankful to Dr. Shuhab Khan for his guidance and suggestions. I also wish to thank my committee members, Dr. Robert Stewart of Allied Geophysics Laboratory (AGL) and Dr. Shrestha Ramesh of National Center for Airborne Laser Mapping (NCALM), for allowing me to use key equipment necessary for completing this study. Many thanks to Dr. Joel Warneke and Texas Brine for allowing me access to the Pierce Junction site. Many thanks to Clifton S. Middleton the NGS representative of HGSD for important information about the GPS network and for supplying the GPS data. A great deal of thanks goes to Dr. Juan Fernandez for assistance in TLS field acquisitions. Many thanks to Michael Sartori and Abhinav Singhania for insightful talks. Also many thanks goes to all the members of the GeoRS team: Kivanc Biber, Shams Ul-Hadi, Ismail Abir, Yahaya Abu, Xu Han, Jessica Quintanar, Ayca Karacay, Kevin Schimdt, and Maisam Otoum for their support. Thanks to Dr. Veronica Sanchez for editorial comments.

I would like to thank my parents and in-laws for all their support and encouragement.

Last but not least an immeasurable amount of thanks go to my wife. Without her this would have all been meaningless.

MULTIDISCIPLINARY INVESTIGATION OF SURFACE DEFORMATION ABOVE SALT DOMES IN HOUSTON, TEXAS

An Abstract of a Thesis

Presented to

the Faculty of the Department of Earth and Atmospheric Sciences

University of Houston

In Partial Fulfillment

of the Requirements for the Degree

Master of Science

By

Zheng Y. Huang

University of Houston

May 2012

Abstract

Surface deformation has been an ongoing problem in the Houston Metropolitan area because of the city's location in a passive margin where faulting and subsidence are common. According to previous studies the causes of the surface deformation are typically attributed to anthropogenic activities, mainly the subsurface withdrawals of oil, gas, and groundwater. However, the majority of the studies done have not accounted for the vast amount of salt underneath the Houston area and its role in the surface deformation. The objective of this study was to identify areas of surface deformation in the greater Houston area and their possible relationship with subsurface salt movements. To accomplish this, I integrated three kinds of data: 1) GPS, 2) LiDAR (Airborne and TLS), and 3) Gravity. GPS data revealed subsidence and uplift in Harris County. DEMs generated from airborne LiDAR revealed changes between salt domes and their surrounding areas. TLS data collected over the Pierce Junction site, chosen for accessibility and depth, revealed vertical changes over the surface above the salt dome. Gravity data acquired over Pierce Junction salt dome also revealed changes in the subsurface. Groundwater withdrawal may be a large influence in the surface deformation of the Houston area, but salt-related surface deformation should be more closely studied to quantify its influence.

Chapter 1 **Introduction**

The Gulf of Mexico basin began forming in the late Triassic as an intracontinental extension within the North American plate (Salvador, 1991b). Enormous amounts of salt accumulated on the Gulf Coast during the late Triassic and Jurassic, followed by carbonate deposition during the late Jurassic and Cretaceous, and clastic deposits during the Cenozoic (Kupfer, 1974). Resting within this passive margin is the city of Houston, Texas. Houston, with a population of over 2 million (U.S. Census Bureau, 2010) is the largest city in Harris County. Harris County has a total population of over 4 million making it the largest county in Texas (U.S. Census Bureau, 2010). This large metropolitan city is approximately 80 kilometers from the Texas shoreline in a region where faulting (Verbeek, et al., 1979; O'Neill & Van Siclen, 1984; Shah & Lanning-Rush, 2005; Engelkemeir & Khan, 2008) and subsidence (Holzer & Gabyrsch, 1987; Coplin & Galloway, 1999; Zilkoski et al., 2003; Engelkemeir et al., 2010) are well-known problems. Subsidence and uplift for the purpose of this work refers to short-term surface deformation. Much of the historical subsidence in the greater Houston area has been attributed to extraction of subsurface oil and gas and more recently to groundwater withdrawal (Holzer, 1984; Coplin & Galloway, 1999; Zilkoski et al., 2003; Engelkemeir et al., 2010). These factors are known to cause subsidence, but many of these studies have over-looked one other factor, the vast amount of salt underneath the Houston area. Subsurface salt movements have played a large role on surface deformation in the Houston area. Almost 80% of the faults in the Houston area are directly above known salt domes (Norman & Howe, 2011). Many of these salt domes such as Pierce Junction, South Houston, Mykawa, Webster, Goose Creek, Humble, Lil Rich, Tomball, and

Hockley (Minor, 1925; Deussen & Lane, 1926; Deussen, 1934; Hanna, 1934; Teas, 1935; Eby, 1945; Murray, 1957) are well known due to oil and gas exploration (Figure 1.1).

1.1 General Geological Setting

Houston is located in the southeastern part of Texas. It is within the Houston Embayment along the Texas Gulf Coast on the northwestern edge of the Gulf of Mexico (Figure 1.2). The structural history of the Gulf of Mexico began in the Late Triassic with the breakup of the supercontinent Pangaea. As the North American plate moved away from the South American and African plates an intracontinental extension

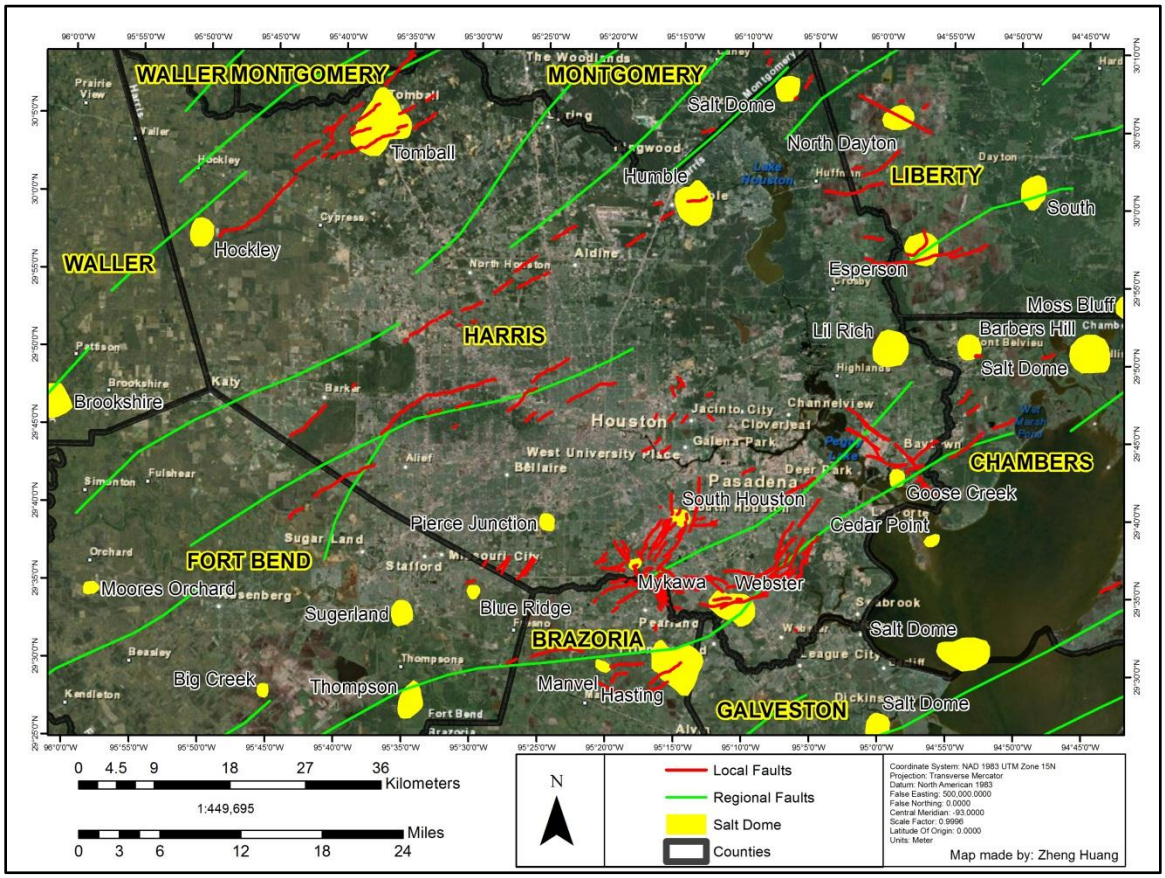

Figure 1.1: The Houston Metropolitan area within Harris County, Texas, USA. The red lines represent local faults (Brown et al., 1974; Verbeek & Clanton, 1978; White & Morton, 1997; Engelkemeir & Khan, 2008) and the green lines represent regional faults (Ewing & Lopez, 1991). The yellow polygons represent Gulf Coast salt domes (Huffman et al., 2004).

began within the North American plate (Walper, 1980; Salvador, 1987; Salvador, 1991b). This was followed by seafloor spreading throughout the Jurassic (Bird, et al., 2005). Presently the Gulf of Mexico Basin is roughly circular with a diameter of 1,500 kilometers, covers an area of approximately 1,500,000 square kilometers, and reaches 3,750 meters water depth in its abyssal plains (Ewing, 1991; Salvador, 1991a). The Gulf of Mexico has three major structural provinces: 1) The northwestern progradational margin, 2) the eastern carbonate margin, and 3) the western compressional margin (Ewing, 1991). For the purpose of this research only parts of the northwestern progradational margin will be discussed further. For more information on the margins please see Ewing (1991).

The northwestern progradational margin consists of two main zones: 1) the Interior Zone and 2) the Coastal Zone. The Interior Zone was created as a result of rifting, sedimentation, differential subsidence, and salt mobilization mainly during the Mesozoic. The Coastal Zone consists of mainly Upper Cretaceous and Cenozoic basinward progradational clastic wedges (Ewing, 1991). These two main zones contain three key structural provinces: 1) the San Marcos Arch, 2) the Rio Grande Embayment, and 3) the Houston Embayment (Figure 1.1) (Dodge & Posey, 1981).

The San Marcos Arch is a broad gently sloping platform extending southeast from Central Texas towards the Gulf of Mexico (Dodges and Posey, 1981). Three major fault zones cross the region: 1) the Balcones fault zone, 2) the Luling fault zone, and 3) the Kames fault zone (Ewing, 1991). All three fault zones strike southwest-northeast. The major fault zones of the San Marcos arch contain faults with displacements over 150 m making them the largest normal faults in south-central Texas (Fowler, 1956).

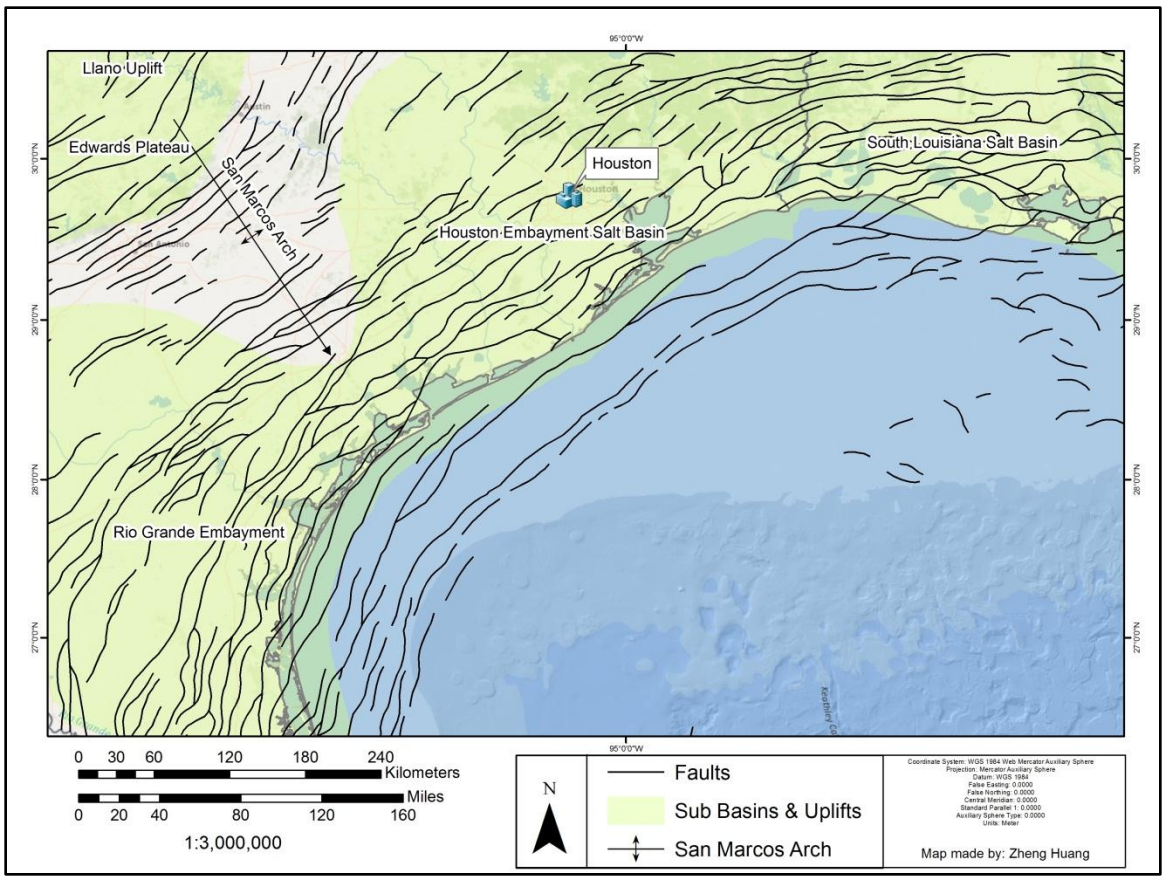

Figure 1.2: Texas Gulf Coast with northeast-southwest striking regional faults. Houston can be seen with in the Houston Embayment Salt Basin. To the southwest of the Houston Embayment are the San Marcos Arch and Rio Grande Embayment (Ewing & Lopez, 1991; Dodge & Posey, 1981).

To the southwest and northeast of the San Marcos Arch are the Rio Grande and Houston embayments. Each of the two embayments contains diapir provinces. The Rio Grande diapir province contains about 12 salt diapirs, while the Houston diapir province on the other hand contains many more, about 60, diapirs (Ewing, 1991). This diapir province is also known as the Houston Salt Basin, where Cenozoic deposits of over 12,000 meters accumulated (Pittman, 1994).

1.2 Salt Tectonics

Trusheim (1960) proposed two terms to describe salt movement: 1) halo-tectonism (deformation as a result of compressive tectonic forces) and 2) halokinesis (autonomous, isostatic salt movement). Halbouty (1979) adapted those terms to differentiate two types of salt basins. A salt basin is one controlled by halo-tectonism and a salt dome basin is one controlled by halokinesis. The Gulf Coast basin is categorized as a salt dome basin. Sediment loading due to progradation over a salt layer with no tectonic influence can create a variety to salt structures proximally and distally (Ge et al., 1997). These structures include salt anticlines, stocks, nappes, pillows, rollers, diapirs, detached diapirs, diapiric walls, extrusive domes, and salt glaciers (Figure 1.3) (Jackson & Talbot, 1986). In spite of the perplexing salt structures, the process of salt tectonics is simple. Salt moves horizontally from zones of higher load to zones of lower load (Hudec & Jackson, 2007). Differential loading of sediments and elevation differences produce differential loading zones. The Texas Gulf Coast salt structures can be attributed to regional extension and sedimentation (Jackson & Vendeville, 1994). Extensional events are responsible for most salt diapirism.

1.3 Subsidence and Monitoring

One of the most noticeable areas of subsidence is the San Jacinto Battleground State Historical Park along the coast approximately 32 km southeast of downtown Houston. Over 400,000 m^2 are now submerged by the Galveston Bay. Another example is the Brownwood subdivision in Baytown, Texas. This upper-income neighborhood was developed in 1938 along Galveston Bay. At the time the subdivision stood approximately

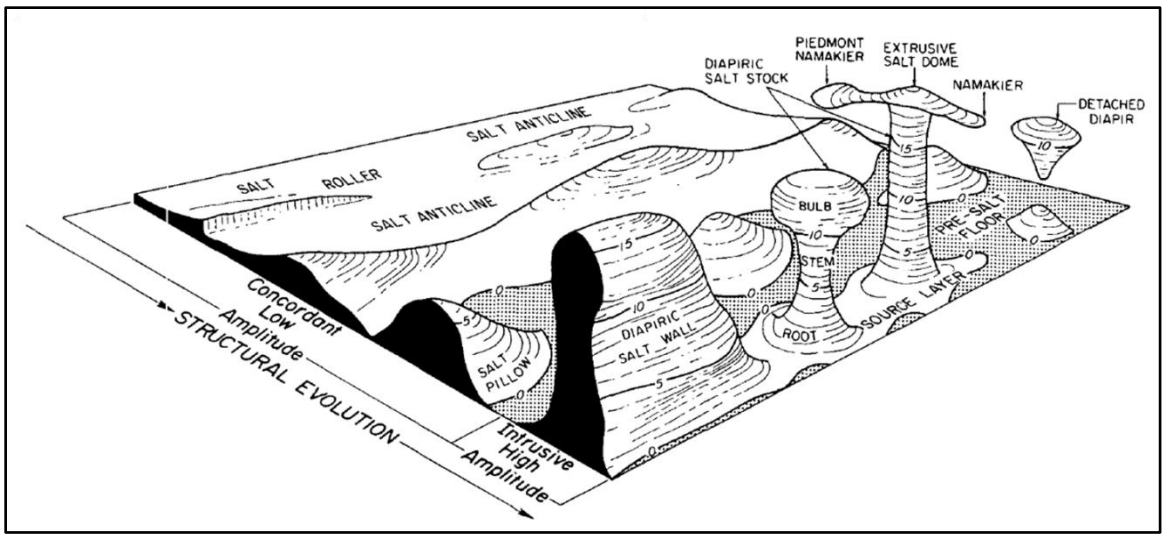

Figure 1.3: Salt structures displaying the evolution of salt tectonics (Jackson & Talbot, 1986).

3 m above sea level, but by 1978 it subsided more than 2 m. This large subsidence resulted in frequent flooding causing millions in property damage. In 1983 Hurricane Alicia delivered a final blow to Brownwood in the form of a 3 m storm surge. The entire 500 lot subdivision was abandoned and is now a swampy wetland (Coplin & Galloway, 1999).

To address this alarming subsidence problem, the Texas Legislature in 1975 commissioned the Harris-Galveston Subsidence District (HGSD) (Zilkoski, et al., 2003). The HGSD attacked the subsidence problem through regulation of groundwater withdrawal. A shift from groundwater withdrawal to using surface waters, like Lake Houston and Lake Livingston, calmed subsidence in the eastern parts of Houston and Galveston Bay (Coplin & Galloway, 1999).

Monitoring subsidence was first achieved through traditional differential leveling and borehole extensometers. These two methods were later replaced by a more cost-effective solution; this will be elaborated upon in Chapter 2.

1.4 Mechanisms for Surface Deformation

The main factors contributing to surface deformation in the greater Houston metropolitan area are faulting, subsidence, and salt tectonics to an unknown degree. Many studies have been done on faults and subsidence in this area (e.g. Verbeek et al., 1979; Holzer & Gabyrsch, 1987; Coplin & Galloway, 1999; Zilkoski et al., 2003; Campbell & Campbell, 2009; Engelkemeir et al., 2010). Some surface deformation may be natural, others may be anthropogenic, or a combination of both (Otoum, 2011). The influence of man in the extraction of subsurface fluids (oil, gas, and groundwater) may unbalance subsurface pore pressures within the strata, which may cause overburden strata to fault and subside. Natural geological processes such as the influence of buried progradational clastic wedges and salt tectonics may cause surface faulting and subsidence as well. All three of these elements affect surface deformation.

1.5 Objective

Influences on subsidence from groundwater and petroleum withdrawal are well documented. However, the roles of salt and salt domes have not been widely considered in the surface deformation of the Houston area. The objective of this work was to identify areas of surface deformation in the greater Houston area and their possible relationship with subsurface salt movements.

1.6 Scope

To accomplish the above, three kinds of data were integrated: 1) geodetic (Global Positioning System, GPS), 2) optical remote sensing (Light Detection And Ranging, LiDAR), and 3) gravity. GPS data along with digital elevation models (DEMs) generated

from airborne LiDAR for all of Harris County were used to identify changes in the rates of subsidence and their relationship to salt domes. Terrestrial Laser Scanner (TLS) (a form of ground base LiDAR) and gravity data were collected over the Pierce Junction salt dome to identify vertical changes over the surface above the salt dome as well as changes in the subsurface. The salt dome was chosen based on accessibility, depth, and safety.

Chapter 2 **Data and Methods**

The methods used to study surface deformation over the greater Houston area included field work, and analysis of GPS, airborne LiDAR DEMs, TLS, and gravity data.

2.1 Field Work

Field work was performed throughout the years of 2010 and 2011. Multiple salt dome locations where scouted and assessed for accessibility and safety. These factors were taken into account when selecting study sites. The dangers of working with the salt domes and the salt storage facilities were made very apparent when an explosion occurred about 50 km east of Houston in Mont Belvieu, Texas (Morris & Fowler, 2011). This happened only two weeks after the site was scouted for this study. This is a salt storage facility directly over the Barbers Hill salt dome which was the first considered site for this study.

2.2 GPS

2.2.1 Introduction

Global Positioning System (GPS) is a man-made constellation of 31active satellites that detects positions on the surface of the earth through triangulation and very accurate timing.

Before a subsidence monitoring GPS network was setup in the Houston area borehole extensometers and more than 2,500 National Geodetic Survey (NGS) benchmarks were set up. Traditional differential leveling of the 2,500 benchmarks cost over one million dollars. These benchmarks were first leveled in 1978 and re-leveled again in 1987. This method provided great spatial coverage of the subsiding area but

lacked high temporal resolution (Zilkoski et al., 2003). A system of continuous data was needed to properly monitor subsidence.

Borehole extensometers (Figure 2.1) were installed by the U.S. Geological Survey (USGS) in the early 1960s to measure subsidence. An extensometer consists of a deep well drilled to stable or relatively stable none compacting strata. Steel casing with slip-joints are installed along with an isolated inner pipe cemented to the base of the well. The slip-joints allow for compaction as the area subsides. The inner pipe extends to the top where measurements between the pipe and surface give the amount of subsidence.

Installing borehole extensometers addressed the temporal issue of subsidence monitoring but due to their high cost a spatial coverage was still lacking. Each unit costs over one million dollars. This greatly restricted their deployment to monitor subsidence (Zilkoski et al., 2003). In order to have both spatial and temporal coverage and still be cost effective, the GPS method was developed.

The Harris-Galveston Subsidence District (HGSD) in partnership with NGS employed a network of GPS stations called Periodically Active Monitors (Middleton, 2011 personal communication) formally known as Port-A-Measures (PAM) in conjunction with Continuously Operating Reference Station (CORS) to monitor subsidence (Zilkoski et al., 2003). GPS CORS units were affixed to the inner pipes of the Lake Houston (LKHU), Northeast (NETP), and Addicks (ADKS) extensometers to provide a relatively stable reference for processing baseline vectors for the PAM sites distributed throughout the greater Houston area (Zilkoski et al., 2003). The NGS software package Program for the Adjustment of GPS Ephemerides (PAGES) is used for processing. During the GPS processing the coordinates of the CORS sites are fixed to

compute the change in ellipsoid height of each PAM site relative to one CORS (Zilkoski, et al., 2003). This is repeated two more times with a total of three CORS each having their own measurements relative to all PAM sites. A weighted average is obtained and used as the final result for each corresponding PAM site.

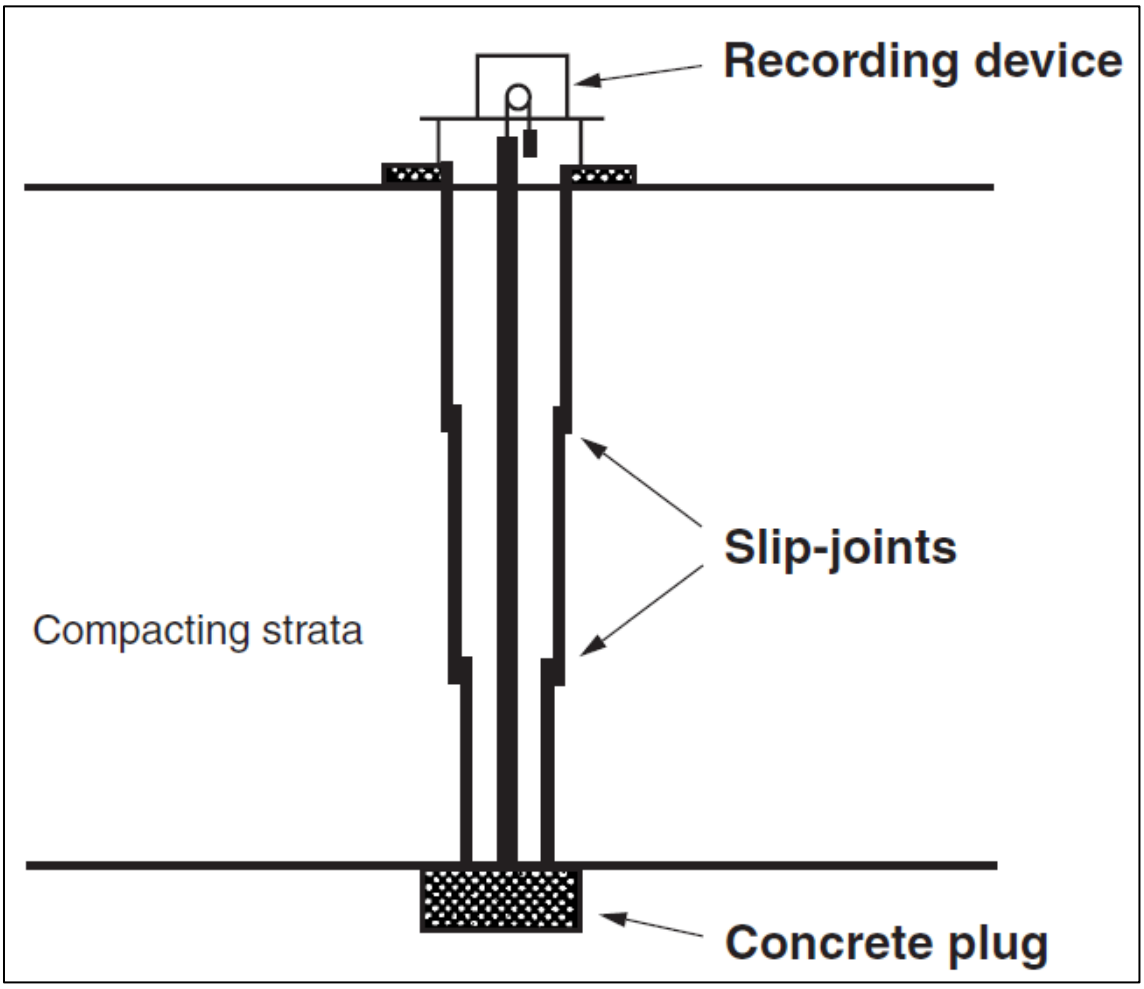

Figure 2.1: Illustration of borehole extensometer. The slip-joints isolate the inner pipe from the compaction of the surrounding strata. The inner pipe is cemented onto a concrete plug that is set into the Burkeville confining layer. This layer is believed to be stable. Displacement is recorded as the difference from the inner pipe to the slip-joint collar at the surface (Zilkoski, et al., 2003).

PAM monuments were designed to minimize the effects of the shrink-swell behavior of clay-rich soils in the area (Figure 2.2). These clay rich layers can extend up to

six meters below the surface. Vertical changes of up to nine centimeters over a period of a few days can occur due to expansion caused by moisture and temperature (Zilkoski et al., 2003). A six meter hole is drilled, in which a polyvinyl chloride (PVC) sleeve is cemented at depth and on the surface to stabilize the PVC. The PVC sleeve isolated the monument from the shrink-swell of the clay rich layers. A heavy wall galvanized pipe is cemented within the PVC sleeve and extended two and half meters above the surface (Zilkoski, et al., 2003). The PAM GPS antennas are placed on top of the galvanized pipe. Their locations were selected in areas away from salt domes and faults to avoid any localized effects that may skew the regional subsidence (Engelkemeir et al., 2010). At first PAM stations were housed in mobile trailers but later were converted to stationary lockboxes due to the cost and man power needed to maintain the trailers (Middleton, 2011 personal communication). One week of continuous static GPS data was originally collected at each PAM site with a monthly rotational schedule, but now this has changed to two months due to the number of PAM sites (Zilkoski et al., 2003; Lackey, 2011). Assuming the extensometers gave the absolute rates of subsidence, Zilkoski et al. (2003) demonstrated the PAM stations were comparable to the million dollar USGS installations (Figure 2.3).

2.2.2 Stability of LKHU, NETP, and ADKS

To see how stable the three extensometer CORS stations were, the Automatic Precise Positioning Service (APPS) (http://apps.gdgps.net) developed by the National Aeronautics and Space Administration's (NASA) Jet Propulsion Laboratory (JPL) was used. The APPS is a web-based application in which the GPS observation files are

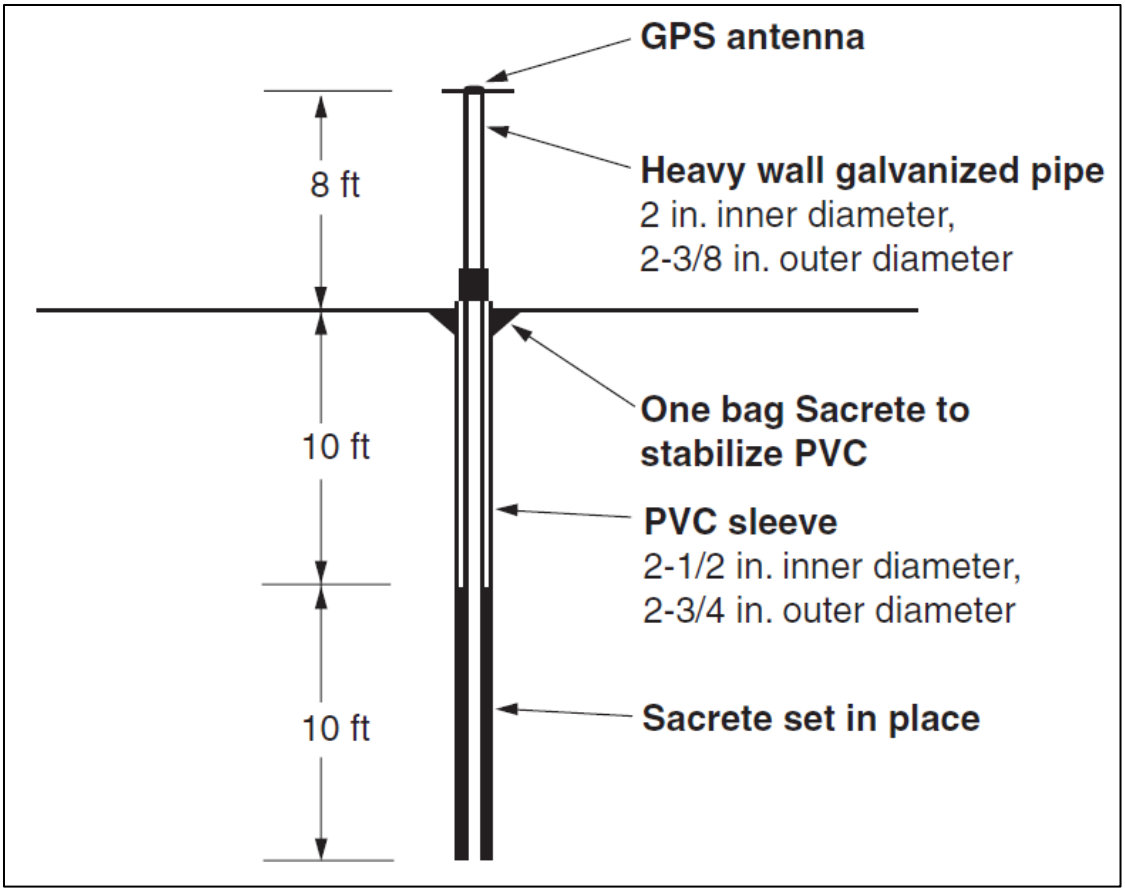

Figure 2.2: Illustration of PAM station. This design minimized the shrink-swell effects of clays in the upper few feet of the strata. Much like the borehole extensometer the PAM's inner pipe is isolated from the surroundings through a sleeve (Zilkoski et al., 2003). Sacrete is a type of ready mix concrete.

uploaded through a web browser and processed. The results are delivered to the user after processing is complete. The APPS is powered by JPL's GIPSY-OASIS software. This software uses a precise point positioning technique (PPP) which is independent of direct ground reference stations. The APPS use extremely precise satellite orbit and clock information to calculate the coordinates of a position (Jet Propulsion Laboratory, 2008). Ten years of data were submitted to APPS to see the stability of LKHU, NETP, and ADKS. The vertical displacements of the three CORS site were minimal (Figure 2.4) and appear suitable as reference stations for subsidence.

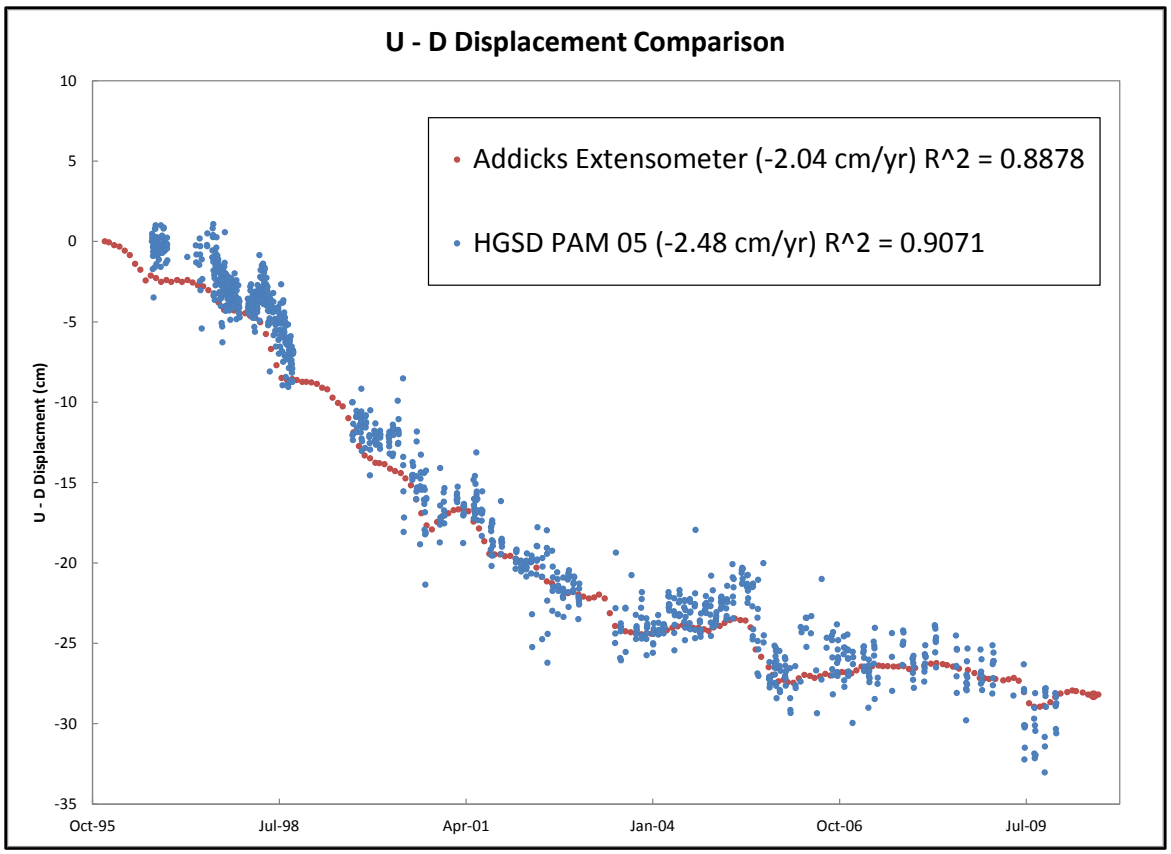

Figure 2.3: Co-plot of ADKS extensometer readings with PAM 05 spanning 13 years (1996-2009). The PAM GPS observations follow the extensometer measurements very closely. A larger scatter is seen starting from 2006 which may be due to antenna changes. It can clearly be seen that GPS results are comparable to the extensometer.

2.2.3 Online Positioning User Service (OPUS)

In 2001 OPUS was brought online by the NGS. It is a free, online, differential GPS post-processing application. OPUS provides highly accurate and reliable coordinates and removes the user's burden of processing GPS data (Wang & Soler, 2012). OPUS currently offers two services: 1) OPUS-S (static) accepts GPS observations longer than two hours and less than 48 hours and 2) OPUS-RS (rapid-static) accepts GPS observations longer than 15 minutes and less than two hours. For this study only the OPUS-S was used. GPS files uploaded with less than two hours of data were automatically detected by the application and processed using OPUS-RS, but results for

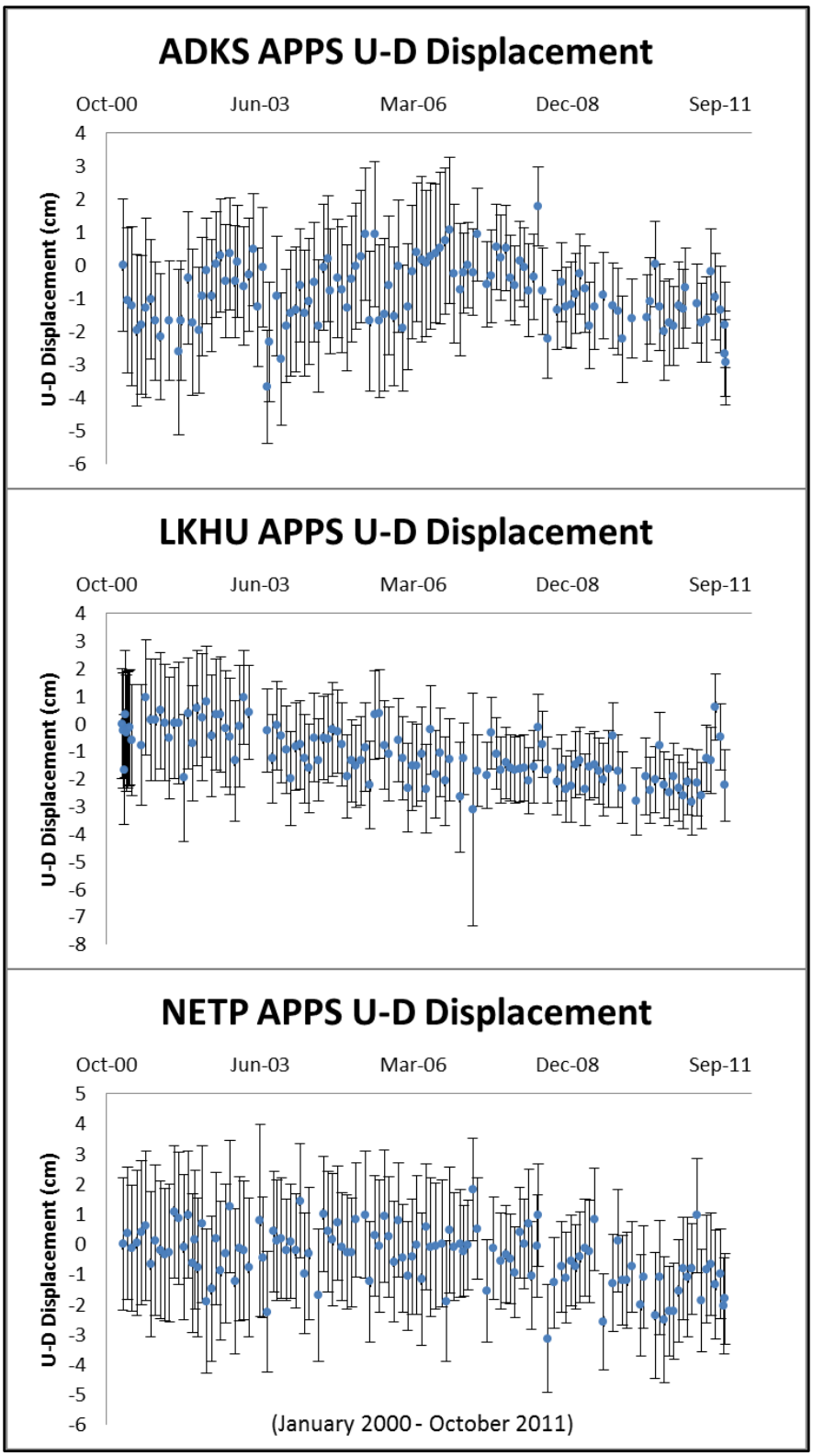

Figure 2.4: APPS result of ADKS, LKHU, and NETP vertical displacements. All three locations look stable in the vertical domain.

these solutions were ignored. At the heart of the OPUS application is the NGS software package Program for the Adjustment of GPS Ephemerides (PAGES). A dual frequency GPS observation file is submitted through the web application and in a few minutes OPUS returns an email containing positional coordinates of the processed observation relative to the national CORS network (National Geodetic Survey, 2012a).

2.2.4 Data Acquisition

All GPS observation files were downloaded from the HGSD File Transfer Protocol (FTP) site (ftp.subsidence.org) or acquired directly from the HGSD's NGS representative. The data from 2007 to 2011 were obtained from the FTP site in Trimble (T00 and T01) format. Data from 1993 to 2007 were obtained from the NGS representative in Receiver Independent Exchange (RINEX) format. The data consisted of a combination of PAM and CORS stations.

2.2.5 Data Preparation

To convert the Trimble proprietary files into RINEX format two tools were used: 1) Translate Edit Quality Control (TEQC) by the University Navstar Consortium (UNAVCO) and 2) Convert to RINEX – TBC Utility Version 2.1.1.0 by Trimble Navigation Limited (Figure 2.5). The RINEX files were grouped according to station number and antenna type. The files indicated that multiple antenna models were used including Trimble TRM39105, TRM41249, TRM55971, and TRM57917. Antenna TRM55971 was mistakenly reported on the observation file. Antenna TRM57917 was the real antenna (Middleton, 2011, personal communication). Due to the large number of files (over ten thousand), sorting station numbers and antenna types manually was not

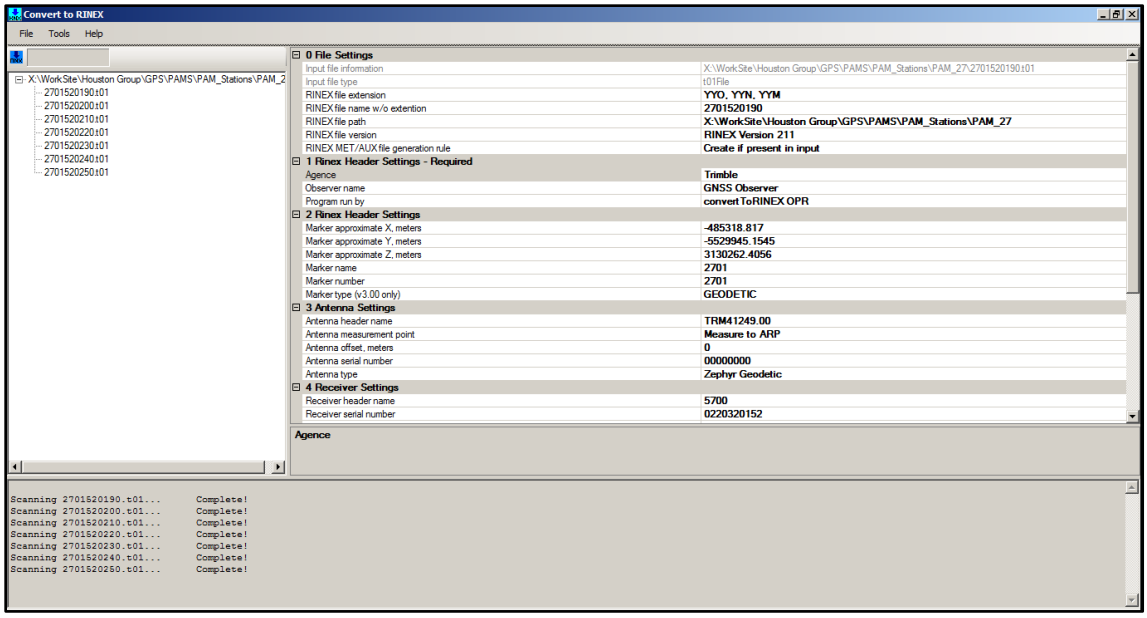

Figure 2.5: Trimble's Covert to RINEX utility. Header information such as antenna type, antenna header name, antenna measurement point, etc. can be viewed for each Trimble GPS file prior to conversion. After all emails containing the OPUS solutions were received they were exported to a single text file through Microsoft Outlook.

practical. To handle this task a script written in Python (a higher level programming language; www.python.org) was used to sort through these files. These sorted files were then zipped according to station number and antenna type using 7zip (www.7-zip.org).

2.2.6 Data Submission

Each zipped file was uploaded to the OPUS web application for processing. To receive the processed data an email account was setup through Gmail (www.gmail.com).

2.2.7 Data Extraction

An additional Python script was created to extract the northing, easting, NAD83 ellipsoid height, ellipsoid peak to peak values, the RINEX file name, start date, percentage of used observations, percentage of ambiguities fixed, root-mean-square (RMS), and the three CORS stations used for the solution. Peak-to-peak values are not

reported for the northing and easting coordinates so the peak to peak values from the NAD83 latitude and longitude were extracted to represent the peak to peak values. The data was compiled onto individual Excel sheets and plotted for each corresponding PAM site.

2.2.8 Data Error Analysis

The NGS has four guide lines for a successful OPUS solution: 1) 90 percent or greater of observations used, 2) 50 percent or greater of ambiguities fixed, 3) overall less than 3 cm RMS value, and 4) 5 cm or less peak to peak error in each component (Lazio, 2011; National Geodetic Survey, 2012b). OPUS solutions that did not meet these four criteria were considered to be errors. This is a general rule-of-thumb to assess the quality and precision of the OPUS solutions suggested by the NGS. This error analysis approach was applied to the data which removed 33 percent of the OPUS solutions. Upon visual inspection most of the removed points did not appear to be outliers. A different approach was evaluated for outlier removal. Similar to the approach by Firuzabadi and King (2011) and Wang and Soler (2012) the peak to peak value for each component (easting, northing, and ellipsoid height) was averaged. Any solution component containing a value three times the average was marked as an outlier. This approach removed less than ten percent of the points and appeared to more effective at removing real outliers (Figure 2.6). This method was used on all datasets.

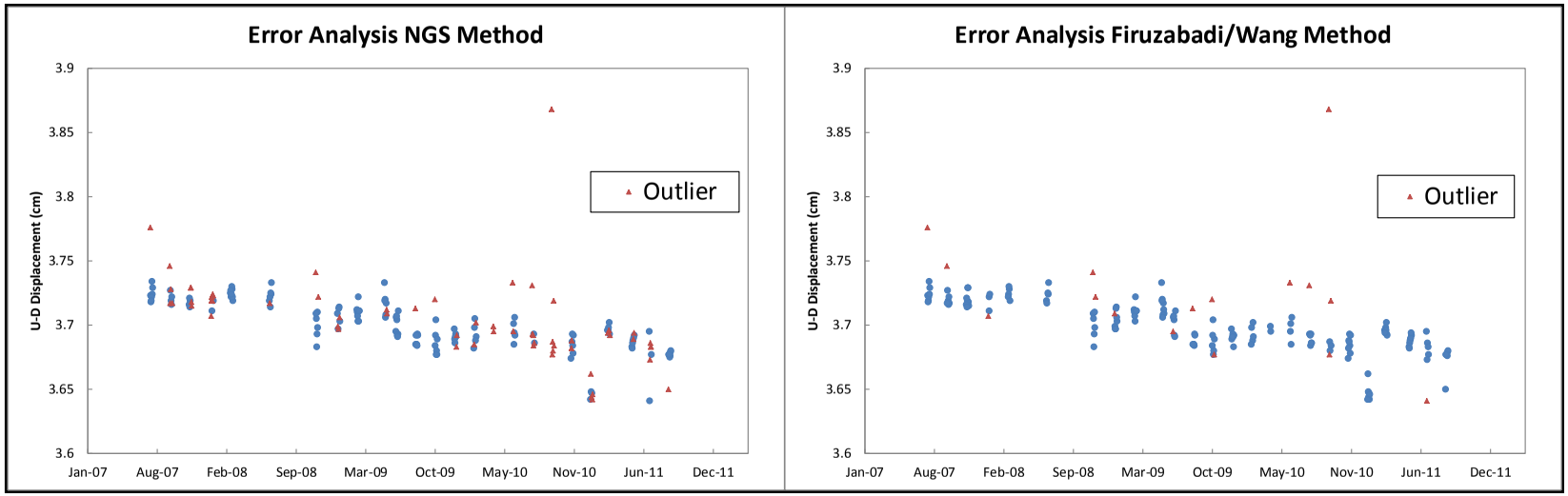

Figure 2.6: Two plots visualizing the results of the two error removal techniques. The NGS method removed outliers but also removed what appear to be valid GPS observations. The Firuzabadi/Wang method removed the same outliers as the NGS method but did not attack the valid GPS observations.

2.2.9 Surface Generation with ArcGIS

The GPS rates were analyzed and displayed in Environmental Sciences Research Institute's (ESRI) ArcGIS 10 software. ArcGIS was used to generate surface interpolations for the two (past and current) vertical rates. Three surfacing algorithms under the Spatial Analysis Tools were tested: 1) Inverse Distance Weighted (IDW), 2) Spline, and 3) Kriging (Figure 2.7). Ultimately Kriging was chosen because both IDW and Spline interpolated surfaces appeared much less representative of real surface deformation rates.

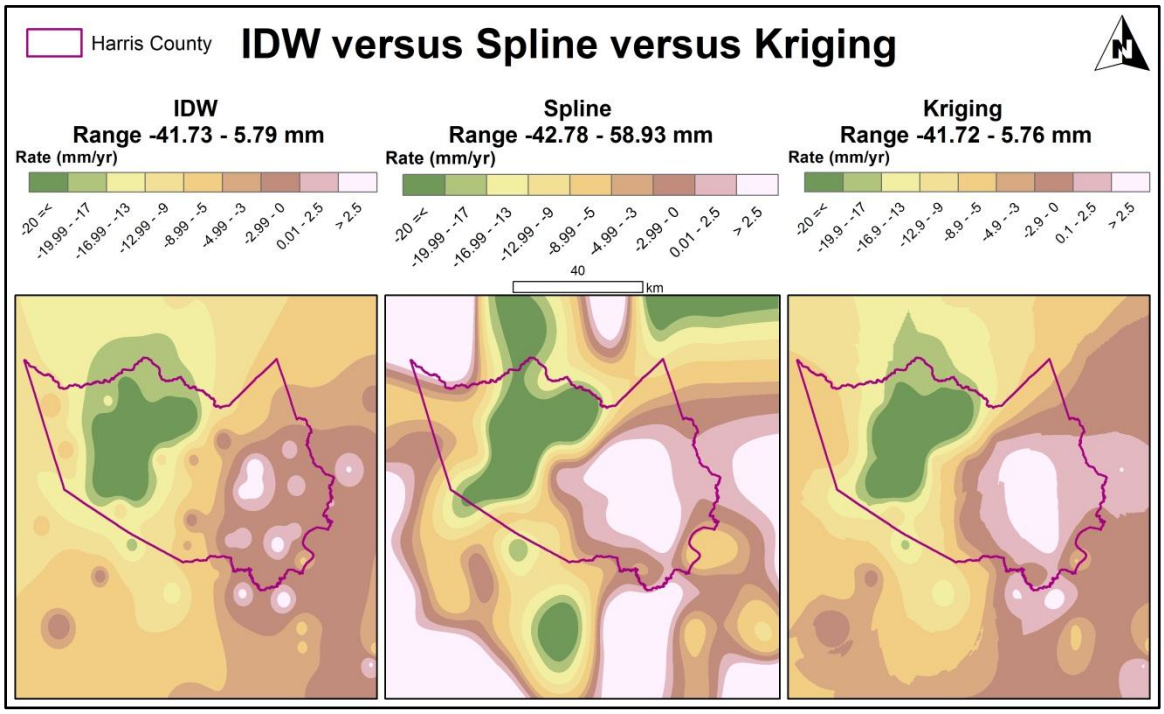

Figure 2.7: Comparison of three interpolations IDW, Spline, and Kriging. First upon visual inspection IDW appears to be plagued with bull eyes features. These features appear to represent the discrete GPS rates rather than generating a continuous surface. Spline's interpolation seems continuous and plausible, but the range goes way beyond the range of the input GPS rates which ranges from -41.73 – 5.84 mm. Kriging satisfies both the continuous surface and a range that is reasonable to that of the input.

2.3 LiDAR

2.3.1 Introduction

Light detection and ranging (LiDAR) is an active sensing system in which a laser beam is emitted towards the surface of the earth as the survey vehicle or aircraft navigates over a location (Fowler, 2001; Engelkemeir & Khan, 2008). LiDAR's main purpose is to measure distance. This can be done in one of three ways: 1) time-of-flight (TOF), 2) optical triangulation (OT), or 3) phase difference (PD). Each of these techniques has their pros and cons. Time-of-flight (or two-way travel time) gives highly accurate range measurements but the system must wait for the emitted pulse to return before the next pulse can be sent. This affects the collection speed at which a survey can be conducted. Optical triangulation, compared to TOF, has a higher data collection rate and accuracy. However, its higher accuracy is lost at greater ranges or when the scanned surface has a high degree of variability (Wehr & Lohr, 1999; Fernandez, 2007). Phase difference has the highest point collection rate of the three but is restricted by its uncertain range measurements. The most common type of ranging LiDAR is TOF (Fernandez, 2007).

A LiDAR scanner can be divided into four main units: 1) laser ranging unit, 2) opto-mechanical scanner, 3) control unit, and 4) processing unit (Wehr & Lohr, 1999). As mentioned before, the laser ranging unit only measures range. In order to have a position for the return pulse a position and orientation system (POS) is needed for the platform on which the LiDAR is emitting from. The POS is an integration of high precision GPS and Inertial Measuring Unit (IMU) (Shrestha et al., 1999). The

amalgamation of all these elements produces an unique X, Y, and Z position for each point (Wehr & Lohr, 1999).

Once acquired, raw LiDAR data is saved as ASCII text files or more recently as LAS binary files. These files are displayed as point clouds. LAS files are now the industry standard for LiDAR data. For terrain analysis the points are filtered and classified to ground and non-ground points based on returns. Last returns are presumed to be the ground features and first returns to be top features. These top features can be trees, building, bridges, and anything else that may be on the surface. This automated filtering can be done through software such as TerraScan and MARS but the classifications are not always 100 percent correct. It takes a skilled and experienced analyst to determine the source of errors.

A Digital Elevation Model (DEM) is most commonly the end product of a LiDAR point cloud. Conversion to a DEM is done by creating a Triangulated Irregular Network (TIN) from the filtered ground points. A TIN is preferred because the space between each point is extrapolated leaving fewer holes in the data. The TIN is then interpolated to produce a DEM (Engelkemeir & Khan, 2008). A DEM is a raster with equally spaced horizontal and vertical cells which contain elevation data. Geomorphological studies using LiDAR-generated DEMs (White & Wang, 2003; Pepe & Coutu, 2008; Sasaki et al., 2008) have been used largely in coastline studies and natural hazard assessments.

2.3.2 Houston Airborne LiDAR Data

There are three sets of LiDAR data for Houston: 1996, 2001, and 2008. The 1996 and 2001 data sets were collected by Terrapoint LLC with horizontal accuracies of ±0.75

m and vertical accuracies of ±15 cm. The North American 1983 HARN (NAD83 HARN) was used as the horizontal datum and the North American Vertical Datum (NAVD) 1988 was used for the vertical datum. HARN is an abbreviation for high accuracy reference network. Merrick & Company collected the 2008 data with horizontal accuracy of ±0.7 m and vertical accuracy ±9.25 cm. The Federal Emergency Management Agency (FEMA) and the Harris County Flood Control District (HCFCD) funded the 2001 data acquisition as part of the Tropical Storm Allison Recovery Project (TSARP) (Meyer, 2002). The 2008 data was commissioned by the Houston-Galveston Area Council and the Geographic Data Committee. These surveys were conducted as part of a flood hazard mapping program.

Each section of LiDAR data has a corresponding Digital Elevation Model (DEM) created. The resolutions of the DEMs are 3 by 3 meters (1996 and 2001) and 1.5 by 1.5 meters (2008). Engelkemeir (2008) noted that some artifacts still remained in the DEMs (Figure 2.8).

2.3.2.1 DEM Height Computation

The polygon technique used by Engelkemeir (2008) was employed to examine changes between the center of the salt dome relative to its surround areas. For each polygon the average elevation within is assumed to provide an acceptable measure of the elevation (Engelkemeir, 2008). Five polygons were created for each salt dome location. Four outside polygons surround the salt dome on the north, south, east, and west. One polygon was created within the area of the salt dome. The polygons were created to avoid artifacts within the DEM.

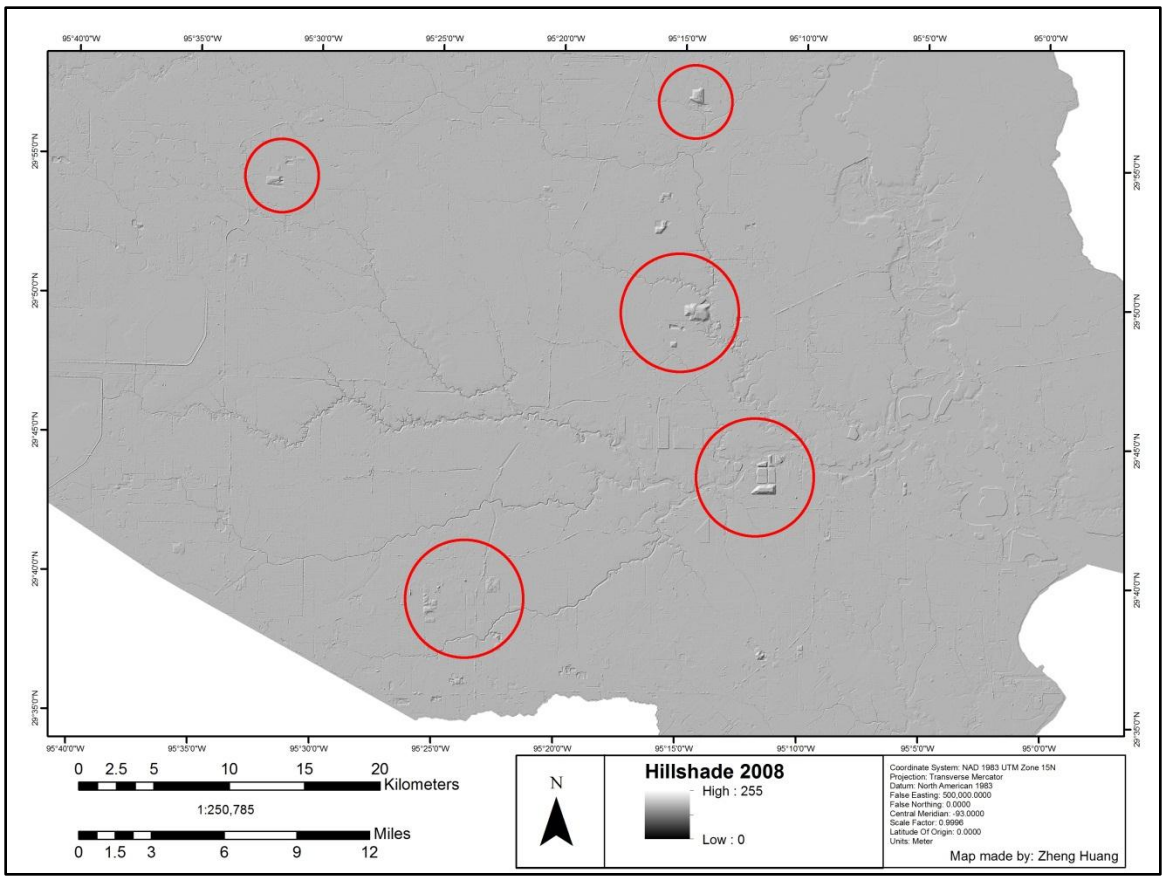

Figure 2.8: Hillshade of 2008 DEM of Harris County. Circled in red are the anomalies noticed in the hillshade image. These anomalies were present in the 1996 and 2001 DEM as well.

This method involved similar steps to Engelkemeir's (2008) polygon method but did not involve the custom tools created by Engelkemeir (2008) for generating a polygon dataset. The scale at which those polygons were created would not be adequate for the purpose of this study due to the larger area needed to be covered. Another approach was taken to create the polygons and is described below.

First ESRI ArcGIS 10's Create Fishnet (Data Management) tool was used to create 250 m evenly spaced polygons for the entire Harris County. The locations of the salt domes were overlain on top of the fishnet (Figure 2.9). Next, a workflow was followed for each salt dome location (Figure 2.10). Using the selection tool, polygons

within the salt dome areas were selected. Four groups of polygons were selected from the north, south, east, and west of the salt domes. Selection of the polygons was essential. Selection was done to avoid DEM artifacts, streams, streets, and large building foot prints. After each selection was made, the selected features were exported from the whole fishnet into a subset polygon shapefile. Within this subset an attribute field named Zone was created. Zone was used to distinguish each features category. The categories set consisted of the name of the salt dome followed by Center (for areas within the salt dome shapefile), North, South, East, and West. After each zone was properly categorized the Dissolve (Data Management) tool was used to aggregate all individual features with the same categories into one feature. For example, all 19 individual features that shared the Pierce Junction Center category were dissolved into one feature named Pierce Junction Center. Zonal Statistics as Table (Spatial Analyst) was used in combination with the newly dissolved shapefile to extract statistics from the DEM. The Zonal Statistics tool calculates area, min, max, range, mean, standard deviation, and sum. An attribute field was created for each calculation and stored as a table. The Zonal Statistics table was then joined to the dissolved shapefile for visual display purposes.

2.3.3 Terrestrial Laser Scanners

Terrestrial Laser Scanners (TLS) are composed of two main parts. The first is the LiDAR unit. The second is the opto-mechanical device capable of steering the laser beam to perform the scan of an area (Fernandez, 2007). TLS surveys are mostly dependent on the operator's experience and the objectives of the survey. There are no design or data collection procedures. Designing a collection begins with accessibility to the region of

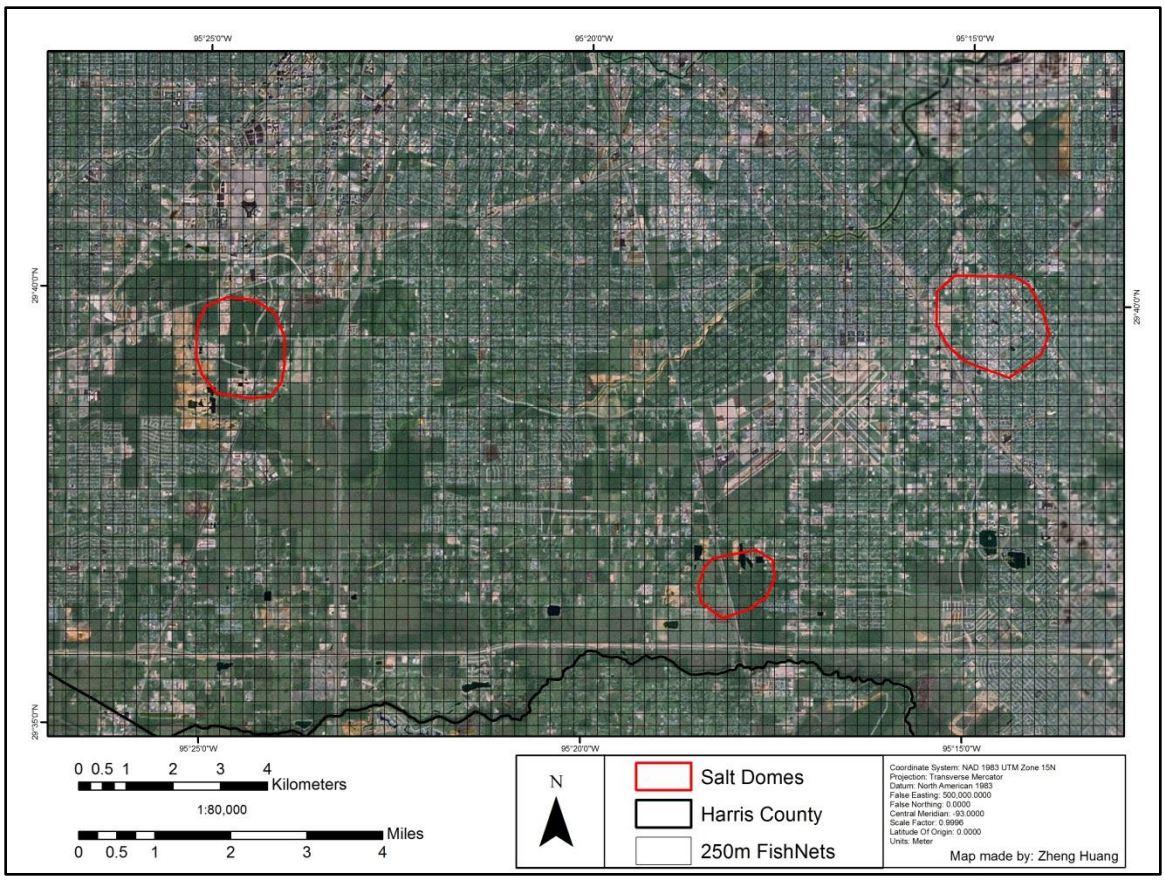

Figure 2.9: Result of the Create Fishnet tool. It created an evenly spaced 250m by 250m grid for Harris County. In this image only the south side of Harris County is displayed because the individual cells are not distinguishable at the extent of the entire county. The surface locations of Pierce Junction, Mykawa, and South Houston salt domes are highlighted in red.

interest (ROI) followed by the purpose of the collection and the desired resolution (resolution can be angular resolution or laser point spacing). Reference of the data set would also need to be considered. The operator decides (depending on the objective) whether the collection should be in the native sensor XYZ or a geodetic coordinate frame. These parameters will help the operator design the scan orientations and reference frame of the data acquisition (Fernandez, 2007).

2.3.3.1 Data Collection

The objective of the Houston salt dome scans was to look for vertical changes of

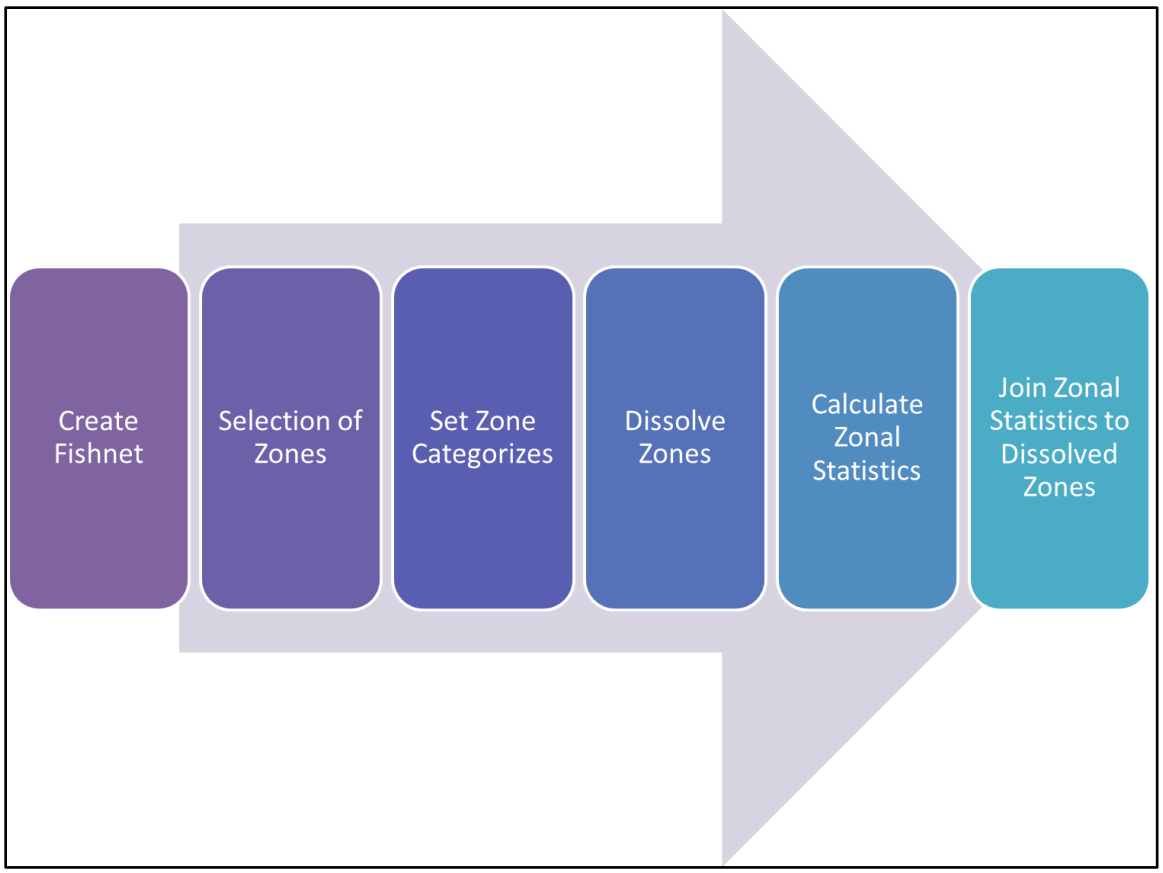

Figure 2.10: Flowchart displaying the process of creating zones and calculating statistics for polygon analysis.

the surfaces above the salt domes over time. For this purpose the data collection was designed with a geodetic coordinate frame. The geodetic coordinate frame gives spatial location to the point cloud which can be analyzed over time for vertical changes in the ROI. The scan orientation was set to one position with a 360^0 scan because one continuous scan will reduce dataset merging errors. The desired point spacing was below 10 cm.

The locations for this study were selected based on accessibility and depth. Pierce Junction (- 229 m), South Houston (-1,280 m), and Webster (-3,109 m). Two TLS units were used: 1) Optech Intelligent Laser Ranging and Imaging System (ILRIS) 3D and 2)

Riegl VZ-400 (Figure 2.11). Two different units were used because the first (Optech) malfunctioned and needed repairs.

The Optech ILRIS 3D consist of a 3 megapixel built-in camera, LCD viewfinder, eye safe class 1 laser (infrared), and a range of 3 m to beyond 1 km (http://www.optech.ca/i3dfeat-ilris.htm). It has a single 40^o x 40^o instantaneous field of view. An optional pan-and-tilt base extends the system to a full 360^o with no loss to accuracy (Optech Inc., 2006).

The Riegl VZ-400 consists of a 12.3 megapixel attachable camera (Nikon D300), human machine interface (HMI), eye safe class 1 laser (near infrared), and a range up to 600 m. It has a 100^o x 360^o field of view (Riegl Laser Measurement Systems, 2011).

The Optech proprietary software Controller was used to perform the data collection. The software displays a digital image through the LCD viewfinder which can be seen also through the Controller's main screen. This display is the 40^o x 40^o scan area or (if the pan-and-tilt base is attached) a 360^o panoramic image consisting of ten overlapping frames in 40^o increments. Before starting the scan, a ROI is selected and an initial range acquisition is conducted to point spacing in linear or angular units (Fernandez, 2007).

The three scan locations were above known salt domes. Scans were conducted at all three locations but only one location was selected for a repeat scan due to accessibility, safety, and environmental factors. GPS data for geo-referencing were taken using Trimble Zephyr Geodetic with GP, Ashtech Marine Rev C, and Ashtech Choke Ring – without Radome antennas. The GPS receivers used were Trimble 5700 and Ashtech Z-Extreme.

Figure 2.11: a) The Optech ILRIS 3D with external batteries, operator, and, pan-and-tilt base for full 360^{o} scanning. b) The Riegl VZ-400 with attachable camera, GPS antenna, and external batteries.

2.3.3.2 Data Extraction

The Optech ILRIS 3D stores collected data, with full sensor orientation factors and range for each return, in binary format. To extract and convert the binary data the Optech proprietary software Parser is used. Parser turns the binary data into 3D positional points set in the sensor XYZ frame of reference. During this parsing process additional information, such as intensity and RGB, can be extracted. Parser can export in a variety of formats that can be recognized by most LiDAR processing software for more analysis, manipulation, and information extraction. Information extraction is the main purpose of the TLS scan (Fernandez, 2007).

The following data processing steps were modeled after Fernandez (2007).The first step after the parsing phase was to geo-reference the point cloud. Five GPS control stations were positioned. XYZ, Easting, Northing, and Height coordinates were obtained for the control points using a combination of PolyWork's IMInspect and TerraScan. The GPS locations were identified within the point cloud and cropped in TerraScan to make it easier to manipulate in the software. The cropped GPS locations from which center points were imported into PolyWorks (Figure 2.12). After obtaining XYZ locations of the center points a Matlab script developed by Fernandez (2007) was utilized to calculate the center point of the spheres (Figure 2.13). Using the calculated centers and GPS measurements of the locations a 3D solid rotation and translation transformation was computed with NAD83 as the horizontal datum and NAVD88 as the vertical datum. Next, all undesired points (cars, people, and other objects outside of the ROI) were cropped using TerraScan (Figure 2.14). Lastly, 10 cm spacing grids were created using ArcGIS 10. 10 cm was chosen because it is larger than the desired point spacing. This will ensure each cell within the grid will have at least one TLS data point.

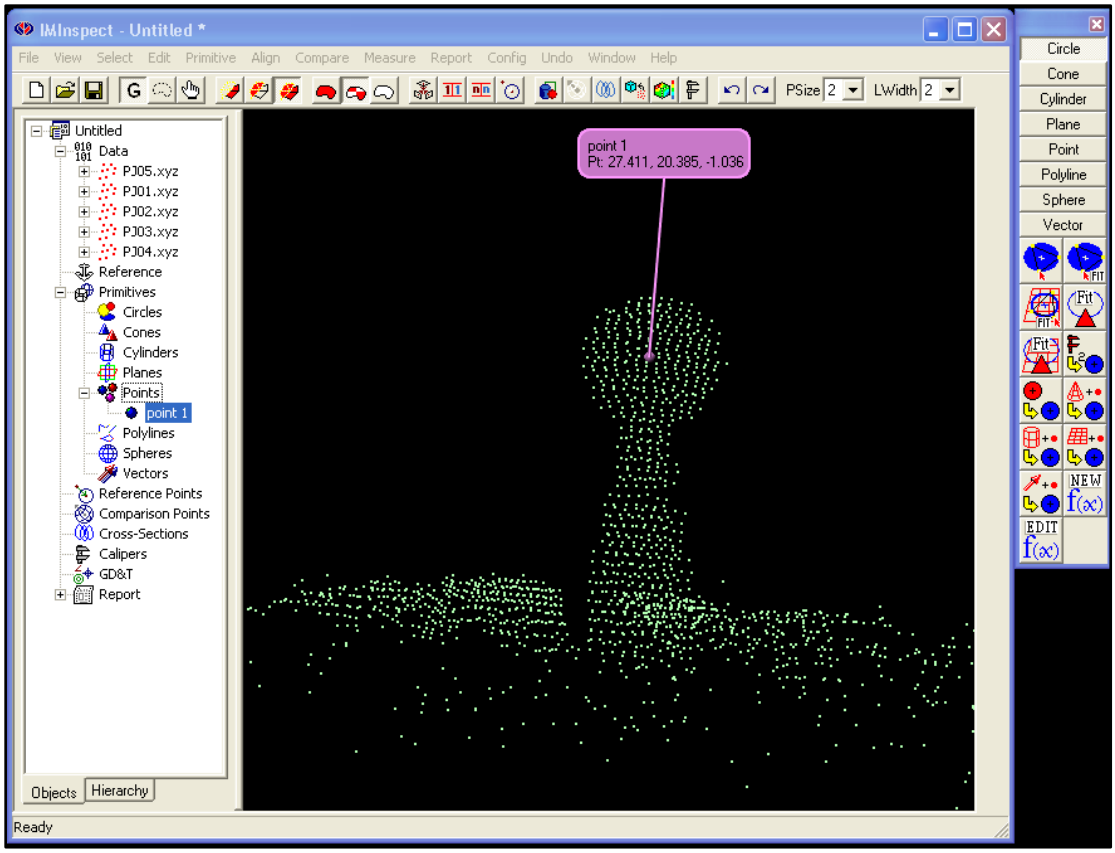

Figure 2.12: Center point extracted from surface of sphere using IMInspect.

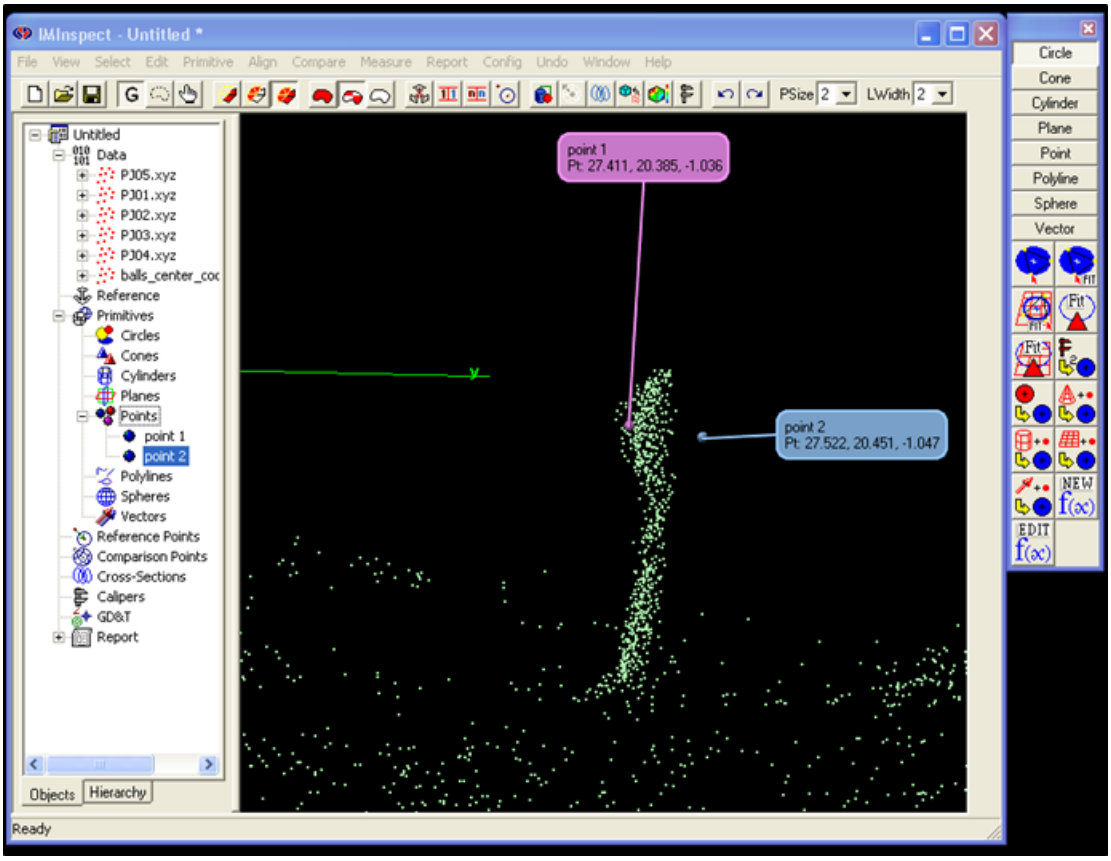

Figure 2.13: Center point of sphere after running Matlab script to calculate the center points of the sphere.

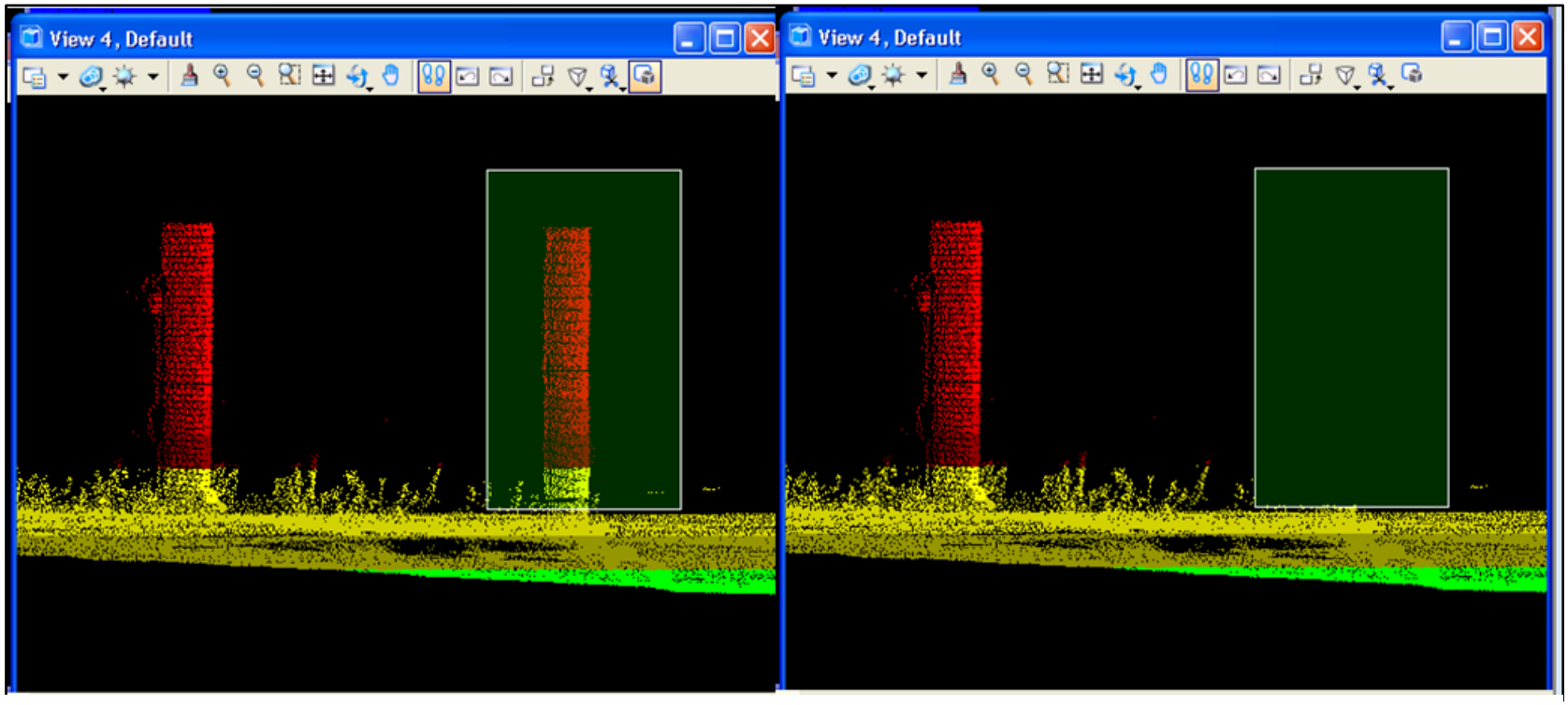

Figure 2.14: TerraScan cross section over a small portion of the South Houston salt dome TLS scan. On the left a fence is drawn around an area of undesired points. On the right shows the undesired points removed. This was done to all the TLS data to remove none surface features such as trees, cars, pedestrian, and other objects.

2.4 Gravity

2.4.1 Introduction

Gravity is the attraction between two masses. Newton's law of gravitation states that every point mass has an attraction to all other point masses, which means that the attraction between the point masses is proportional to the product of their masses and to one over the square of the distance between them. Newton's second law states that acceleration is proportional to force. When measuring gravity, gravitational acceleration is what is actually measured. Gravitational acceleration is the rate of change of a body's speed under the influence of the gravitational force. This translates into the geoscience domain in the form of density. Density is mass per unit volume. When an object is denser it has greater attraction relative to lower density objects. It is known that the Earth's crust consists of many rock types with varying densities. This variation in density causes distortions in the gravity field over the surface of the Earth. Hence, changes in the subsurface involving differing densities would reflect a change in the intensity of gravity (Nettleton, 1976).

Field observations of gravity anomalies caused by density differences in the subsurface lithology are most often small. They are often masked by instrumental and topographical factors. These factors can be split into two main categories (Seigel, 1995; Boyd, 2003; Otoum, 2011): 1) Temporal factors and 2) spatial factors.

Temporal factors, such as instrumental drift and tidal effects, like the name implies, are variations that are time dependent. These factors change even if the location of the gravimeter does not (Boyd, 2003).

Instrumental drift will happen to all gravimeters. Even in a controlled environment with constant temperature, the spring in the machine will experience elastic relaxation and change gravity readings (Nettleton, 1976). Along with this, other human-related issues may arise such as impact shock, transportation vibration, improper temperature conditions, and long periods of power loss all of which can cause up to 0.1 mGal of drift per day (Boyd, 2003). Tidal effects are the gravitational attraction from the positioning of the Sun and Moon (Nettleton, 1976). These effects can be very serious and may cause as much as 0.3 mGal variation in the measured gravity (Seigel, 1995).

To correct for these temporal factors, a standard field procedure of establishing a base station is employed. Periodically reoccupying the base station allows for the tide and instrumental drift effects to be a time varying influence (Seigel, 1995; Boyd, 2003). In essence each measurement is relative to the base station. Each time the base station is measured an offset correction is established for the stations that follow. Standard software that automatically accounts for tidal effects is also included in most modern gravimeters.

Spatial factors are factors that depend on the space or location of the instrument (Seigel, 1995; Boyd, 2003; Otoum, 2011). These factors all require a set of corrections which include latitude, free-air, Bouguer, and terrain corrections (Figure 2.15)

The need for latitude correction stems from two factors, the elliptical shape and rotation of the Earth (Hammer, 1943; Nettleton, 1976; Boyd, 2003). At the Equator an increase of 3.39 gals is experienced due to the outward centrifugal acceleration of the Earth. Flattening experienced at the poles causes an increase of 6.63 gals because the

surface is closer to the Earth's center of mass (Hammer, 1943). A mathematical formula is used to correct for latitude (Moritz, 1992):

$$Gn = 9.780327(1.0 + 0.0053024\ sin^2(\theta) - 0.0000058\ sin^2(2\theta)) \quad \ldots\ldots(1)$$

Gn is gravity normal in mGal after latitude correction. θ is the latitude in decimal degrees of the gravity measurement.

Free-air and Bouguer corrections can both be attributed to the effects of elevation (Nettleton, 1976; Seigel, 1995). Free-air effects are due to the fact that the higher the elevation, the further away it is from the Earth's central mass. The further away something is from the center of the Earth, the lower the gravitation acceleration (Nettleton, 1976). However, when a surface measurement is taken at a high elevation it is not taken in midair. It is usually on a feature such as a mountain or other large mass. This additional mass exerts a gravitational pull (Seigel, 1995). This is the Bouguer effect. To correct for these, I used the two following equations:

$$Gf = Go - Gn + \Delta Gf \quad \ldots\ldots(2)$$

$$\Delta Gf = \pm 0.3086h \text{ mGal/m} \quad \ldots\ldots(3)$$

Gf is the free-air corrected gravity readings in mGal; *Go* is the raw observed measurements in mGal; Δ*Gf* is the free-air correction in mGal; *h* is the elevation in meters. All free-air corrections above sea level will be positive and all corrections below sea level will be negative.

$$Gb = 0.04192\rho h \ldots\ldots(4)$$

Gb is the Bouguer correction in mGal; ρ is the bulk density of the overburden in grams per cubic centimeter; *h* is the elevation in meters. The end product is a corrected set of data points commonly referred to as Bouguer anomalies (Otoum, 2011).

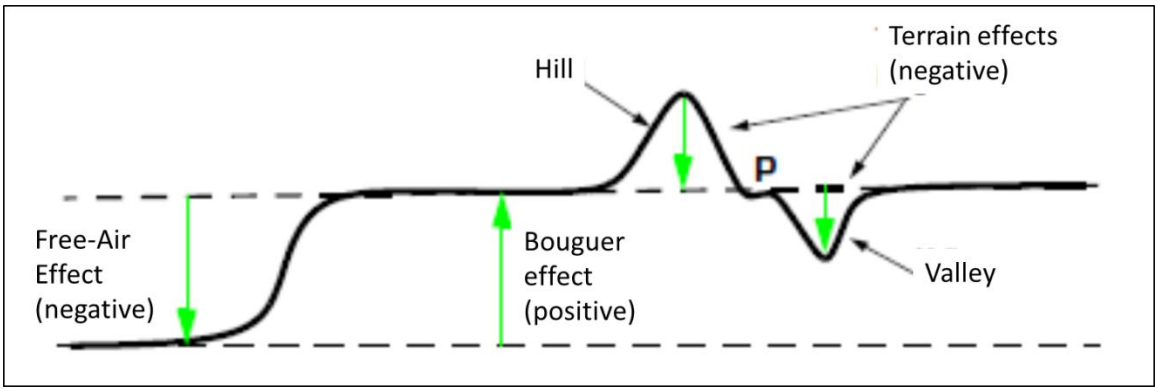

Figure 2.15: Illustration of the different spatial factors that may affect the observed gravity (Seigel, 1995).

A terrain correction is applied to account for irregularities in the topography near the gravity measurement location. Topographic features such as mountains and valleys cause reductions in gravity readings (Seigel, 1995).

2.4.2 Survey Design

The objective of the survey is to identify any subsurface movement of the salt dome over time. Two lines, one oriented north-south and one oriented east-west, were designed over the crest of the Pierce Junction salt dome. Each lines location was assessed for environmental variables (seismic noise, wind vibration, and elevation differences), location reoccupation, and safety. The target depth is about 250 m. This is known from previous publications from Teas (1935) amd Holzer & Bluntzer (1984). The station spacing was set to 100 m to provide adequate resolution to identify the salt dome.

2.4.3 Equipment

The equipment used in the survey included:

- Base GPS antenna type: Zephyr Geodetic with ground plane (GP)
- Rover GPS antenna type: Trimble 5800

- Survey Controller: Trimble TSC 2
- Radio: Trimble HPB450
- GPS Receiver: Trimble 5700
- Tripods and Bi-pods: one fixed height tripod, one bi-pod, and one fixed height staff
- Gravimeter: Scintrex CG-5 Autograv (Figure 2.16)
- Miscellaneous: hammer, survey nails/spikes, spray paint, measuring wheel, and personal safety equipment as required by Texas Brine

2.4.4 Field Procedures

The N-S gravity line started at the northeastern limit of the Texas Brine property line at Pierce Junction. A measuring wheel was used to measure 100 m intervals for each station along a 1 km line. At each station a survey spike (MAG SPIKE) was driven into the ground to mark its location. Spray paint was also used to mark the location. A base station was set on the third station of the N-S line. This is where the center of the dome was hypothesized to be. For the E-W line the eastern limit of the property was used (close to the front gate). Intervals of 100 m were also used on this line for a total of 900 m. The 1 km marker was not reached because it encountered the property limit of the facility. After the stations were emplaced, the locations were measured using Real Time Kinematic (RTK) GPS. RTK GPS is fast and accurate for short baselines. A baseline is the distance from the base GPS station to the rover. The rover is the mobile unit used for GPS measurements. High horizontal and vertical accuracy is achieved in post process of the RTK survey.

Gravity measurements were taken after the GPS survey was complete. Two gravity surveys were conducted for each line at two different times of the year. One set was taken on 5 May, 2011 and the second set was taken on 28 September, 2011. Before setting up the gravimeter, the tripod was placed firmly on the ground. The tripod stabilizes and levels the gravimeter.

2.4.5 Processing

2.4.5.1 RTK GPS

The first step in post processing is getting the data out of the equipment and into the computer. To do this, the tool Trimble Data Transfer Utility was used. This tool extracts and decompresses Trimble zipped files (.T00 or .T01) into .DAT files. For the base station the .DAT file will be larger in size relative to the other GPS measurements. This is because an accurate location for the base station is required. The occupation time for the base station was between six to eight hours. OPUS was used to process the base station. Once the base station coordinates were received via email the next step of processing the RTK data began.

The RTK survey was processed using Trimble Geomatics Office (TGO) following UNAVCO's procedures (UNAVCO, 2010). Trimble Geomatics Office is proprietary Trimble software that helps you to easily perform survey tasks, quickly check field work, and depending on the modules installed, process GPS baselines (Trimble Navigation Limited, 2002). In TGO a project must be setup for each survey with the Universal Transverse Mercator (UTM) zone 15N projection and the WGS 1984 datum. Next, the survey controller's .DC file is loaded. This gives a visual of the survey

locations as points. To adjust the points to the base stations coordinates TGO's Recompute tool was used.

2.4.5.2 Gravity

A Microsoft Excel spreadsheet was used to correct for Latitude, Free-Air, and Bouguer (Table 2.1). The spreadsheet method was modeled after Fourie (1998) and Ottoum (2011). Terrain correction was not done because of the relatively flat topography of the Houston area. Drift and tide corrections were done on the fly in the gravimeter during acquisition. Figures 2.17 to 2.20 show the differences between raw gravity measurements and corrected gravity measurements.

Figure 2.16: Field measurement of a section of N-S gravity line. In the lower right corner of the image is the Scintrex CG-5 Autograv. In my hand is the remote control to start gravity measurements.

Table 2.1: Microsoft Excel table showing the progression of raw gravity measurements into Bouguer anomalies. With the first three columns (Raw Gravity, GPS Elevation, and Latitude) the Latitude correction can be calculated. From there, the Free-Air and Bouguer corrections are calculated.

	Raw Gravity	GPS Elevation	Latitude	Lat. Corr.	Free-Air Corrected	Bouguer Corrected
base station	2732.595	18.187	29.65779885	9.8304	2728.377	2727.004
1	2732.745	17.439	29.6586988	9.8304	2728.296	2726.980
2	2732.806	17.196	29.65957159	9.8304	2728.282	2726.984
3	2732.866	16.965	29.66043616	9.8304	2728.271	2726.991
5	2732.511	18.098	29.65690675	9.8304	2728.266	2726.900
6	2732.420	18.435	29.65600461	9.8303	2728.279	2726.888
7	2732.430	18.541	29.65510445	9.8303	2728.321	2726.922
8	2732.322	18.977	29.6541995	9.8303	2728.347	2726.916
9	2732.242	19.2	29.65328717	9.8303	2728.336	2726.888
10	2732.078	19.557	29.65237971	9.8303	2728.283	2726.807
11	2732.297	18.438	29.65147632	9.8303	2728.157	2726.765
12	2732.243	18.64	29.65056901	9.8302	2728.165	2726.759
13	2732.172	18.62	29.64967039	9.8302	2728.088	2726.683
14	2732.113	18.688	29.64904559	9.8302	2728.050	2726.640
base station	2732.508	18.187	29.65779885	9.8304	2728.290	2726.918
16	2732.536	17.9	29.65758892	9.8304	2728.230	2726.879
17	2732.392	18.338	29.6576039	9.8304	2728.220	2726.837
18	2732.481	17.93	29.65761288	9.8304	2728.184	2726.831
19	2732.548	17.763	29.65761318	9.8304	2728.199	2726.859
20	2732.486	17.903	29.65760132	9.8304	2728.180	2726.829
21	2732.370	18.213	29.65760191	9.8304	2728.160	2726.785
22	2732.365	17.971	29.65760455	9.8304	2728.080	2726.724
23	2732.419	17.56	29.65764824	9.8304	2728.007	2726.682
24	2732.442	17.46	29.65761348	9.8304	2727.999	2726.682
25	2732.441	17.344	29.65758313	9.8304	2727.963	2726.654

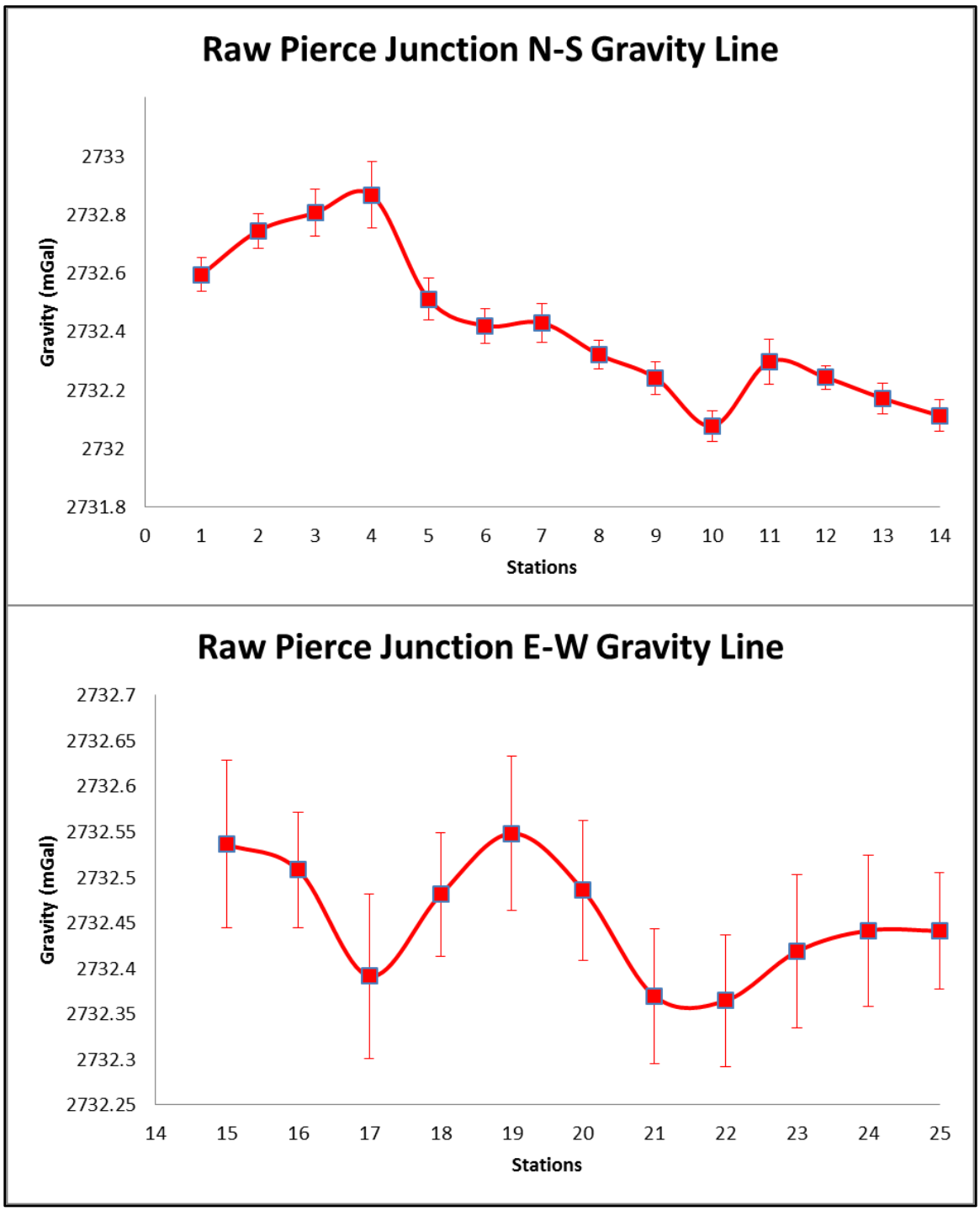

Figure 2.17: Graph of raw gravity data measurements collected in May 2011.

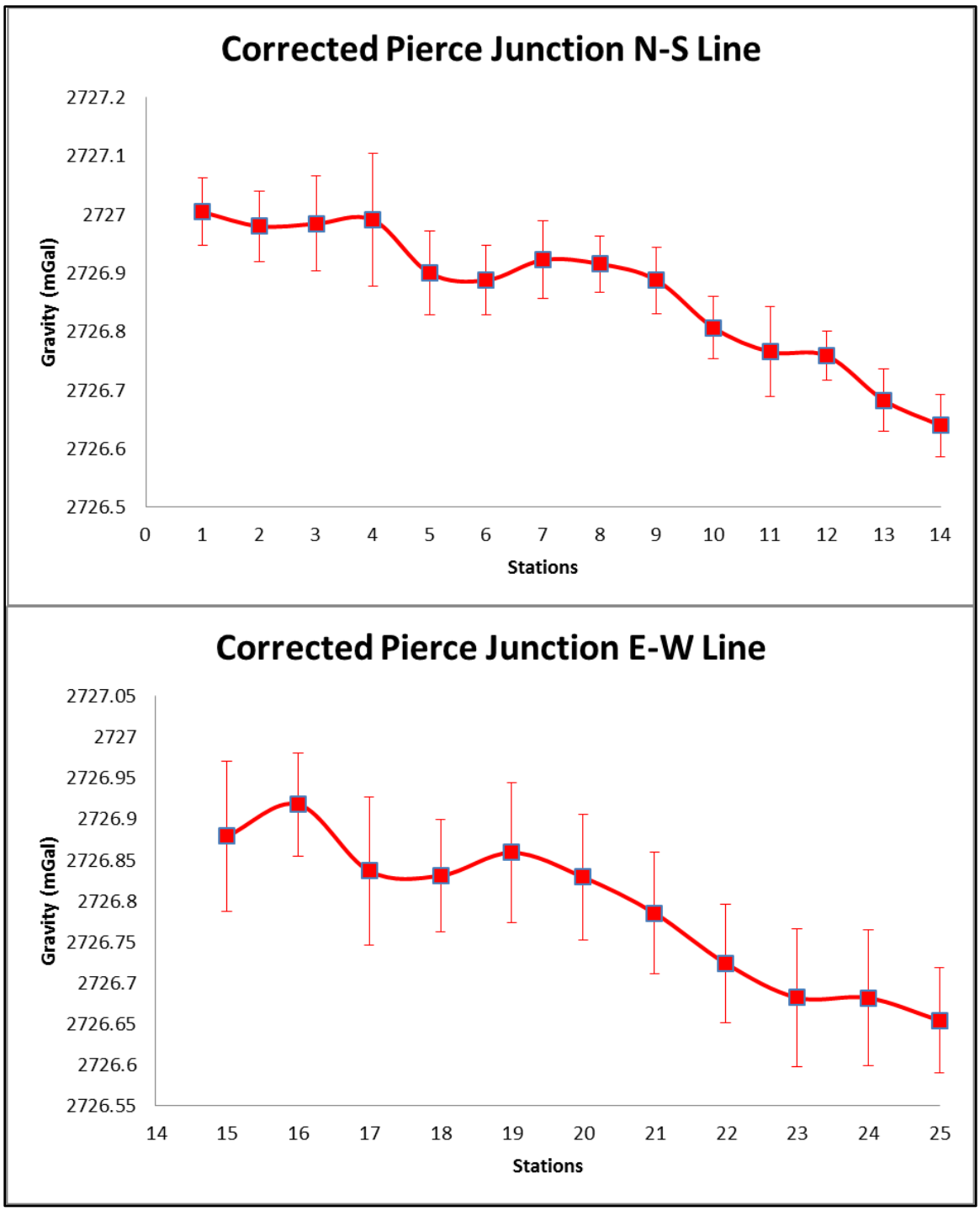

Figure 2.18: Graph of corrected gravity data measurements collected in May 2011.

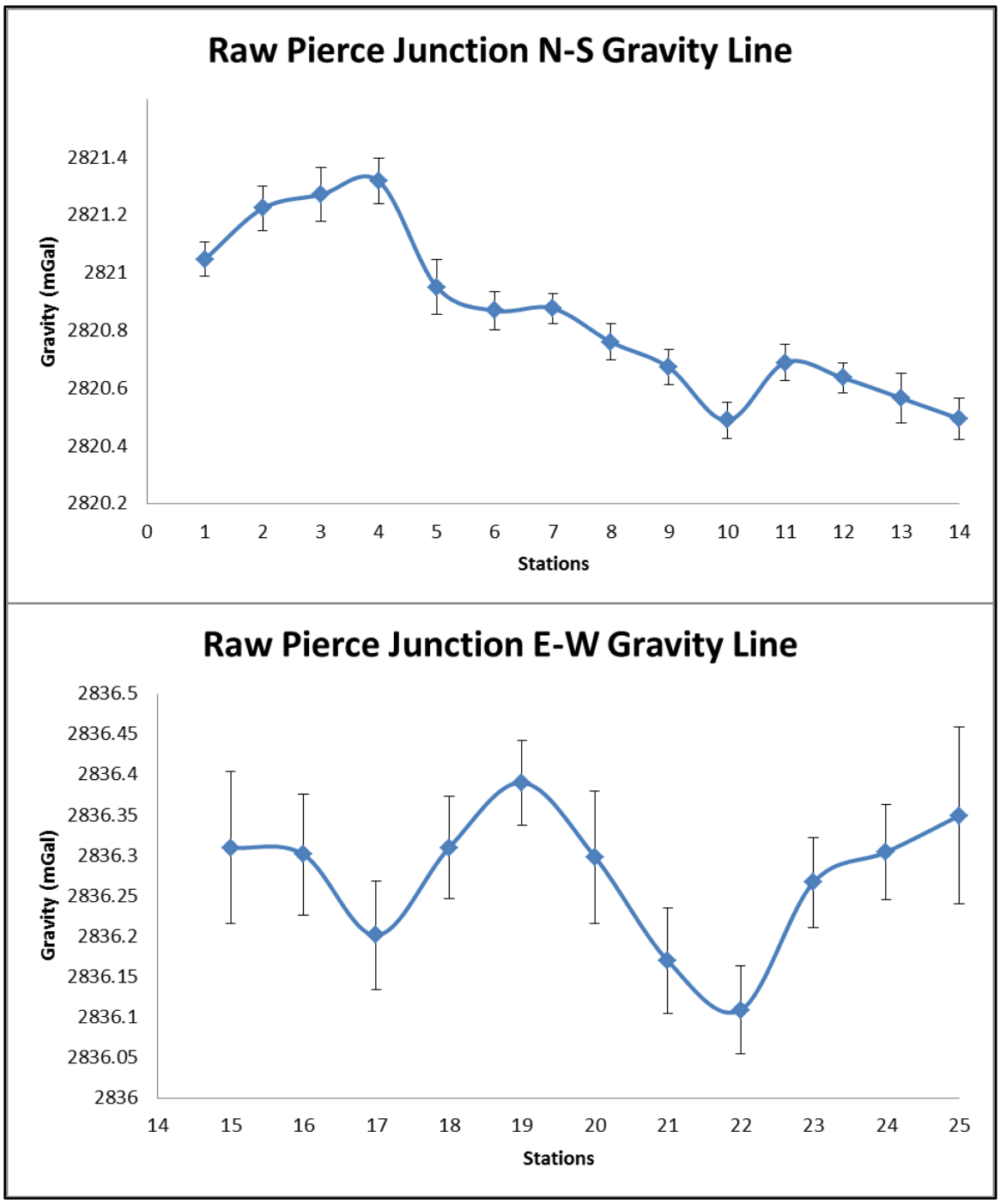

Figure 2.19: Graph of raw gravity data measurements collected in September, 2011.

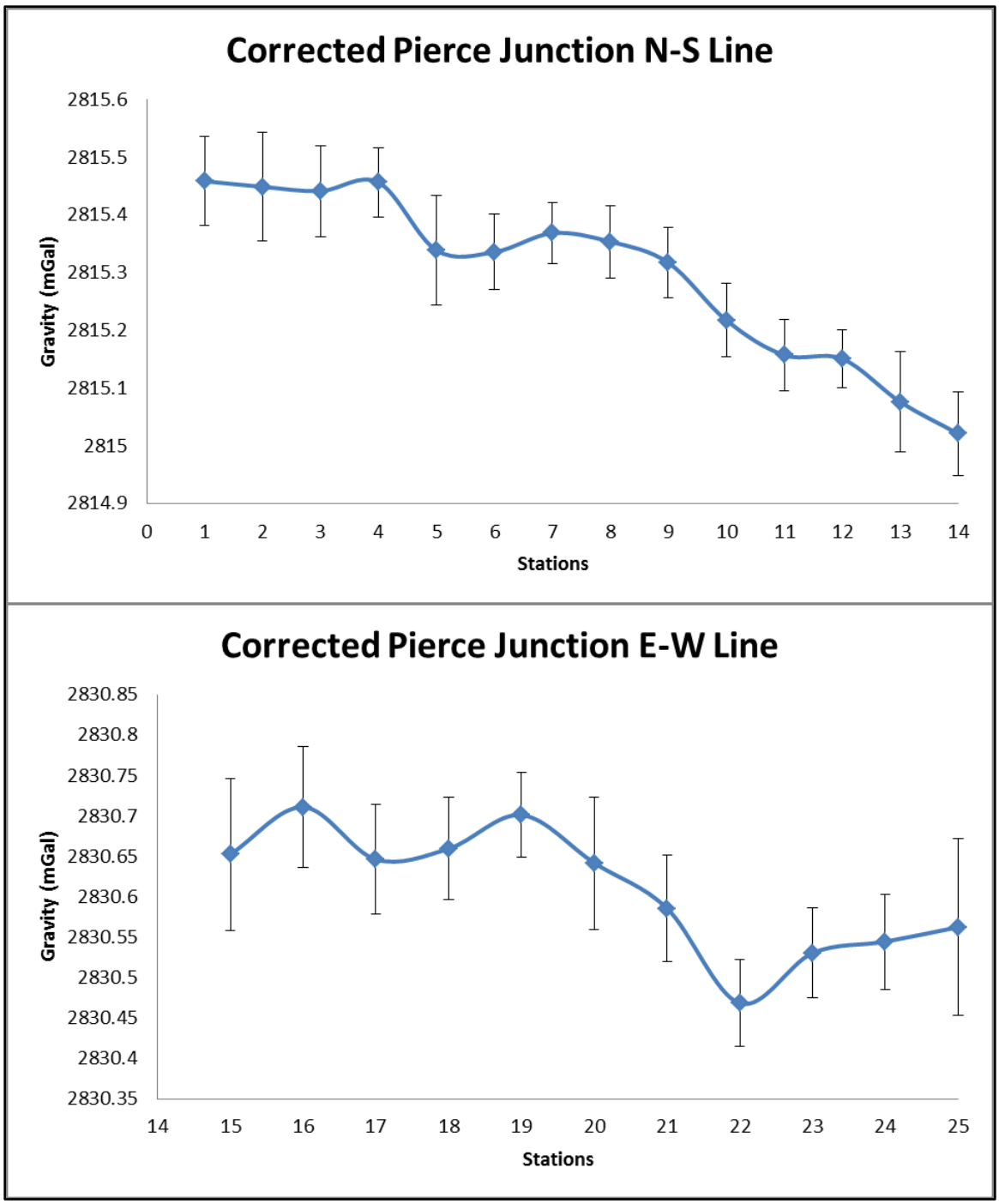

Figure 2.20: Graph of corrected gravity data measurements collected in September, 2011.

Chapter 3 **Results**

Results of the GPS, LiDAR, TLS, and gravity data are presented below. These different complementary techniques were used to interpret patterns in the surface deformation for the greater Houston area.

3.1 GPS

Data from sixty nine GPS sites (53 PAM and 16 CORS) in the greater Houston area were analyzed to yield vertical displacement rates with respect to LKHU, ADKS, and NETP (Table 3.1). Vertical movements can be attributed to known features such as groundwater withdrawal, fault creep, and salt domes (Engelkemeir et al., 2010). Figure 3.1 and 3.2 show surfaces generated from subsidence rates from two different time intervals (1994-2010 and 2007-2011). Figure 3.1 (1994-2010) shows subsidence in the northwest region and uplift in the southeast region. The highest rates of subsidence are localized in the Jersey Village area. Figure 3.2 (2007-2011) shows a similar pattern of subsidence in this area. The lowest rates of subsidence and uplift are mostly in the South Houston area. The areas of both subsidence and uplift in Figure 3.1 are smaller compared to Figure 3.2. The two figures also show location of salt domes. Note that PAM stations 15, 25, 34, and 39 were either destroyed or were missing data; therefore, data from these sites are not included in this analysis. According to the HGSD website (http://www.hgsubsidence.org), PAM stations 34 and 39 are operational but data are unavailable.

Table 3.1: PAM and CORS station with current and past rates.

Sites	TYPE	Current (mm/yr)	Dates	Past (mm/yr)	Dates
PAM 00	PAM	-1.46	2007-2011	-2.65	1996-2010
PAM 01	PAM	-18.62	2007-2011	-40.87	1994-2010
PAM 02	PAM	-22.63	2007-2011	-32.96	1994-2010
PAM 03	PAM	-12.05	2007-2011	-35.40	1994-2010
PAM 04	PAM	-16.06	2007-2011	-18.72	1995-2010
PAM 05	PAM	-9.49	2007-2011	-23.72	1996-2010
PAM 06	PAM	-17.89	2007-2011	-29.30	1997-2010
PAM 07	PAM	-23.36	2007-2011	-40.26	1999-2010
PAM 08	PAM	-18.62	2007-2011	-28.58	1999-2010
PAM 09	PAM	-7.67	2007-2011	-3.02	1999-2010
PAM 10	PAM	-1.10	2007-2011	-5.45	1999-2010
PAM 11	PAM	-9.86	2007-2011	-6.19	2000-2010
PAM 12	PAM	-32.12	2007-2010	-13.25	2001-2010
PAM 13	PAM	-20.44	2007-2011	-19.22	2001-2010
PAM 14	PAM	-9.13	2007-2011	-9.14	2001-2010
PAM 15	PAM	Destroyed	NA	NA	NA
PAM 16	PAM	-13.14	2007-2011	-11.55	2001-2010
PAM 17	PAM	-17.52	2007-2011	-21.05	2001-2010
PAM 18	PAM	-18.62	2007-2011	-25.30	2001-2010
PAM 19	PAM	-9.86	2007-2011	-13.05	2001-2010
PAM 20	PAM	-5.11	2007-2011	-0.86	2002-2010
PAM 21	PAM	-8.03	2007-2011	-6.45	2002-2010
PAM 22	PAM	0.37	2007-2011	-5.96	2002-2010
PAM 23	PAM	2.56	2007-2011	-1.35	2002-2010
PAM 24	PAM	1.83	2007-2011	0.74	2002-2010
PAM 25	PAM	Destroyed	NA	NA	NA
PAM 26	PAM	0.73	2007-2011	-2.55	2002-2010
PAM 27	PAM	-1.46	2007-2011	-5.85	2002-2010
PAM 28	PAM	-2.19	2007-2011	-0.67	2002-2010
PAM 29	PAM	-21.54	2007-2011	-21.20	2007-2010
PAM 30	PAM	-8.40	2007-2011	-14.91	2007-2010
PAM 31	PAM	-1.83	2007-2011	-9.48	2007-2010
PAM 32	PAM	-4.38	2007-2011	-8.54	2007-2010
PAM 33	PAM	-6.57	2007-2011	-3.46	2007-2010
PAM 34	PAM	NA	NA	NA	NA
PAM 35	PAM	-0.29	2007-2011	-1.56	2007-2010
PAM 36	PAM	-1.46	2007-2011	-5.04	2007-2010
PAM 37	PAM	2.19	2007-2011	0.33	2007-2010
PAM 38	PAM	1.83	2007-2011	-5.89	2007-2010
PAM 39	PAM	NA	NA	NA	NA
PAM 40	PAM	-18.25	2007-2011	-18.35	2007-2010
PAM 41	PAM	-5.48	2007-2011	-13.40	2007-2010
PAM 42	PAM	-5.11	2007-2011	-12.11	2007-2010
PAM 43	PAM	0.18	2007-2011	-2.69	2007-2010
PAM 44	PAM	-14.97	2007-2011	-20.95	2007-2010
PAM 45	PAM	-4.75	2007-2011	-1.86	2007-2010
PAM 46	PAM	-22.63	2007-2011	-31.91	2007-2010
PAM 47	PAM	-26.28	2007-2011	-30.74	2007-2010
PAM 48	PAM	-13.14	2007-2011	-21.43	2007-2010
PAM 49	PAM	2.56	2007-2011	-6.21	2007-2010
PAM 50	PAM	1.46	2007-2011	-1.50	2007-2010
PAM 51	PAM	-5.48	2007-2011	-4.30	2007-2010
PAM 52	PAM	-2.19	2007-2011	-2.60	2007-2010
PAM 53	PAM	-0.73	2007-2011	-4.07	2007-2010
PAM 54	PAM	-1.46	2007-2011	-2.72	2007-2010
PAM 55	PAM	1.83	2007-2011	-0.65	2007-2010
PAM 56	PAM	-4.38	2007-2011	-12.81	2007-2010
COH1	CORS	-8.03	2007-2011	-11.33	2003-2010
COH2	CORS	-6.94	2007-2011	-6.58	2003-2010
COH3	CORS	4.02	2007-2011	1.09	2003-2008
COH4	CORS	0.73	2007-2011	0.73	2003-2010
COH5	CORS	NA	NA	NA	NA
COH6	CORS	-8.03	2007-2011	-8.42	2003-2010
COH7	CORS	2.19	2007-2011	-11.19	2003-2008
ROD1	CORS	-18.98	2007-2011	-25.83	2007-2010
TMCC	CORS	-1.10	2007-2011	-4.04	2003-2010
TXAG	CORS	0.37	2007-2011	-3.05	2005-2010
TXBY	CORS	-0.07	2007-2011	-3.53	2005-2010
TXCN	CORS	-11.68	2007-2011	-13.15	2005-2010
TXGA	CORS	-5.48	2007-2011	-5.35	2005-2010
TXGV	CORS	-0.18	2007-2011	-3.95	2007-2010
TXHE	CORS	-9.86	2007-2011	-8.05	2005-2010
TXLI	CORS	-0.11	2007-2011	-2.43	2005-2010
TXLM	CORS	-4.02	2007-2011	-7.19	2005-2010
TXRO	CORS	-18.98	2007-2011	-8.24	2005-2010

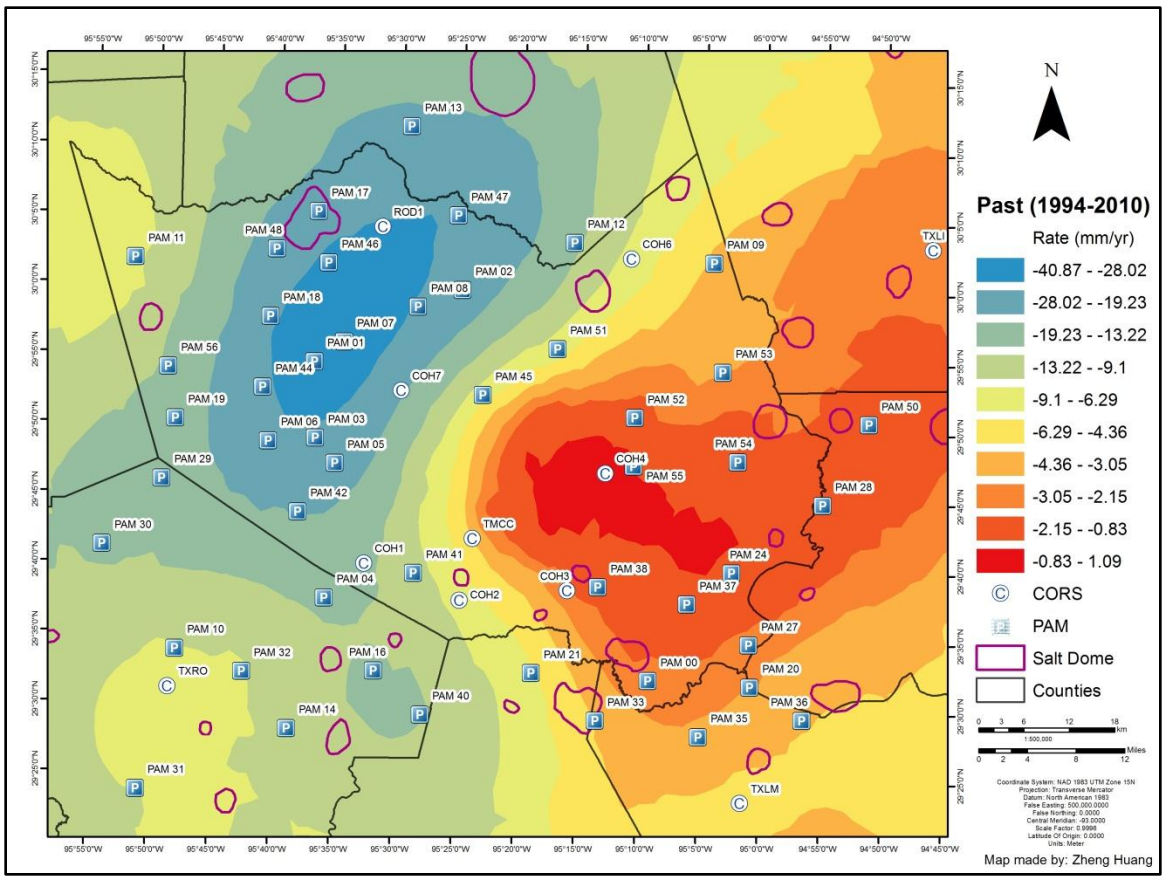

Figure 3.1: Kriging surface displaying GPS (PAM and CORS) derived surface deformation in the greater Houston area for the years 1994 through 2010. The area is extensively covered by both CORS and PAM GPS stations. As seen in this surface there is an area of subsidence in the northwest and an area of uplift in the southeast. One key difference is the distribution of salt domes in the two areas. In the southeast there are more known salt domes relative to the northwest. This may suggest some association between uplift and salt diapirism.

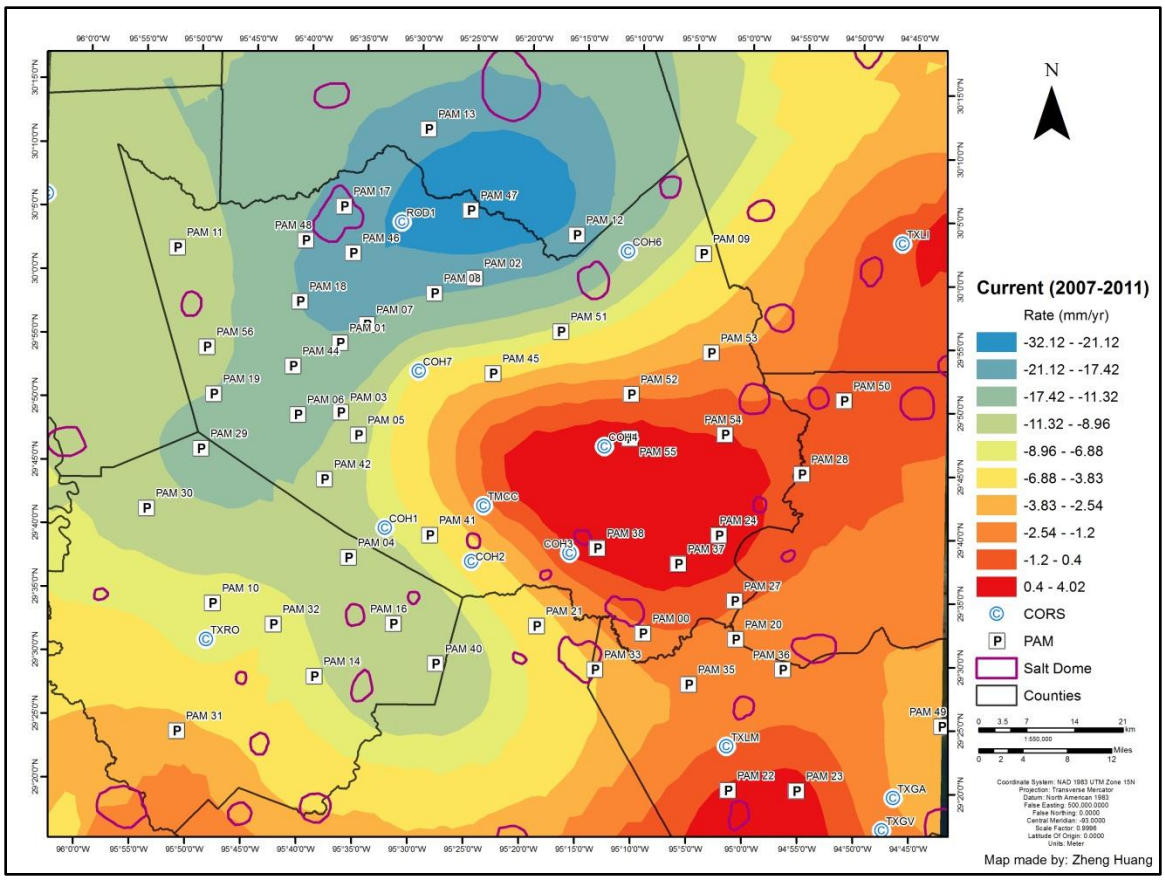

Figure 3.2: Kriging surface displaying GPS (PAM and CORS) derived surface deformation in the greater Houston area for the years 2007 through 2011. Similar to figure 3.1 subsidence is seen in the northwest and uplift in the southeast. Some notable differences are that the area of subsidence appears to be migrating to the north whereas the uplift is still relatively located in the same area. This could further support the role of salt in these surface deformations. The area of uplift is still concentrated around the southeastern salt domes whereas the northwestern subsidence is unconfined and moving north.

3.2 LiDAR

3.2.1 DEM Height Computed

DEM height computations using Engelkemeir's (2008) polygon method were used for Pierce Junction, Mykawa, South Houston, Webster, Lil Rich, Humble, Hockley, Tomball, and Goose Creek (Figure 3.3). Three different LiDAR DEMs were used with data from 1996, 2001 (Terrapoint), and 2008 (Merrick).

Figure 3.4 shows polygons colored according to the mean elevation for the 2008 (Figure 3.4), 2001 (Figure 3.5), and 1996 (Figure 3.6) for the Pierce Junction salt dome. A difference in mean elevation can be seen for areas within the outline of the salt dome and areas outside.

Table 3.2 displays the results of the zonal statistics with each salt dome's statistics highlighted in a different color. From Table 3.2, the mean elevation of the center was compared to the north, south, east, and west. The mean value with the highest difference to the center was picked to do comparisons (Table 3.3). The difference between the center and highest outer polygon were plotted to compare variability (Figure 3.7).

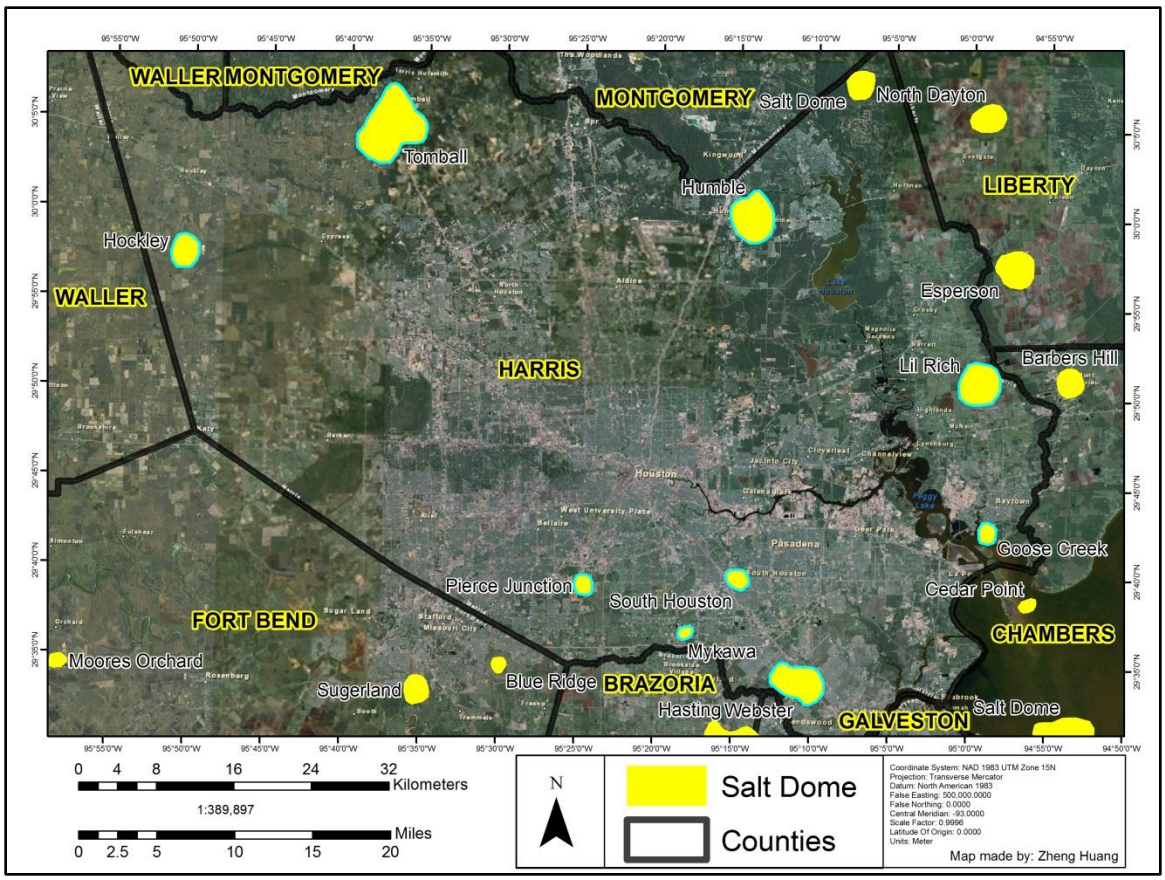

Figure 3.3: Harris County, Texas is outlined in black. Salt domes surrounding the county are in yellow and salt domes that were examined are outlined in light blue. These salt domes include Pierce Junction, Mykawa, South Houston, Goose Creek, Lil Rich, Humble, Tomball, and Hockley.

Table 3.2: Zonal statistic results from the polygon method.

	1996					2001					2008				
ZONE	MIN	MAX	RANGE	MEAN	STD	MIN	MAX	RANGE	MEAN	STD	MIN	MAX	RANGE	MEAN	STD
PJ Center	14.33	23.16	8.84	18.18	0.77	16.02	21.86	5.84	17.95	0.60	15.71	24.20	8.49	18.00	0.66
PJ East	9.75	17.07	7.32	13.55	0.64	11.82	15.30	3.48	13.46	0.55	11.61	16.70	5.09	13.42	0.53
PJ North	12.19	20.12	7.92	14.59	0.54	12.35	19.29	6.95	14.62	0.44	12.00	16.29	4.29	14.51	0.43
PJ South	11.28	19.20	7.92	14.77	0.60	11.86	17.90	6.04	14.72	0.56	11.37	20.32	8.95	14.91	0.59
PJ West	11.58	22.25	10.67	16.74	0.87	15.17	19.00	3.82	16.55	0.52	15.37	19.05	3.67	16.56	0.43
Mykawa Center	11.89	18.59	6.71	14.21	0.51	10.51	15.52	5.01	14.22	0.46	12.47	16.50	4.03	14.21	0.39
Mykawa East	10.67	17.68	7.01	14.09	0.38	11.04	15.23	4.18	14.20	0.38	10.67	15.70	5.04	14.01	0.38
Mykawa North	12.50	16.15	3.66	14.75	0.36	13.60	15.79	2.19	14.87	0.28	13.03	15.66	2.63	14.64	0.30
Mykawa South	12.50	14.94	2.44	13.48	0.33	12.91	14.57	1.66	13.67	0.30	12.71	14.50	1.79	13.58	0.27
Mykawa West	13.11	17.07	3.96	15.14	0.59	13.14	16.23	3.09	14.99	0.54	11.98	17.64	5.66	15.01	0.59
SH Center	7.32	14.63	7.32	8.98	0.52	7.55	10.29	2.74	9.02	0.31	4.69	11.07	6.38	9.04	0.32
SH East	7.32	17.37	10.06	9.15	0.66	7.66	9.97	2.31	9.11	0.26	7.42	10.14	2.73	9.12	0.27
SH North	4.57	11.28	6.71	9.29	0.65	7.01	10.58	3.57	9.44	0.59	6.42	11.09	4.67	9.37	0.60
SH South	9.45	14.02	4.57	11.74	0.54	10.40	14.20	3.80	12.01	0.44	10.08	13.64	3.56	11.97	0.46
SH West	7.92	13.41	5.49	10.97	0.73	9.44	12.83	3.39	11.12	0.66	6.44	12.79	6.35	10.95	0.65
Webster Center	7.62	12.19	4.57	10.15	0.52	8.10	11.52	3.42	10.03	0.49	7.90	11.55	3.65	9.98	0.50
Webster East	-0.91	10.67	11.58	8.28	0.76	2.67	10.72	8.05	8.20	0.59	2.11	10.50	8.39	8.09	0.62
Webster North	5.49	15.85	10.36	9.57	0.85	5.77	11.16	5.38	9.49	0.77	5.84	11.11	5.27	9.49	0.77
Webster South	5.49	11.89	6.40	7.86	0.79	6.18	9.47	3.29	7.82	0.67	5.83	9.71	3.87	7.80	0.65
Webster West	6.71	12.50	5.79	10.27	0.50	8.36	11.89	3.54	10.16	0.48	8.09	11.80	3.71	10.15	0.51
LR Center	8.53	15.85	7.32	11.47	0.57	7.92	13.21	5.29	11.31	0.54	6.02	13.10	7.09	11.27	0.54
LR East	7.32	10.97	3.66	9.22	0.33	7.35	10.43	3.08	9.27	0.30	7.18	10.65	3.47	9.19	0.30
LR North	9.75	13.41	3.66	11.82	0.49	10.29	13.12	2.83	11.72	0.46	10.20	13.28	3.07	11.70	0.51
LR South	8.84	13.11	4.27	10.86	0.57	9.16	12.32	3.15	10.71	0.60	9.01	12.46	3.45	10.79	0.69
LR West	11.58	15.24	3.66	13.48	0.35	11.90	14.52	2.62	13.55	0.31	11.64	14.77	3.13	13.40	0.35
Humble Center	17.37	28.96	11.58	23.28	1.82	17.78	28.39	10.61	23.40	1.87	17.54	28.07	10.53	23.21	1.85
Humble East	17.37	27.13	9.75	21.46	0.59	17.69	26.28	8.58	21.46	0.56	17.41	24.93	7.53	21.39	0.51
Humble North	19.20	28.65	9.45	24.12	1.13	19.72	27.67	7.95	24.21	1.12	19.50	27.83	8.33	24.09	1.12
Humble South	16.46	23.77	7.32	20.10	1.06	17.09	23.02	5.93	20.11	1.02	16.60	23.06	6.45	20.01	1.04
Humble West	22.56	29.57	7.01	25.84	0.93	24.01	27.98	3.96	26.00	0.86	22.42	28.16	5.74	25.70	0.96
Hockley Center	48.16	58.22	10.06	51.51	1.44	48.51	56.70	8.18	51.41	1.34	48.24	57.49	9.25	51.42	1.30
Hockley East	47.24	54.25	7.01	50.94	1.29	47.54	53.63	6.09	50.84	1.28	47.20	53.74	6.54	50.80	1.29
Hockley North	55.78	64.31	8.53	60.51	1.77	56.08	63.84	7.76	60.47	1.60	55.52	64.10	8.59	60.49	1.57
Hockley South	47.85	52.43	4.57	50.63	0.42	49.39	51.80	2.40	50.60	0.44	46.73	52.71	5.97	50.48	0.43
Hockley West	51.51	60.35	8.84	54.31	1.39	52.20	60.30	8.11	54.53	1.32	52.47	60.28	7.81	54.40	1.36
Tomball Center	40.84	60.66	19.81	51.66	2.36	44.49	57.37	12.89	51.43	2.23	45.53	57.21	11.68	51.35	2.21
Tomball East	41.15	47.55	6.40	43.46	0.55	41.73	45.79	4.06	43.51	0.51	41.06	48.89	7.82	43.49	0.54
Tomball North	48.46	64.62	16.15	55.67	3.50	48.17	63.71	15.54	55.50	3.66	47.51	63.67	16.16	55.45	3.69
Tomball South	40.23	48.46	8.23	43.73	0.98	39.61	47.42	7.81	43.73	1.01	39.18	46.34	7.16	43.58	0.99
Tomball West	58.83	69.49	10.67	64.36	1.55	58.73	68.31	9.58	64.34	1.51	58.76	69.01	10.25	64.30	1.51
GC Center	0.30	7.32	7.01	3.87	0.74	0.51	5.87	5.37	3.91	0.75	0.04	5.87	5.83	3.76	0.72
GC East	-0.30	8.23	8.53	5.05	0.82	0.42	7.26	6.84	5.20	0.79	-0.12	6.67	6.79	5.12	0.77
GC North	5.18	10.36	5.18	7.73	0.88	5.23	9.68	4.45	7.77	0.90	5.14	9.85	4.71	7.72	0.89
GC South	3.96	11.89	7.92	6.00	0.84	3.76	8.85	5.08	6.02	0.74	3.29	8.45	5.15	5.94	0.74
GC West	2.74	6.71	3.96	3.63	0.42	2.96	5.89	2.93	3.67	0.44	4.79	8.95	4.16	5.49	0.22

Table 3.3: Center and largest difference polygon.

	1996						2001						2008				
ZONE	MIN	MAX	RANGE	MEAN	STD		MIN	MAX	RANGE	MEAN	STD		MIN	MAX	RANGE	MEAN	STD
PJ Center	14.33	23.16	8.84	18.18	0.77		16.02	21.86	5.84	17.95	0.60		15.71	24.20	8.49	18.00	0.66
PJ East	9.75	17.07	7.32	13.55	0.64		11.82	15.30	3.48	13.46	0.55		11.61	16.70	5.09	13.42	0.53
Mykawa Center	11.89	18.59	6.71	14.21	0.51		10.51	15.52	5.01	14.22	0.46		12.47	16.50	4.03	14.21	0.39
Mykawa South	12.50	14.94	2.44	13.48	0.33		12.91	14.57	1.66	13.67	0.30		12.71	14.50	1.79	13.58	0.27
SH Center	7.32	14.63	7.32	8.98	0.52		7.55	10.29	2.74	9.02	0.31		4.69	11.07	6.38	9.04	0.32
SH South	9.45	14.02	4.57	11.74	0.54		10.40	14.20	3.80	12.01	0.44		10.08	13.64	3.56	11.97	0.46
Webster Center	7.62	12.19	4.57	10.15	0.52		8.10	11.52	3.42	10.03	0.49		7.90	11.55	3.65	9.98	0.50
Webster South	5.49	11.89	6.40	7.86	0.79		6.18	9.47	3.29	7.82	0.67		5.83	9.71	3.87	7.80	0.65
LR Center	8.53	15.85	7.32	11.47	0.57		7.92	13.21	5.29	11.31	0.54		6.02	13.10	7.09	11.27	0.54
LR East	7.32	10.97	3.66	9.22	0.33		7.35	10.43	3.08	9.27	0.30		7.18	10.65	3.47	9.19	0.30
Humble Center	17.37	28.96	11.58	23.28	1.82		17.78	28.39	10.61	23.40	1.87		17.54	28.07	10.53	23.21	1.85
Humble South	16.46	23.77	7.32	20.10	1.06		17.09	23.02	5.93	20.11	1.02		16.60	23.06	6.45	20.01	1.04
Hockley Center	48.16	58.22	10.06	51.51	1.44		48.51	56.70	8.18	51.41	1.34		48.24	57.49	9.25	51.42	1.30
Hockley North	55.78	64.31	8.53	60.51	1.77		56.08	63.84	7.76	60.47	1.60		55.52	64.10	8.59	60.49	1.57
Tomball Center	40.84	60.66	19.81	51.66	2.36		44.49	57.37	12.89	51.43	2.23		45.53	57.21	11.68	51.35	2.21
Tomball West	58.83	69.49	10.67	64.36	1.55		58.73	68.31	9.58	64.34	1.51		58.76	69.01	10.25	64.30	1.51
GC Center	0.30	7.32	7.01	3.87	0.74		0.51	5.87	5.37	3.91	0.75		0.04	5.87	5.83	3.76	0.72
GC North	5.18	10.36	5.18	7.73	0.88		5.23	9.68	4.45	7.77	0.90		5.14	9.85	4.71	7.72	0.89

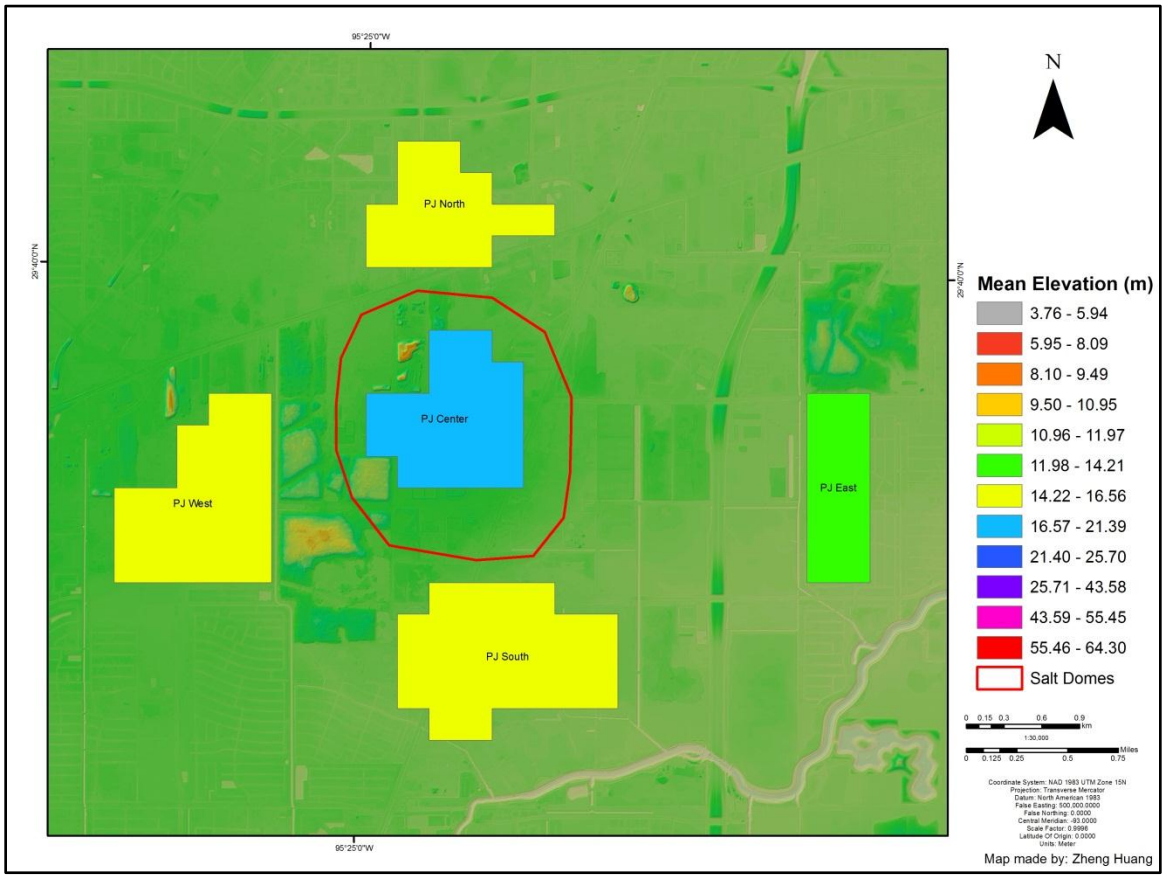

Figure 3.4: Polygon based DEM height computations for Pierce Junction salt dome. Color scale is set to mean elevation (m) for 2008 which was extracted from the Zonal Statistics as Table tool from ArcGIS 10. The background is a hillshade image of the 2008 DEM. Notice the polygons were created to avoid the anomalies in the DEM.

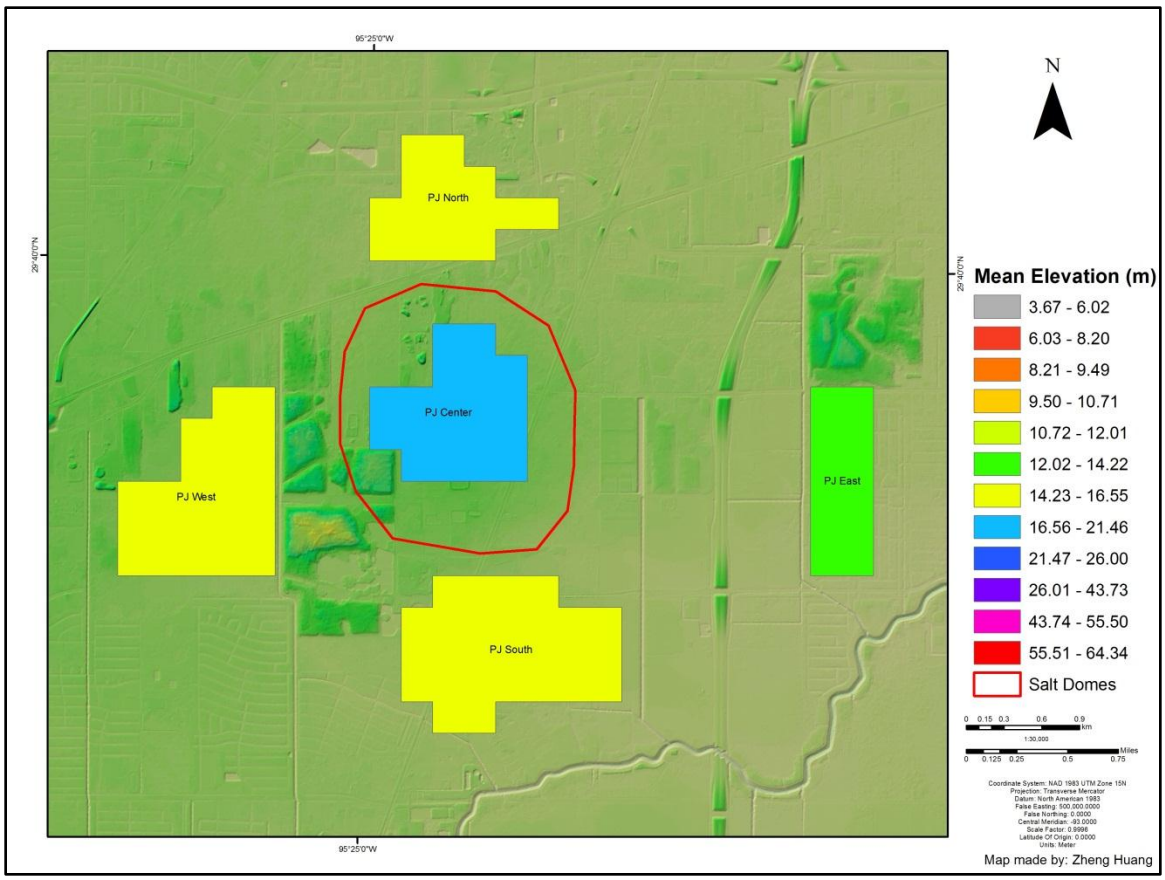

Figure 3.5: Polygon based DEM height computations for Pierce Junction salt dome. Color scale is set to mean elevation (m) for 2001 which was extracted from the Zonal Statistics as Table tool from ArcGIS 10. The background is a hillshade image of the 2001 DEM. Notice the polygons were created to avoid the anomalies in the DEM which are present in the 2001 DEM also.

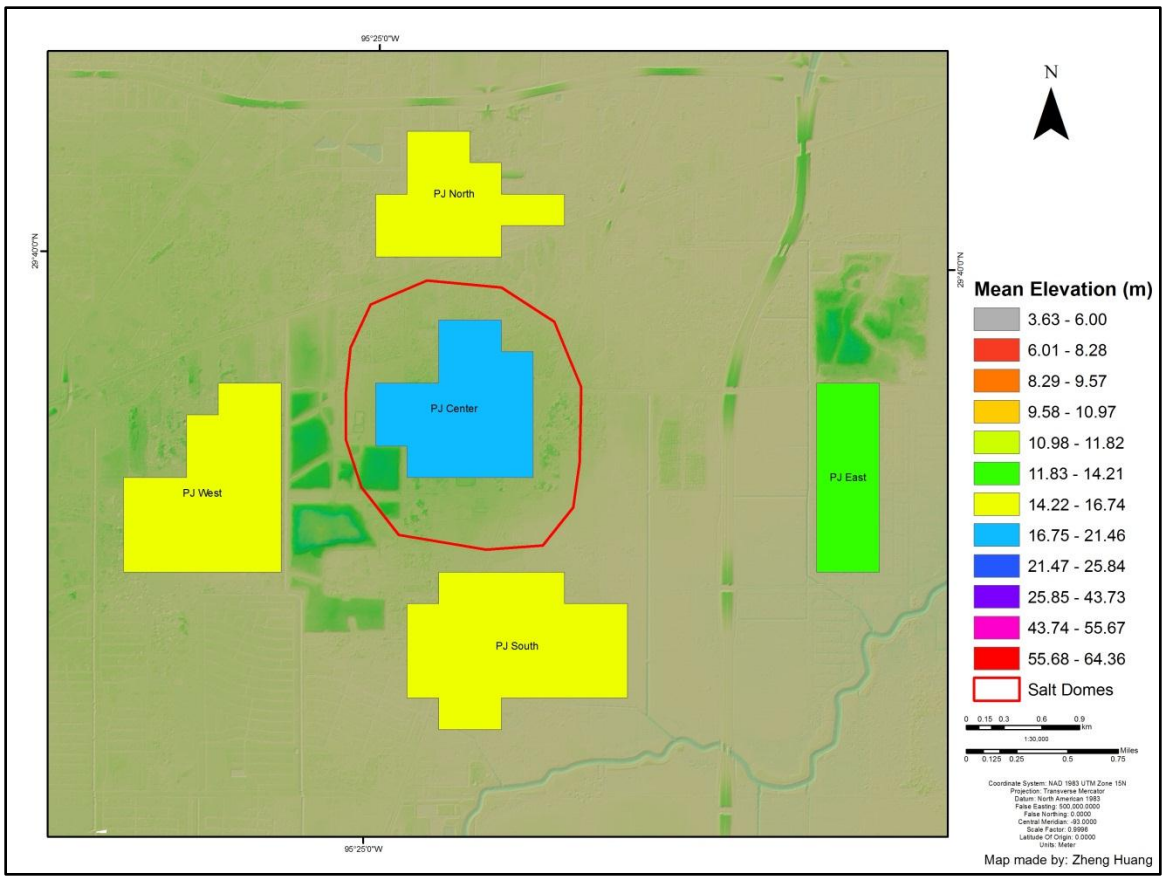

Figure 3.6: Polygon based DEM height computations for Pierce Junction salt dome. Color scale is set to mean elevation (m) for 1996 which was extracted from the Zonal Statistics as Table tool from ArcGIS 10. The background is a hillshade image of the 1996 DEM. Notice the polygons were created to avoid the anomalies in the DEM which are present in the 2001 DEM also.

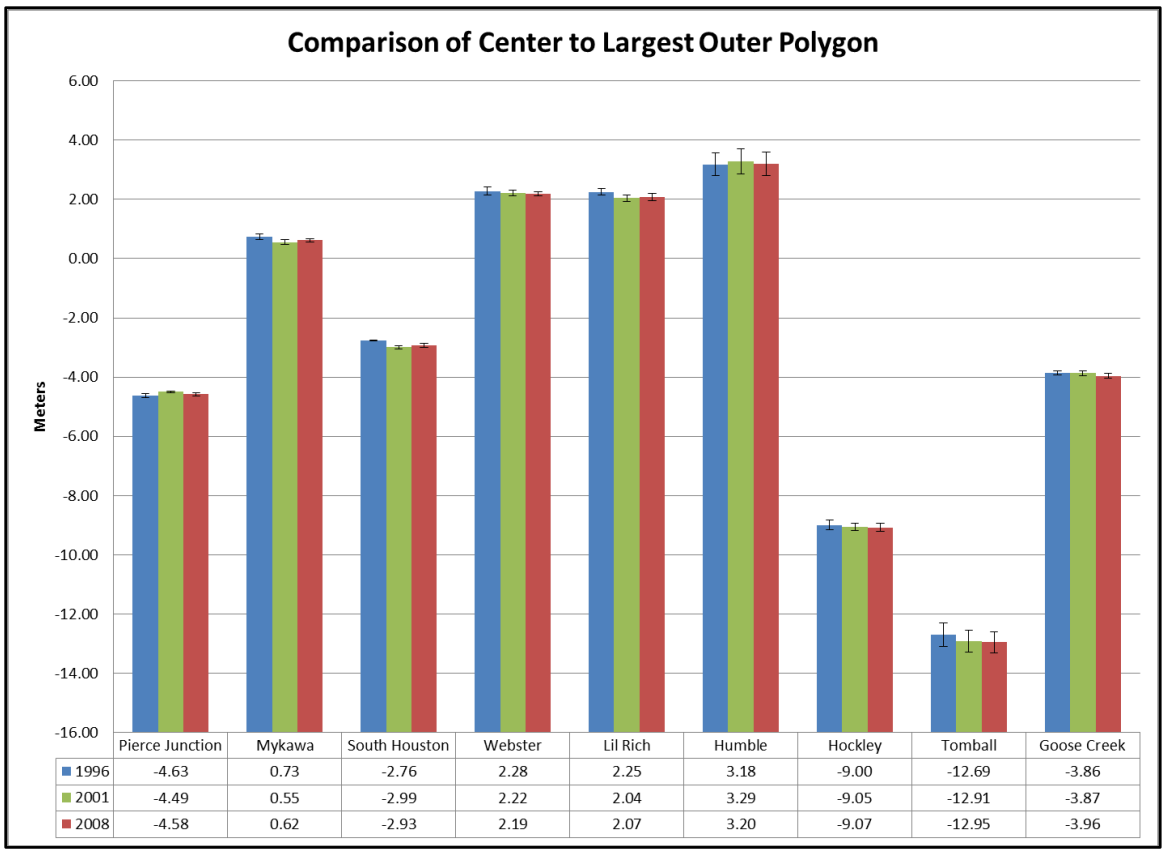

	Pierce Junction	Mykawa	South Houston	Webster	Lil Rich	Humble	Hockley	Tomball	Goose Creek
1996	-4.63	0.73	-2.76	2.28	2.25	3.18	-9.00	-12.69	-3.86
2001	-4.49	0.55	-2.99	2.22	2.04	3.29	-9.05	-12.91	-3.87
2008	-4.58	0.62	-2.93	2.19	2.07	3.20	-9.07	-12.95	-3.96

Figure 3.7: Comparison of the mean elevation of the central polygon versus one of the outer polygons.

3.2.2 Terrestrial Laser Scanner (TLS)

Elevation changes were calculated for two TLS scans over a portion of the Pierce Junction salt dome (Figure 3.8). One was completed on 17 March, 2011 the other was completed on 14 October, 2011. The LiDAR point clouds were cleaned-up and geo-referenced (as described in Chapter 2). The LiDAR point cloud was gridded and examined using ArcGIS 10. The average elevation was extracted for each scan set. The first scan had an average elevation of 17.89 m and the second had an average elevation of 17.95 m (Table 3.4). A difference of 6 cm is seen in the average elevation. GPS ground truth was conducted over the scan area as well (Table 3.5).

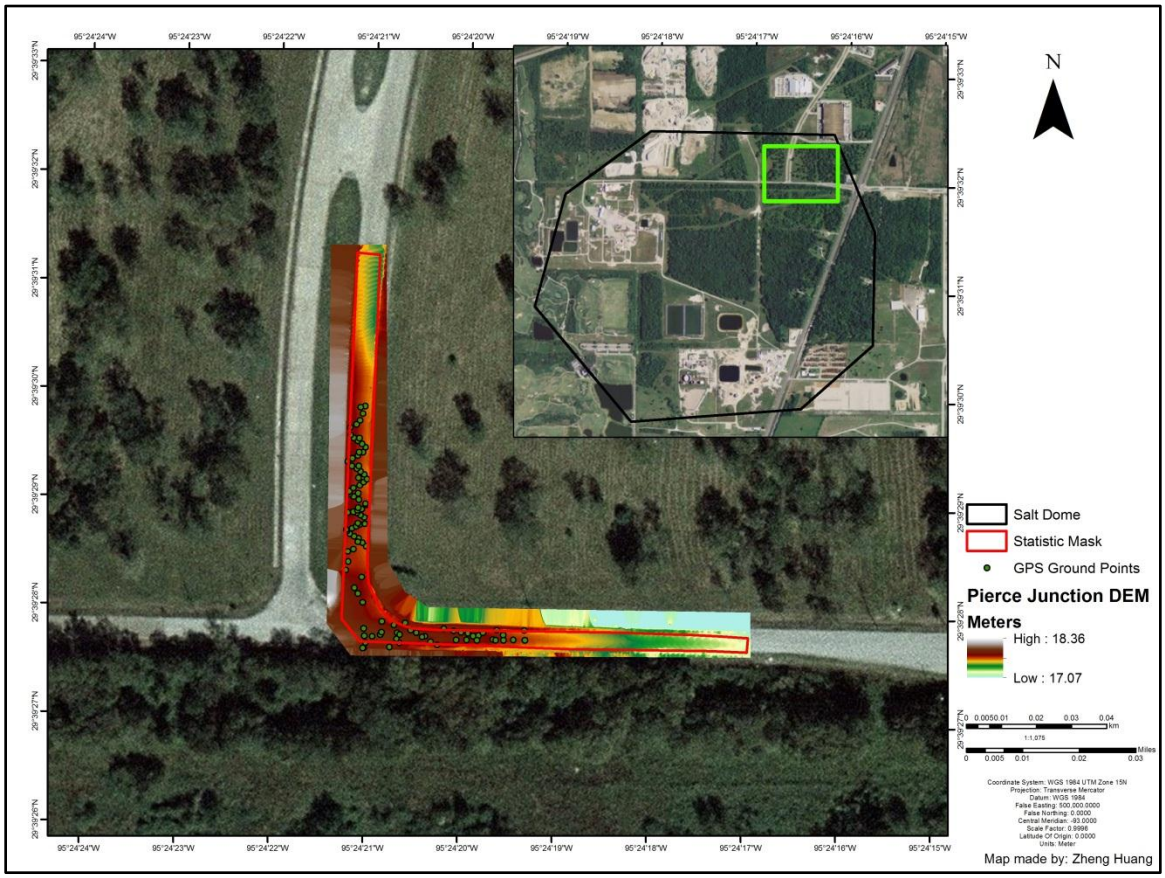

Figure 3.8: DEM from TLS over northeastern part of Pierce Junction salt dome. This location was the intersection of two streets: Fannin and Reed Road.

Table 3.4: Statistics of DEM from TLS data.

Scans	Min	Max	Mean	Std Dev
TLS of Pierce Juncition March	17.07	18.36	17.89	0.23
TLS of Pierce Juncition October	17.47	19.94	17.95	0.15

Table 3.5: GPS ground truth over scanned area. The max height difference was 5 cm, minimum – 5 cm, median 0, and standard deviation 2 cm.

Point	Northing (m)	Easting (m)	GPS Height (m)	LiDAR Height (m)	Height Difference (m)
1	3283296.31	267137.51	17.92	17.90	**-0.02**
2	3283298.84	267138.08	17.90	17.90	**0.00**
3	3283301.60	267138.03	17.90	17.89	**-0.01**
4	3283302.26	267139.60	17.90	17.90	**0.00**
5	3283303.23	267143.18	17.92	17.90	**-0.02**
6	3283304.12	267142.16	17.93	17.90	**-0.03**
7	3283305.39	267141.00	17.93	17.92	**-0.01**
8	3283305.95	267139.75	17.92	17.92	**0.00**
9	3283306.75	267138.54	17.92	17.91	**-0.01**
10	3283307.49	267137.81	17.92	17.91	**-0.01**
11	3283307.82	267137.61	17.92	17.92	**0.00**
12	3283308.23	267139.23	17.92	17.92	**0.00**
13	3283308.83	267140.39	17.94	17.92	**-0.02**
14	3283309.24	267141.41	17.92	17.92	**0.00**
15	3283309.48	267142.84	17.92	17.91	**-0.01**
16	3283311.00	267143.38	17.91	17.91	**0.00**
17	3283311.80	267141.80	17.93	17.93	**0.00**
18	3283311.32	267142.70	17.92	17.91	**0.00**
19	3283311.92	267141.59	17.94	17.93	**-0.01**
20	3283312.69	267140.55	17.94	17.94	**0.00**
21	3283312.71	267138.05	17.94	17.94	**0.00**
22	3283312.88	267139.57	17.95	17.94	**-0.01**
23	3283313.26	267140.80	17.92	17.94	**0.02**
24	3283313.66	267141.96	17.93	17.93	**0.00**
25	3283314.95	267143.32	17.90	17.92	**0.02**
26	3283315.24	267143.02	17.90	17.92	**0.02**
27	3283316.37	267141.11	17.93	17.93	**0.00**
28	3283317.22	267139.68	17.93	17.93	**0.00**
29	3283318.02	267138.61	17.93	17.93	**0.00**
30	3283318.60	267138.35	17.92	17.93	**0.01**

Table 3.5 continued

31	3283318.73	267138.52	17.92	17.93	**0.01**
32	3283319.67	267139.55	17.94	17.91	**-0.03**
33	3283320.52	267141.35	17.90	17.89	**-0.01**
34	3283321.28	267142.45	17.92	17.88	**-0.04**
35	3283322.25	267143.48	17.89	17.88	**-0.01**
36	3283323.50	267142.68	17.90	17.89	**-0.01**
37	3283324.41	267141.61	17.91	17.89	**-0.02**
38	3283325.14	267140.58	17.91	17.90	**0.00**
39	3283325.94	267139.22	17.93	17.93	**0.00**
40	3283327.26	267138.06	17.93	17.94	**0.01**
41	3283328.13	267139.26	17.92	17.93	**0.01**
42	3283328.84	267140.88	17.91	17.92	**0.01**
43	3283329.85	267142.33	17.87	17.90	**0.03**
44	3283331.23	267143.10	17.86	17.88	**0.02**
45	3283332.24	267141.99	17.88	17.90	**0.02**
46	3283333.03	267140.89	17.90	17.93	**0.03**
47	3283333.97	267139.69	17.92	17.94	**0.02**
48	3283334.69	267138.83	17.93	17.95	**0.02**
49	3283336.90	267138.79	17.93	17.96	**0.03**
50	3283337.75	267140.49	17.89	17.94	**0.04**
51	3283340.74	267142.34	17.87	17.89	**0.02**
52	3283342.94	267143.04	17.83	17.88	**0.05**
53	3283342.62	267141.64	17.88	17.90	**0.02**
54	3283338.89	267141.49	17.90	17.92	**0.02**
55	3283333.84	267141.32	17.90	17.92	**0.02**
56	3283329.83	267141.19	17.91	17.92	**0.01**
57	3283325.99	267141.14	17.90	17.90	**0.00**
58	3283322.59	267141.07	17.90	17.90	**0.00**
59	3283318.23	267140.98	17.93	17.91	**-0.02**
60	3283314.09	267140.91	17.94	17.94	**0.00**
61	3283309.61	267140.86	17.93	17.92	**-0.01**
62	3283304.35	267140.85	17.91	17.90	**-0.01**
63	3283294.34	267141.91	17.95	17.93	**-0.02**
64	3283291.37	267139.80	17.96	17.94	**-0.02**
65	3283289.67	267140.80	17.96	17.95	**-0.01**
66	3283287.13	267142.22	17.95	17.94	**-0.01**
67	3283281.82	267147.70	17.95	17.93	**-0.02**
68	3283280.73	267151.14	17.97	17.96	**-0.01**

Table 3.5 continued

69	3283278.47	267152.06	18.04	18.02	**-0.02**
70	3283275.71	267152.70	18.02	18.01	**-0.01**
71	3283279.77	267142.49	18.01	18.00	**-0.01**
72	3283277.72	267142.65	18.05	18.03	**-0.02**
73	3283274.32	267142.50	17.93	17.92	**-0.01**
74	3283274.20	267142.18	17.97	17.92	**-0.05**
75	3283275.77	267142.99	18.01	17.98	**-0.03**
76	3283277.48	267144.93	18.05	18.03	**-0.02**
77	3283278.10	267147.19	18.07	18.03	**-0.04**
78	3283274.54	267149.89	17.99	17.98	**-0.01**
79	3283276.75	267151.85	18.07	18.04	**-0.03**
80	3283281.35	267154.32	17.96	17.95	**-0.01**
81	3283279.27	267155.83	18.00	17.99	**-0.01**
82	3283278.55	267157.46	18.02	18.01	**-0.01**
83	3283277.53	267159.83	18.06	18.05	**-0.01**
84	3283275.95	267161.53	18.03	18.02	**-0.01**
85	3283275.06	267163.39	17.98	17.97	**-0.01**
86	3283279.68	267165.37	17.98	18.00	**0.02**
87	3283279.04	267168.09	18.02	18.03	**0.01**
88	3283278.56	267170.22	18.02	18.05	**0.03**
89	3283278.38	267172.16	18.04	18.06	**0.02**
90	3283277.56	267173.58	18.07	18.08	**0.01**
91	3283277.80	267175.19	18.05	18.07	**0.02**
92	3283278.54	267176.47	18.04	18.06	**0.02**
93	3283276.56	267179.30	18.05	18.08	**0.03**
94	3283279.24	267180.39	18.00	18.03	**0.03**
95	3283277.90	267182.15	18.01	18.06	**0.05**
96	3283276.43	267188.34	18.05	18.07	**0.02**
97	3283279.16	267188.23	17.99	18.03	**0.04**
98	3283276.46	267185.06	18.03	18.07	**0.04**
99	3283276.43	267182.30	18.03	18.07	**0.04**
100	3283276.42	267180.05	18.05	18.08	**0.03**
101	3283276.37	267174.68	18.08	18.08	**0.00**
102	3283276.52	267171.84	18.03	18.08	**0.05**
103	3283276.49	267168.80	18.04	18.06	**0.02**
104	3283277.30	267159.15	18.05	18.04	**-0.01**
105	3283278.07	267152.81	18.04	18.03	**-0.01**
106	3283278.68	267147.60	18.04	18.02	**-0.02**

3.3 Gravity

Gravity data for the Pierce Junction N-S line were collected over the hypothesized center of the salt dome. Higher gravity readings were observed at the estimated center dome location. Gravity readings decreased as the station progressed south. There was a gravity difference of 0.36 mGal from the start of the survey to the end of the survey for 5 May, 2011. A gravity difference of 0.44 mGal from start to finish was observed for the 28 September, 2011 gravity survey.

The E-W profile displayed more variability between the two scanning periods of May and September. A difference of 0.27 mGal was seen from the May survey and a difference of 0.19 mGal for the September survey (Figure 3.9).

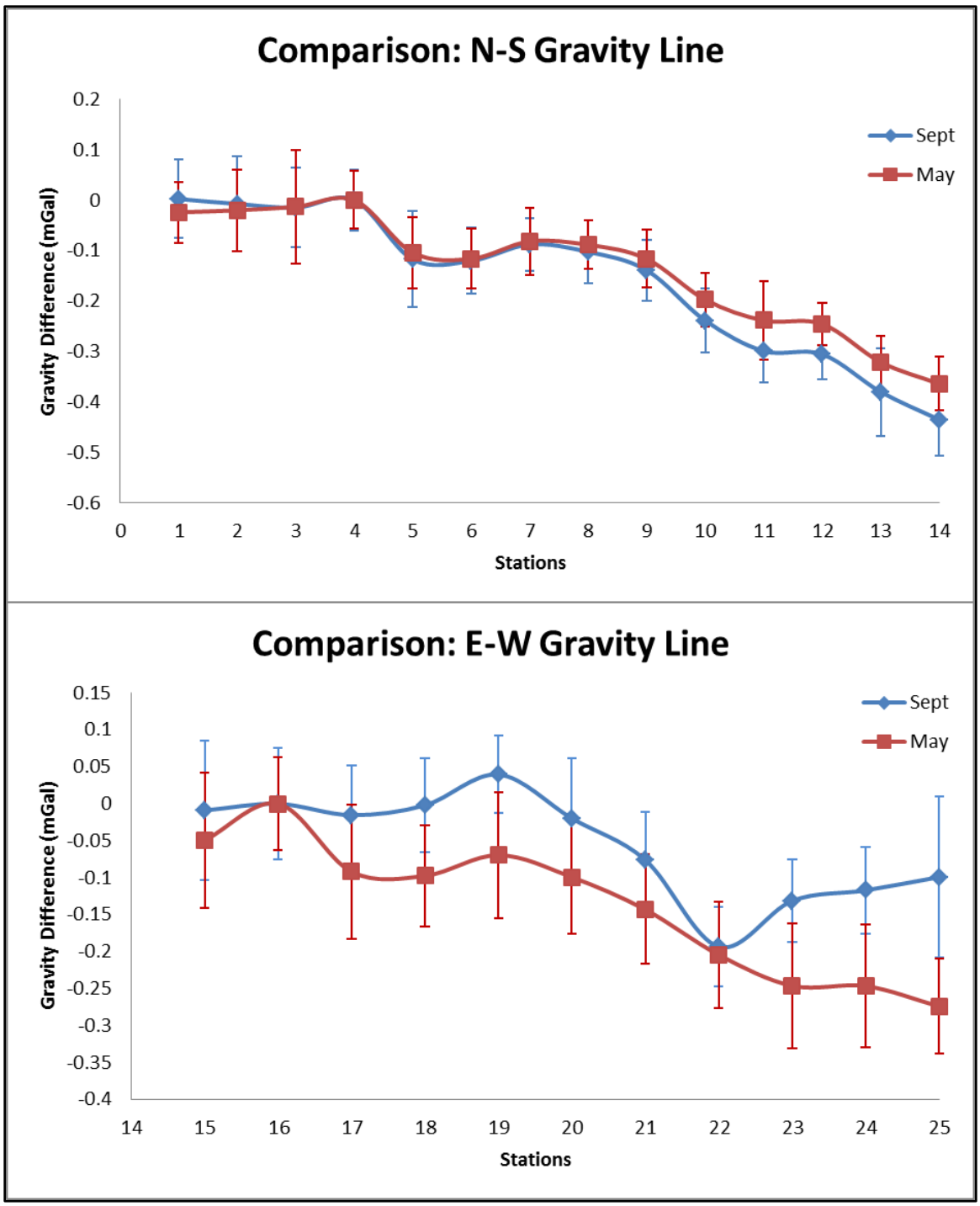

Figure 3.9: Gravity differences between the May and September gravity measurements. In the N-S line the September reading seem to be lower. In the E-W line the September reading seem to be higher. Stations 4 and 16 are base stations.

Chapter 4 **Discussion**

4.1 Surface Deformation Activity

GPS rates from the HGSD as well as ones calculated in this study show a change in surface deformation patterns. High rates of subsidence in the northwestern areas and signs of uplift in the southeast are observed. High rates of subsidence appear to decrease as time progresses. LiDAR-generated DEM analysis showed a change in the overall average elevations of the salt domes relative to their surroundings. The TLS analysis of a section of the Pierce Junction salt dome showed a change in the average elevation for a particular section of the study area. Gravity results of the two surveys over Pierce Junction both showed a range of change of 0.08 mGal within four months.

4.2 GPS Patterns

Patterns observed in the surfaces generated from the GPS rates clearly show continued subsidence in the Jersey Village area. Contrary to previous studies (Engelkemeir & Khan, 2008) in which the location of subsidence appeared to be expanding towards the northwest, my results show the area of subsidence is shrinking and migrating towards the northeast. One possibility could be the continued withdrawal of the subsurface salt. This idea was first proposed by Engelkemeir et al. (2010). If salt domes in the region are still experiencing active diapirism this could cause subsidence in areas such as northwest Harris County to experience subsidence. As seen in Figures 3.1 and 3.2, high rates of subsidence are mostly observed in areas with few to no salt domes. Figure 4.1 shows three GPS sites in the northwest all of which experienced subsidence. Figure 4.2 shows three GPS sites in the southeast, near salt domes, which experienced uplift.

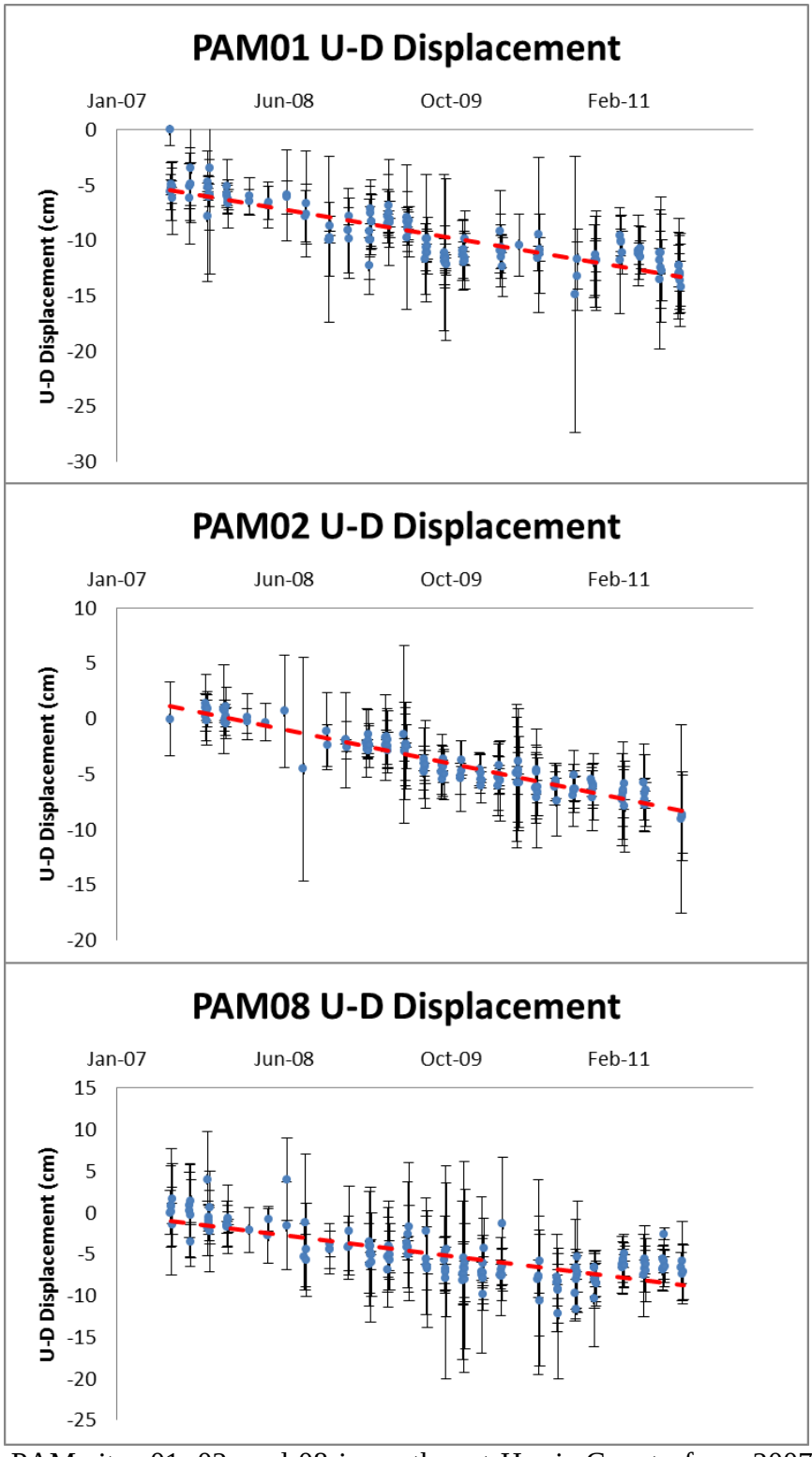

Figure 4.1: PAM sites 01, 02, and 08 in northwest Harris County from 2007-2011. The red dashed lines are the linear trend lines. All three are showing a negative trend which represents subsidence at these PAM sites.

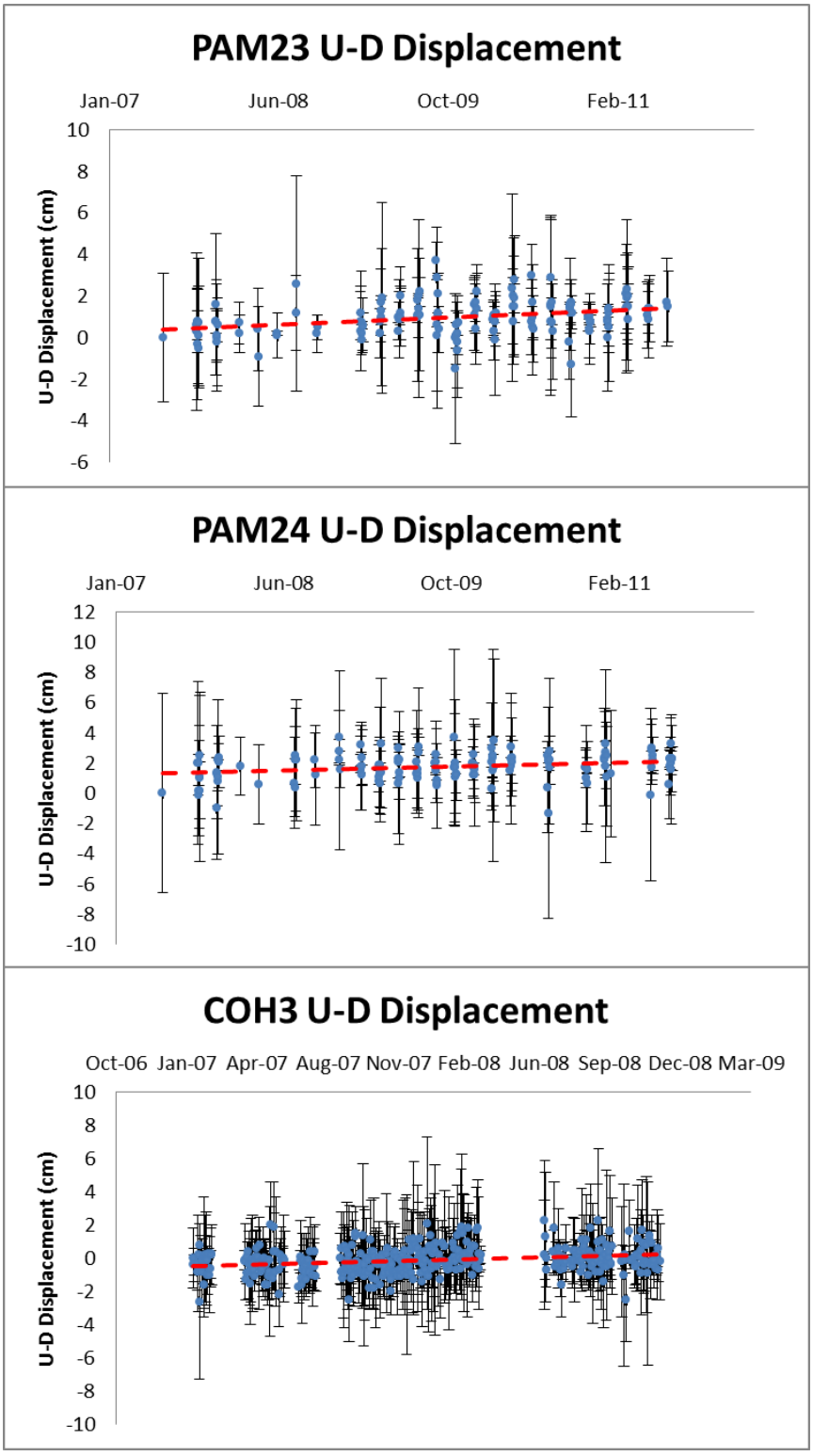

Figure 4.2: PAM sites 23, 24, and CORS COH3 in southeast Harris County from 2007-2011. The red dashed lines are the linear trend lines. All three are showing a slight positive trend which may represent uplift at these sites.

Jackson and Seni (1983) showed Texas salt domes had maximum gross growth rates of 400 to 450 m/Ma, which is roughly a growth rate of 0.45 mm/yr. The growth rates were not continuous and were thought to be more cyclic. Jackson and Talbot (1986) compiled data from 436 salt domes in the United States Gulf Coast and produced a model for average salt dome growth and their cycles (Figure 4.3). Pittman (1994) noted maximum growth of the salt domes in the greater Houston area followed closely to Jackson and Talbot's (1986) growth rates (Figure 4.4). The formation of a rim syncline may form as a result of salt withdrawal (Sorensen, 1986; Pittman, 1994; Hudec, et al., 2009; Brandes, et al., 2012). The presence of a rim syncline can be inferred from Figure 3.1. This rim syncline in the northwest area of Harris County appears to be the primary rim syncline which forms during the Pillow Stage (Figure 4.5). As a salt dome enters the Diapir Stage a secondary rim syncline is usually formed creating localized subsidence around the piercing salt dome (Brewer & Kenyon, 1996).

Another cause for these observed rates could be subsurface fluid withdrawal. These fluids include oil, gas, and groundwater. One well known incident of subsidence associated with oil and gas withdrawal occurred in the Goose Creek Oil Field. After one year of production subsidence was noted with subsidence rates exceeding 11 cm/yr (Pratt and Johnson, 1926). As mentioned in the Introduction, groundwater withdrawal can cause noticeable subsidence as was seen in the San Jacinto Battleground State Historical Park and Brownwood subdivision (Coplin & Galloway, 1999). Studies conducted by the U.S. Department of Commerce and the NGS suggest groundwater withdrawal as the major contribution to subsidence in the Houston area (Harris-Galveston Coastal Subsidence District & Espey, Huston & Associates Inc., 1981).

In 1999 the HGSD split Harris County into three regulatory areas (Harris-Galveston Subsidence District, 1999). Area one is in the southeast and extends into most of Galveston County. Area two is in south-central Harris County and a small part of Galveston County. Area two is also where the majority of Houston lies. Area three is in the north and northwest of Harris County (Figure 4.6). In 2010 the total groundwater withdrawal for areas one and two was 45.3 million gallons per day (MGD). The total groundwater withdrawal for area three was 195.5 MGD (Lacy, 2011). Groundwater withdrawal rates have dropped significantly since the 1970s within areas one and two (Figure 4.7). This may suggest that the subsidence seen in northwestern Harris County in Figures 3.1 and 3.2 are related to regulatory area three's higher groundwater withdrawal rates.

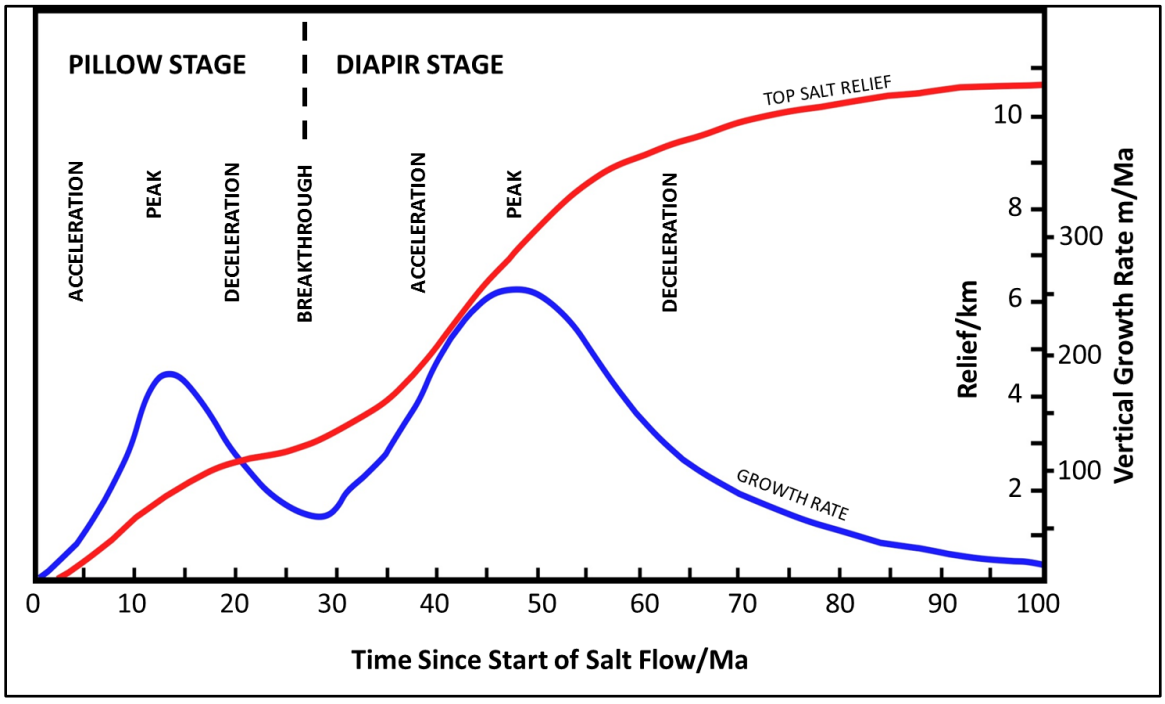

Figure 4.3: The growth rate of salt domes in the Gulf Coast Region. The two stages of salt evolution, Pillow and Diapir, are differentiated by the dashed line in the upper portion of the image. This shows two cycles of accelerated dome growth (Modified from Jackson & Talbot, 1986).

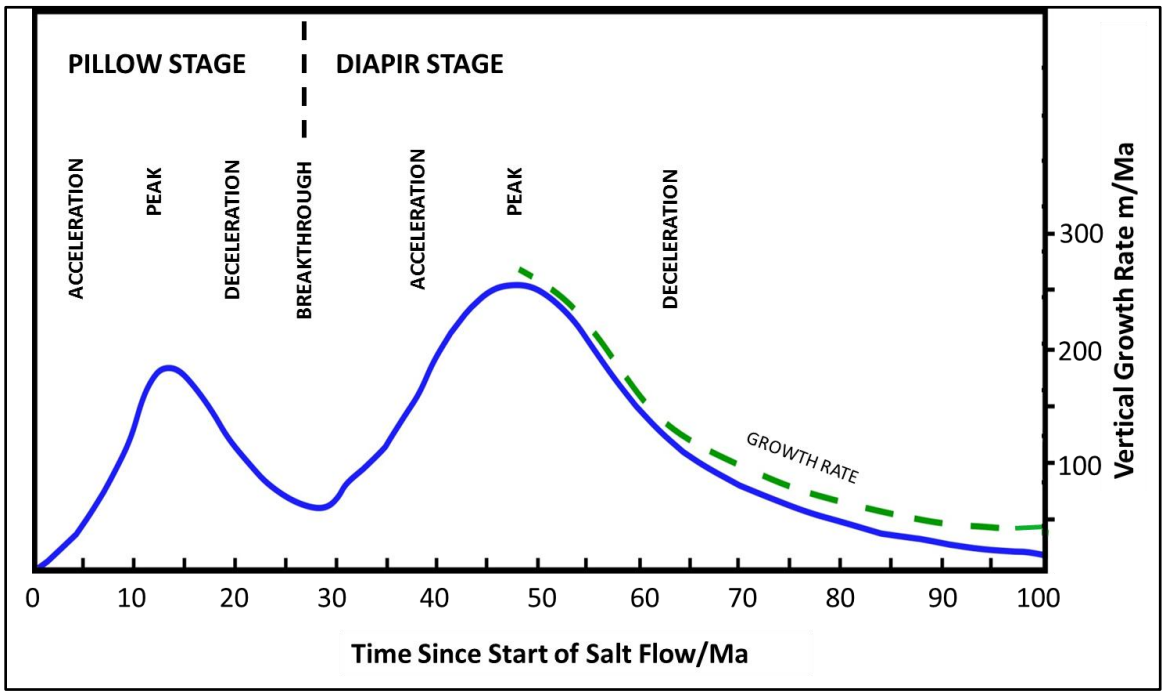

Figure 4.4: The dashed line above the solid line is the rate of growth for the salt domes of the Houston area modified from Pittman (1994) and compared to Jackson and Talbot (1986). The growth rates appear to be very similar. It shows that most salt domes in the Gulf Coast Region experienced similar cycles of growth (Modified from Pittman, 1994).

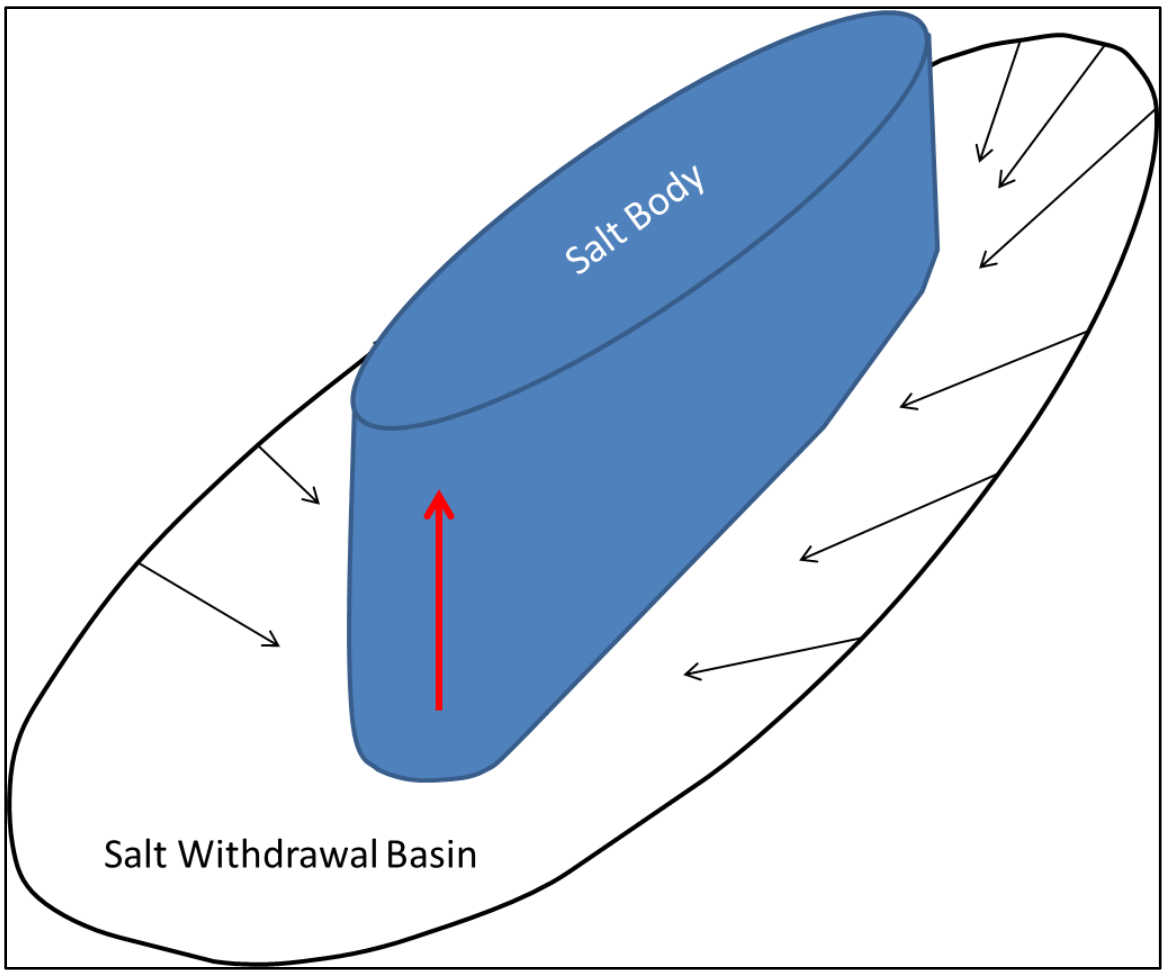

Figure 4.5: Cartoon of idealized formation of a primary salt withdrawal basin during the Pillow Stage in which large volumes of salt are extruded upward. The red arrow indicates direction of salt movement (Modified from Brewer & Kenyon, 1996).

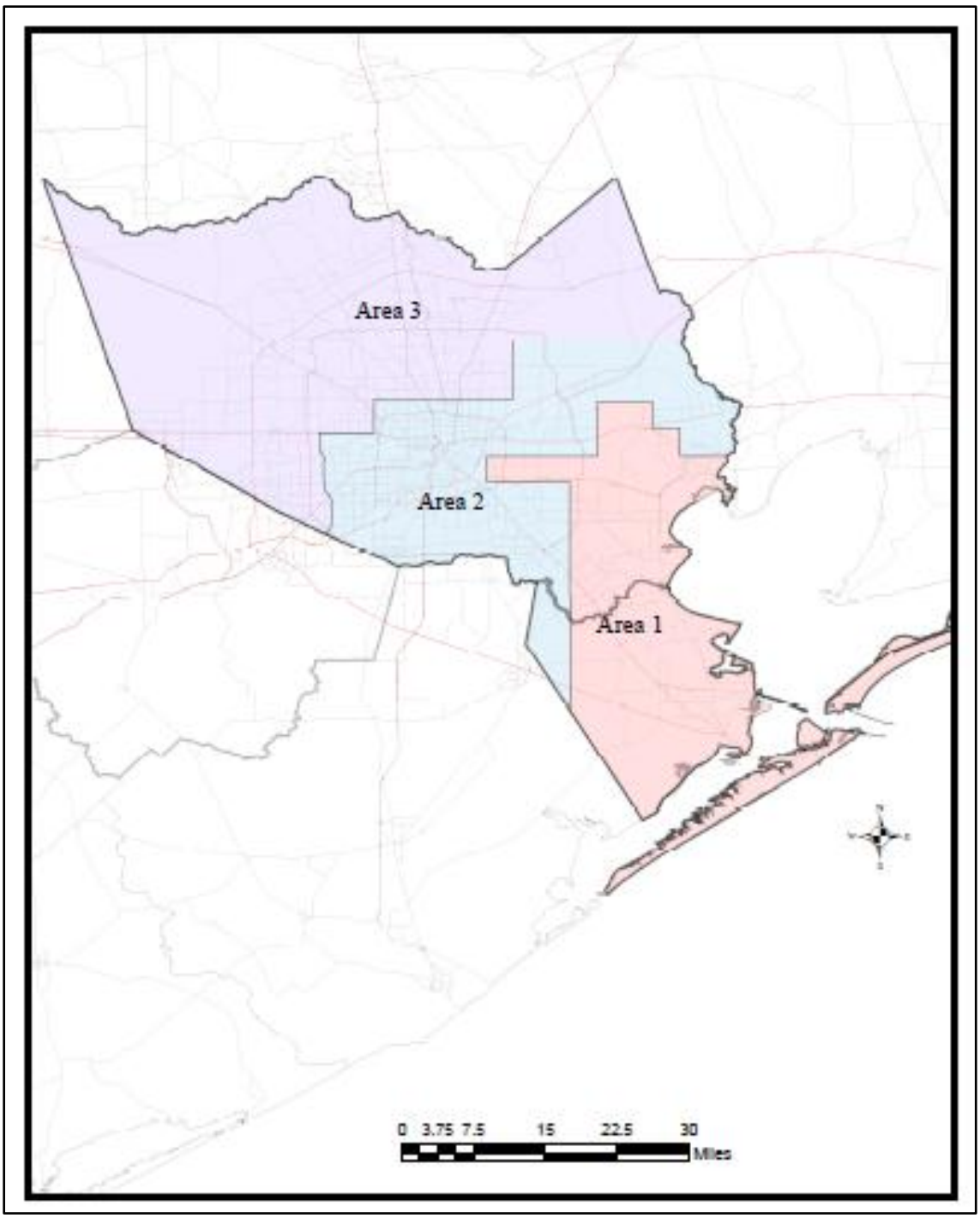

Figure 4.6: The three areas according to the HGSD 1999 Regulatory Plan (Harris-Galveston Subsidence District, 2012).

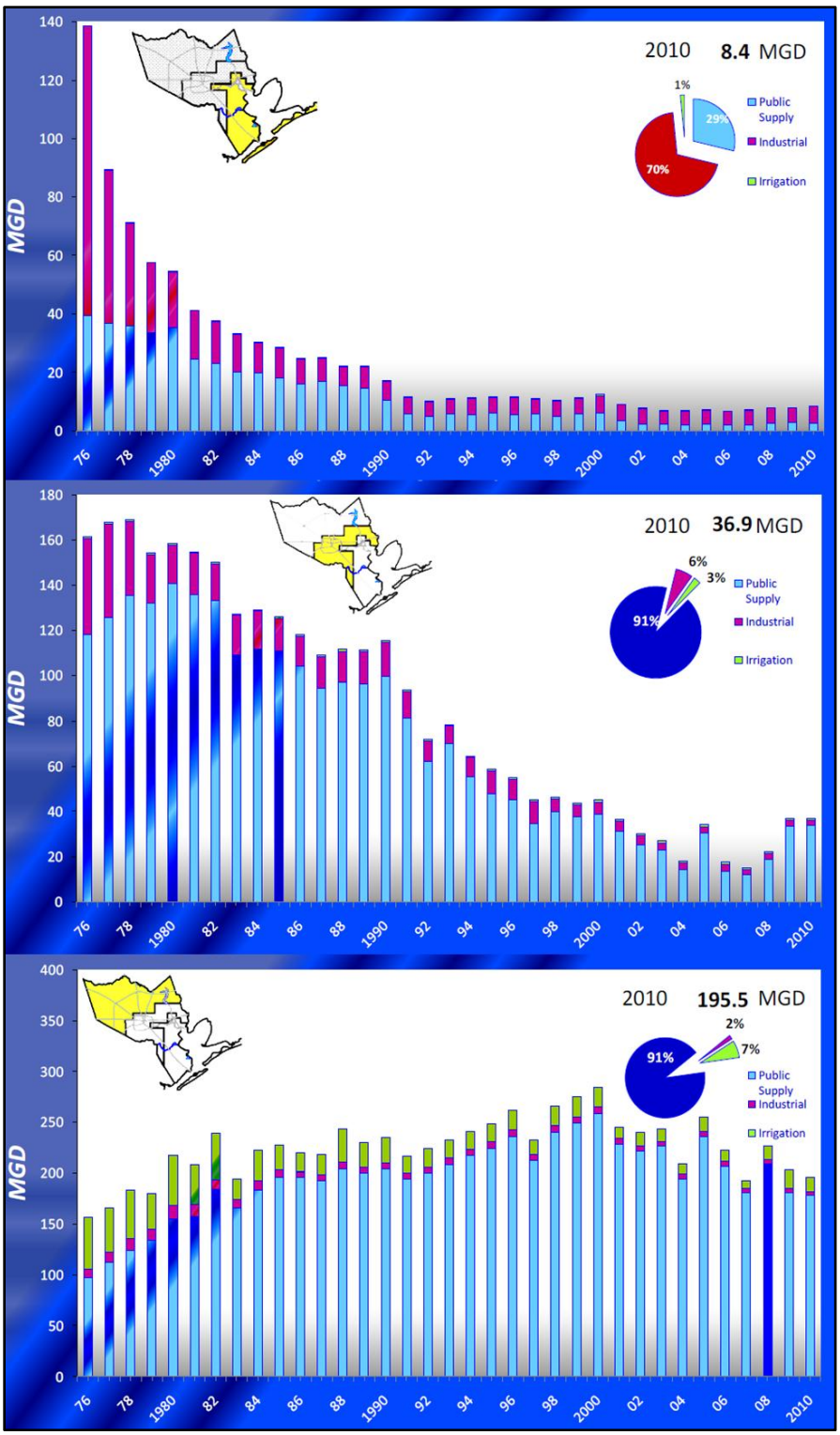

Figure 4.7: Groundwater withdrawal rates for areas one, two, and three in Harris-Galveston County. Withdrawal rates show steady decline for areas one and two. In area three withdrawal rates began to decline in 2000, but overall still remain high (Lackey, 2011).

4.3 LiDAR and DEM

The DEM polygon method results are qualitative at best. No quantitative analysis could be done due to the variable vertical accuracies of each year's DEM. Each salt dome showed a change in the difference between the central and outer polygon's mean elevation. This could represent uplift in the surface above the salt domes, subsidence of the surrounding area, or vice versa.

A much more detailed time lapse TLS scan was conducted on Pierce Junction salt dome. Results showed +6 cm of change in elevation in a seven-month period. This translates to 0.86 cm/month and 10.29 cm/yr. If that rate was caused by pure salt dome uplift, Pierce Junction would have one of the fastest non-breached salt movement rates in the world. This however is highly unlikely. A more reasonable reason for this increase of 6 cm could be the shrink-swell behavior of the soil-moisture active zone. This zone of expansive clays extends 4 to 6 m below the surface and responds to variations in rainfall and temperature. As much as 6 to 9 cm of vertical movement can occur within a few days (Zilkoski et al., 2003).

4.4 Gravity Patterns

Gravity differences observed in this study may be attributed to subsurface salt movement, changes in water level, or field acquisition procedures. If the salt is rising beneath Pierce Junction the increase in gravity difference noted in Figure 3.7 could represent a subsurface increase in salt within the center dome area. The 0.08 mGal difference between the two sets of surveys may show a uniform rise in the salt dome from the north, south, east, and west. The positive anomaly observed at Pierce Junction is

counter to most gravity readings above salt domes. However, the positive anomaly may be attributed to how close the Pierce Junction salt dome is to the surface. The change from negative to positive density contrast is demonstrated by Nettleton (1976) (Figure 4.8).

A simple simulation was conducted using GravMod version 3.2 created by Dr. Mark W. Hounslow of Lancaster University (http://geography.lancs.ac.uk/cemp/resources/software/gravmod.htm). GravMod is a simple software used for modeling Bouguer anomaly data. Density differences between sediments and the salt dome were obtained from previous works and measurements (Table 4.1). The salt measured in this work was from the Hockley salt dome (Figure 4.9). The overburden was a mixture of the Midway, Wilcox, Claiborne, Jackson, and Vicksburg Groups which range in age from Paleocene to Oligocene. The rock salts' purity was determined through bulk x-ray diffraction (XRD) (Figure 4.10). The percentages of halite (94 %) and anhydrite (1%) agree with percentages from Halbouty (1979) which were ~97 % for halite and ~3 % for anhydrite.

Two different density contrasts were assumed for the modeling. For the first model a density difference of 0.2 mGal was assumed between the overburden (2.2 g/cc) and the salt dome (2.0 g/cc) (Figures 4.11 and 4.12). The second model assumed a density difference of 0.09 mGal (Figures 4.13 and 4.14). Both sets of models showed that the differences observed between the May and September survey could be caused by changes in the distribution of subsurface mass (salt).

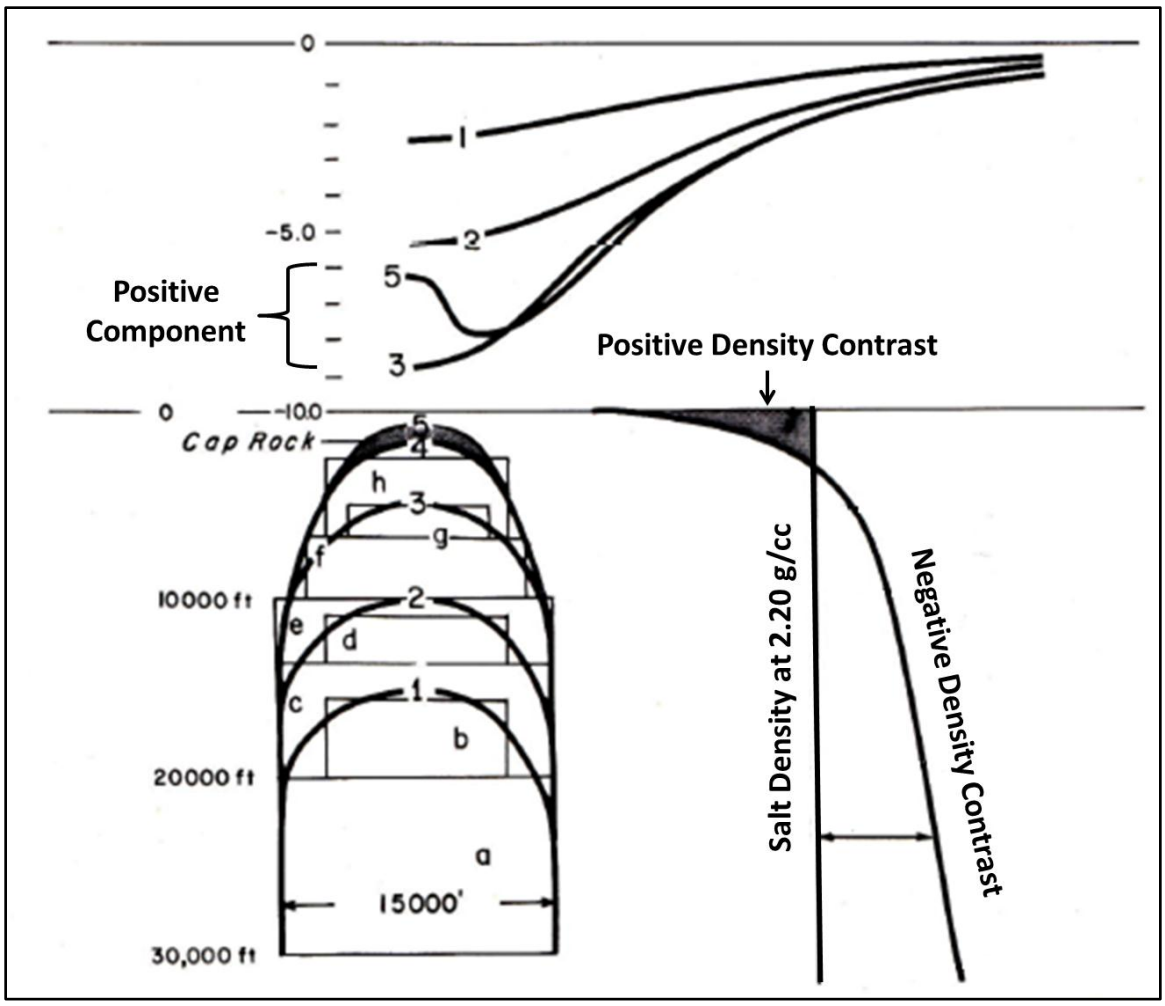

Figure 4.8: Illustration of typical gravity profiles from salt domes of varying depths. This demonstrates a negative to positive density contrast relative to how close the salt dome is to the surface (Modified from Nettleton, 1976).

Table 4.1: Densities of different rocks and minerals from Nettleton (1976), Seigel (1995), and measurements from this current study.

(Modified from Seigel, 1995)		
Type	**Range (g/cc)**	**Average (g/cc)**
Overburden (wet)		1.92
Soil (wet)	1.2–2.4	1.92
Clay (wet)	1.63–2.6	2.21
Gravel (wet)	1.7–2.40	2
Sand (wet)	1.70–2.30	2
Sandstone (wet)	1.61–2.76	2.35
Shale (wet)	1.77–3.20	2.4
Limestone (wet)	1.93–2.90	2.55
Dolomite (wet)	2.28–2.90	2.7
Sedimentary Rocks (wet average)		2.5
Rocksalt	2.1-2.6	2.22
Gypsum	2.2-2.6	2.35
Calcite	2.6-2.7	
Anhydrite	2.29-3.0	2.93
(Modified from Nettleton, 1976)		
Type	**Range (g/cc)**	**Average (g/cc)**
Unconsolidated Sediments	1.7-2.3	
Sandstones	2.0-2.5	
Salt (Pure Halite)	2.16	
Salt (Salt Dome)	2.2	
Limestone	2.5-2.7	
Average Crustal Rock		2.67
(Current work, 2012)		
Type	**Range (g/cc)**	**Average (g/cc)**
Overburden		2.66
Salt (Hockley salt dome)		2.22

Figure 4.9: A block of rock salt from the Hockley salt dome. A quarter is visible for scale.

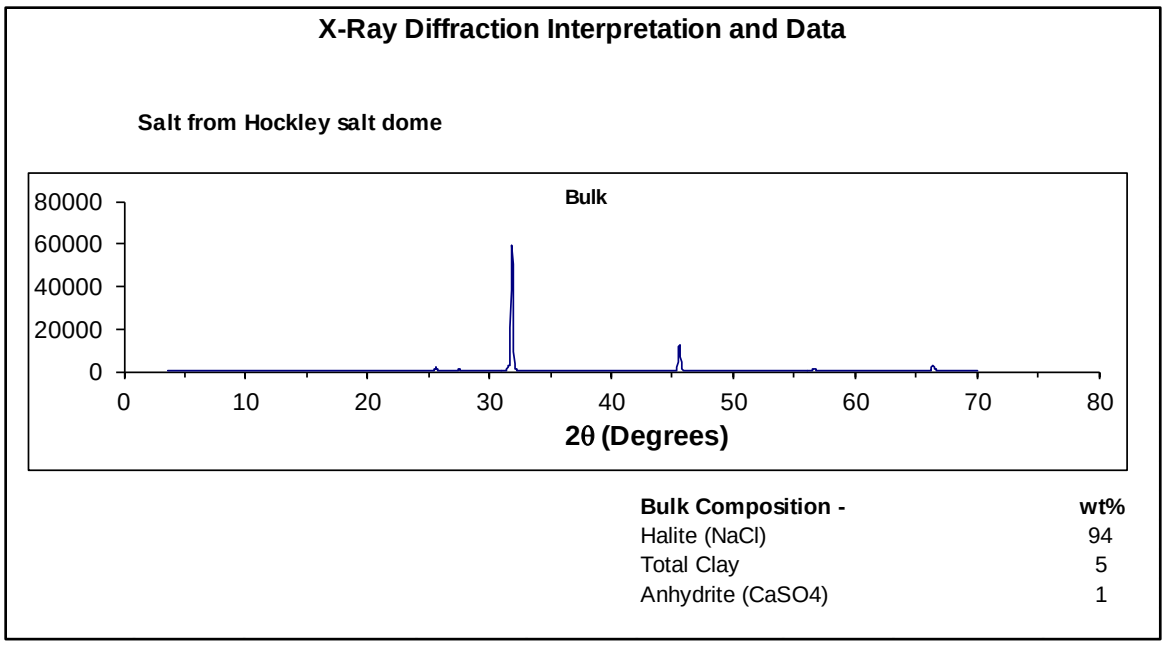

Figure 4.10: XRD diffractogram of salt from the Hockley salt dome. The percentages of Halite and Anhydrite agree with other published percentages for Gulf Coast salt domes of ~3 % Anhydrite and ~97 % Halite (Halbouty, 1979).

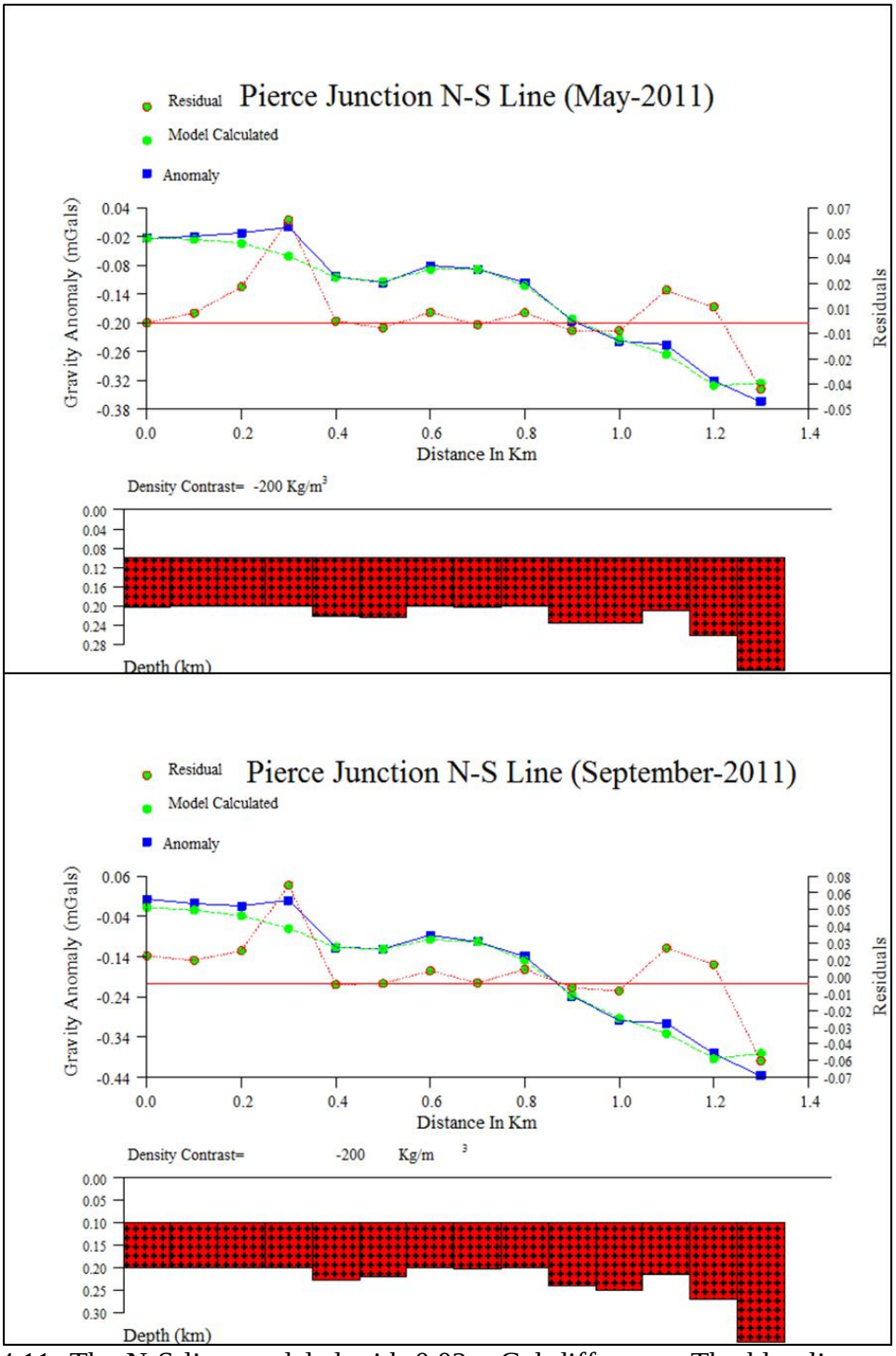

Figure 4.11: The N-S line modeled with 0.02 mGal difference. The blue line represents the observed Bouguer anomalies, the green line is calculated gravity from modeling, and the red line with yellow dots is residuals between the observed and calculated gravity values. The red bars are objects with different density then the surroundings.

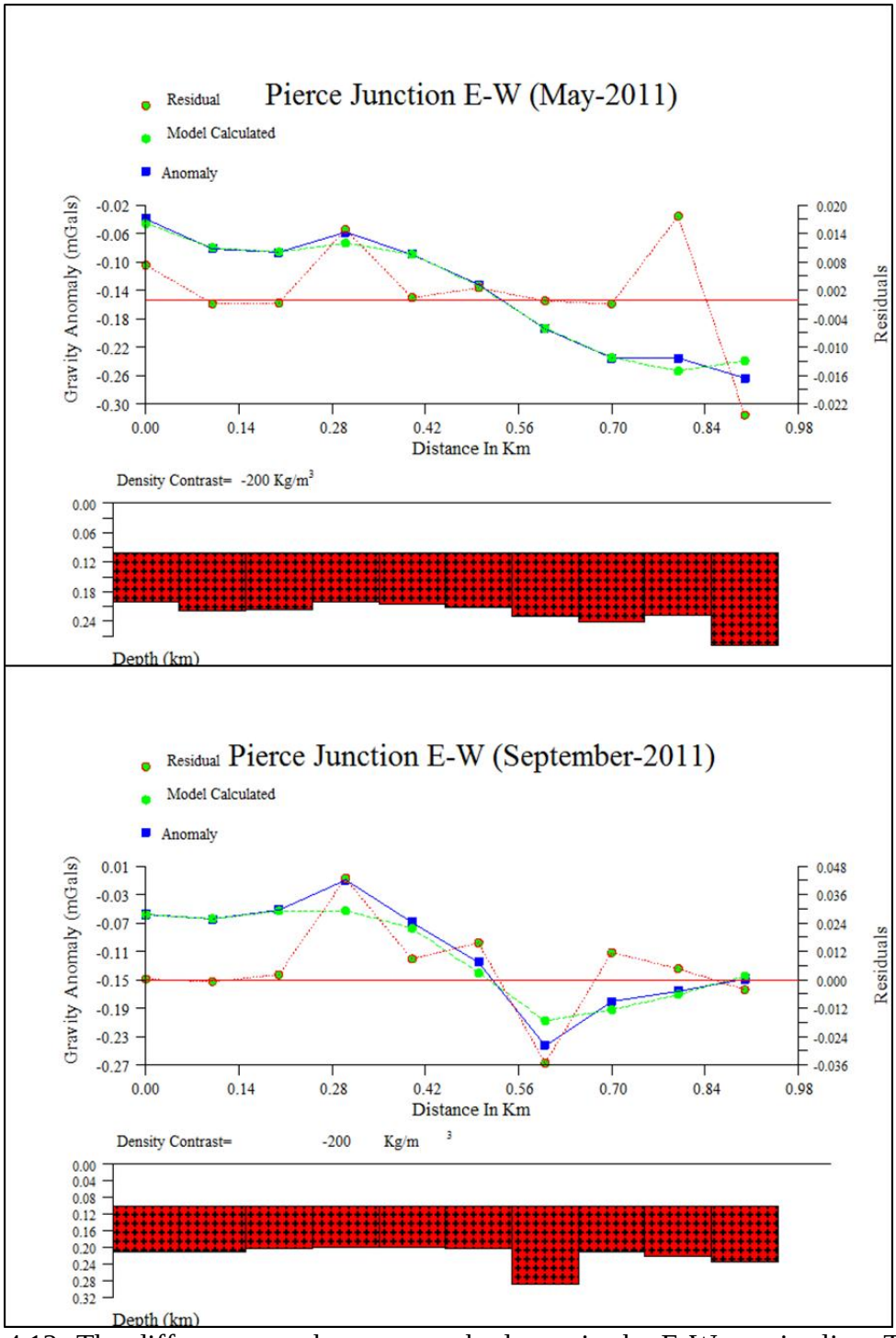

Figure 4.12: The difference can be seen much clearer in the E-W gravity line. The red bars in the September survey are larger which may signify increased subsurface mass (salt).

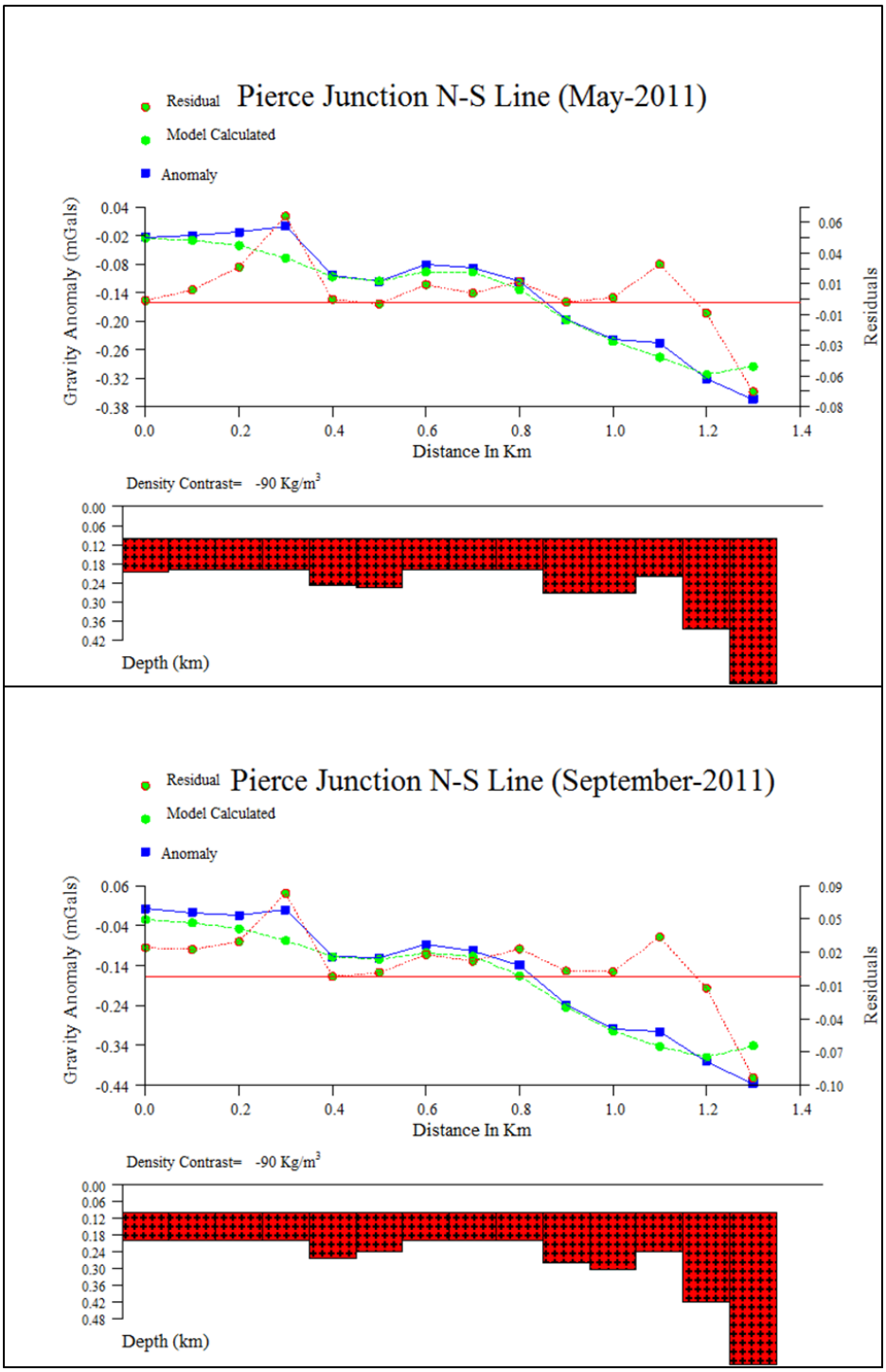

Figure 4.13: Gravity modeling of N-S line with 0.09 mGal difference. The differences in the red bars between May and September surveys are much more noticeable then figure 4.11. The smaller gravity difference means more salt movement is required to produce the different gravity readings.

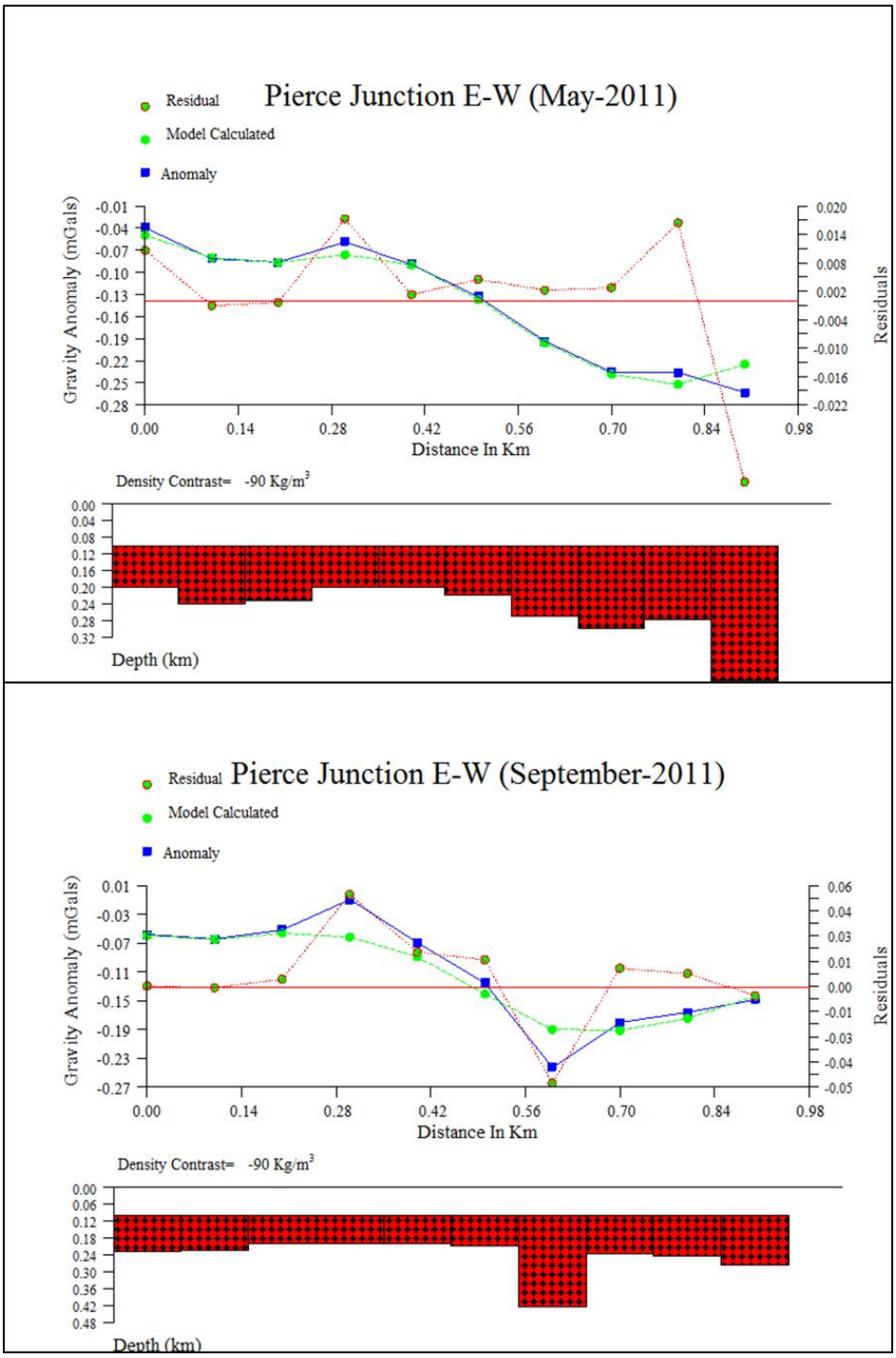

Figure 4.14: Gravity modeling of E-W line with 0.09 mGal of difference. Compared to figure 4.12 the red bars show much more difference.

Changes in water levels can have an influence on the density of the near-surface layer which can in turn influence gravity readings (Völgyesi & Tóth, 2005). A long period of drought followed by weeklong rain in the study area could have changed the water level enough to give the difference in readings.

The last possibility for the difference in gravity readings may be due to variability in the field acquisition. The exact location of the previous survey may not have been measured. Measurements could have varied by ±10–50 cm in any direction of the previous survey. This may be attributed to the choice of relative small survey markers (MAG NAILS) and stability of the surface for leveling the gravimeter. This slight variation in measurement locations should not affect the readings as much but never-the-less should be considered when examining the results.

Chapter 5 **Conclusion**

Gravity, GPS, and LiDAR are all powerful tools. The GPS data documented subsidence in the northwest and uplift in the southeast in the Houston area. The DEM derived from LiDAR documented elevation changes within the salt domes relative to their surroundings. TLS measured an increase of 6 cm over a section of Pierce Junction. Gravity detected a range of change of 0.08 mGal over Pierce Junction. These changes detected from gravity, GPS, and LiDAR could suggest salt movement, possibly the result of secondary salt withdrawal through continued diapirism.

Although salt withdrawal and salt diapirism could cause all the observed results another significant factor comes into question: groundwater. Groundwater withdrawal has been targeted as one of the main causes of subsidence in the Houston area (Coplin & Galloway, 1999). This extremely impactful anthropogenic factor may overshadow most if not all natural surface deformation in the greater Houston area such as from salt movement.

Chapter 6 **Recommendations**

I believe the best to best way to observe and quantify the influence of salt on surface deformation is through continued measurements. A period of 5, 10, or possibly 15 years of continued GPS, LiDAR, and gravity measurements may reveal more conclusive results.

For GPS the best method would be to install permanent GPS stations above the center of a salt dome and one GPS station outside of the salt dome. Through continuous monitoring seasonal variations from the near-surface could be identified and removed which may reveal actual salt dome movement. Additionally repeated TLS and gravity scans over the entire dome could give a better idea on whether there is uniform movement in the subsurface and how that is expressed on the surface.

This campaign could be incorporated into a graduate level class in which every year a group of students can conduct surveys as an exercise. After a period of time a graduate student could analysis the collected data as a possible masters thesis project.

References

Bird, D., Burke, K., Hall, S. & Casey, J., 2005. Gulf of Mexico tectonic history: Hotspot tracks, crustal boundaries, and early salt distribution. *AAPG Bulletin,* Volume 89, pp. 311-328.

Boyd, T. M., 2003. *Introduction to Geophysical Exploration.* [Online]
Available at: http://galitzin.mines.edu/INTROGP/
[Accessed December 2010].

Brandes, C. et al., 2012. Basin modelling of a lignite-bearing salt rim syncline: Insights into rim syncline evolution and salt diapirism in NW Germany. *Basin Research,* Volume 24, pp. 1-18.

Brewer, R. C. & Kenyon, P., 1996. Balancing salt dome uplift and withdrawal basin subsidence in cross-section. *Jounal of Structural Geology,* 18(4), pp. 493-504.

Brown, L. J. et al., 1974. *Natural hazards of the Texas coastal zone.* First ed. Austin, Texas: Bureau of Economic Geology.

Campbell, M. D. & Campbell, M. D., 2009. *Growth Faulting in the Houston, Texas Area: Origins, Relationships, Geologic Hazards, Impacts, and Methods of Investigation (Draft).* [Online]
Available at: www.ela-iet.com/DraftFaultpaperFullColumn022604NEW.pdf
[Accessed October 2011].

Coplin, L. & Galloway, D. L., 1999. Houston-Galveston, Texas: Managing coastal subsidence. In: D. L. Galloway, D. R. Jones & S. E. Ingebritsen, eds. *Land subsidence in the United States.* s.l.:U.S. Geological Survey Circular 1182, pp. 35-48.

Deussen, A., 1934. Oil-producing horizons of gulf coast in Texas and Louisiana. *American Association of Petroleum Geologist Bulletin,* 18(4), pp. 500-518.

Deussen, A. & Lane, L. L., 1926. Hockley salt dome, Harris County, Texas. In: R. C. Moore, et al. eds. *Geology of Salt Dome Oil Fields.* Tulsa, Oklahoma: American Association of Petroleum Geologists, pp. 570-599.

Dodge, M. M. & Posey, J. S., 1981. *Structural cross sections, Tertiary formations, Texas Gulf Coast.* Austin, Texas: Bureau of Economic Geology, University of Texas at Austin.

Eby, J. B., 1945. Geophysical history of south houston salt dome and oil field, Harris County, Texas. *American Association of Petroleum Geologists Bulletin,* 29(2), pp. 210-214.

Engelkemeir, R. E., Khan, S. & Burke, K., 2010. Surface deformation in Houston, Texas using GPS. *Tectonophysics,* Volume 490, pp. 47-54.

Engelkemeir, R. & Khan, S. D., 2008. LiDAR mapping of faults in Houston, Texas, USA. *Geosphere,* 4(1), pp. 170-182.

Ewing, T. E., 1991. Structural framework. In: A. Salvador, ed. *The Gulf of Mexico Basin.* Boulder, Colorado: Geological Society of America, pp. 31-52.

Ewing, T. E. & Lopez, R. F., 1991. Principal structural features, Gulf of Mexico Basin. In: A. Salvador, ed. *The Gulf of Mexico Basin.* Boulder, Colorado: Geological Society of America, p. plate 2.

Fernandez, J., 2007. *Scientific Applications of the Mobile Terrestrial Laser Scanner (M-TLS) System.* s.l.:M.S. Thesis, Univeristy of Florida.

Firuzabadi, D. & King, R. W., 2011. GPS precision as a function of session duration and reference frame using Multi-point software. *GPS Solutions,* 16(2), pp. 191-196.

Fourie, C. J. S., 1998. Spreadsheet reductions of gravity data. *Computers & Geosciences,* 24(5), pp. 495-499.

Fowler, R., 2001. Topographic LiDAR. In: D. F. Maune, ed. *Digital Elevation Model Technologies and Applications: The DEM Users Manual.* Bethesda, Maryland: American Society for Photogrammetry and Remote Sensing, pp. 207-236.

Gabrysch, R. K., 1984. Case History No. 9.12. The Houston-Gavlestion Region, Texas, U.S.A.. In: J. F. Poland, ed. *Guidebook to studies in land subsidence due to ground-water withdrawal.* Chelsea, Michigan: United Nations Educational, Scientific, and Cultural Organization, pp. 253-262.

Ge, H., Jackson, M. P. A. & Vendeville, B. C., 1997. Kinematics and Dynamics of Salt Tectonics Driven by Progradation. *American Association of Petroleum Geologists Bulletin,* 81(3), pp. 398-423.

Halbouty, M. T., 1979. *Salt Domes, Gulf Region, United States and Mexico.* Second Edition ed. Houston, Texas: Gulf Publishing Company.

Hammer, S., 1943. Note on the variation from equator to pole on the Earth'sgravity. *Geophysics,* 8(1), pp. 57-60.

Hanna, M. A., 1934. Geology of the Gulf Coast salt domes: Part IV. Relations of petroleum accumulation to structure. In: W. E. Wrather & F. H. Lahee, eds. *Problems of Petroleum Geology.* Tulsa, Oklahoma: American Association of Petroleum Geologists, pp. 629-678.

Harris-Galveston Coastal Subsidence District & Espey, Huston & Associates Inc., 1981. *Water Resource Management Program Phase I,* Friendswood, Texas: The District.

Harris-Galveston Subsidence District, 1999. *www.hgsubsidence.org.* [Online] Available at: http://www.hgsubsidence.org/documents/regulatory.html [Accessed March 2012].

Harris-Galveston Subsidence District, 2012. *www.subsidence.org.* [Online] Available at: http://mapper.subsidence.org/ [Accessed March 2012].

Holzer, T. L., 1984. Ground failure induced by ground-water withdrawal from unconsolidated sediment. In: T. L. Holzer, ed. *Man-induced Land Subsidence.* Boulder, Colorado: Geological Society of America, pp. 67-105.

Holzer, T. L. & Gabyrsch, R. K., 1987. Effect of water-level recoveries on fault creep, Houston, Texas. *Ground Water,* 25(4), pp. 392-397.

Hudec, M. R. & Jackson, M. P. A., 2007. Terra infirma: Understanding salt tectonics. *Earth-Science Reviews,* 82(1-2), pp. 1-28.

Hudec, M. R., Jackson, M. P. A. & Schultz-Ela, D. D., 2009. The paradox of minbasin subsidence into salt: Clues to the evolution of crustal basins. *Geologial Society of America Bulletin,* 121(1/2), pp. 201-221.

Huffman, A. C. et al., 2004. Salt Diapirs in the Gulf Coast. *U.S. Geological Survey, DS-90, version 1.0.*

Jackson, M. P. A. & Seni, S. J., 1983. Geometry and evolution of salt structures in a marginal rift basin of the Gulf of Mexico, East Texas. *Geology,* Volume 11, pp. 131-135.

Jackson, M. P. A. & Talbot, C. J., 1986. External shapes, strain rates, and dynamics of salt structures. *Geological Society of America Bulletin,* Volume 97, pp. 305-323.

Jackson, M. P. A. & Vendeville, B. C., 1994. Regional extension as a geologic trigger for diapirism. *Geological Society of America Bulletin,* 106(1), pp. 57-73.

Jet Propulsion Laboratory, 2008. *Under the Hood.* [Online] Available at: http://apps.gdgps.net/apps_underhood.php [Accessed November 2011].

Kupfer, D. H., 1974. Environment and intrusion of Gulf Coast salt and its probable relationship to plate tectonics. *In Fourth Symposium on Salt, Cleveland, Ohio. Northern Ohio Geological Society*, pp. 197-213.

Lackey, M. G., 2011. *Annual Groundwater Report, 33rd annual report*, s.l.: Harris-Galveston Subsidence District, 147 p..

Lazio, P., 2011. Editing RINEX Files to fix a poor OPUS run. In: T. Soler, ed. *CORS and OPUS for Engineers.* Reston, Virginia: American Society of Civil Engineers, pp. 62-66.

Meyer, W. B., 2002. Allison's aftermath. *Point of Begining*, July, p. 4.

Minor, H. E., 1925. Goose Creek Oil Field, Harris County, Texas. *American Association of Petroleum Geologists,* Volume 9, pp. 286-297.

Moritz, H., 1992. Geodetic reference system 1980. *Bulletin Géodésique,* 66(2), pp. 187-192.

Morris, M. & Fowler, T., 2011. *Natural Gas Plant Burns in Mont Belvieu.* [Online]
Available at: http://www.chron.com/news/houston-texas/article/Natural-gas-plant-burns-in-Mont-Belvieu-1692771.php
[Accessed January 2012].

Murray, G. E., 1957. Geologic occurrence of hydrocarbons in gulf coastal province of the United States. *Gulf Coast Association of Geological Societies Transactions,* Volume 7, pp. 253-299.

National Geodetic Survey, 2012a. *Continuously Operating Reference Station (CORS).* [Online]
Available at: http://geodesy.noaa.gov/CORS/
[Accessed November 2011].

National Geodetic Survey, 2012b. *Accuracy.* [Online]
Available at: http://geodesy.noaa.gov/OPUS/about.jsp#accuracy
[Accessed November 2011].

Nettleton, L. L., 1976. *Gravity and Magneetics in Oil Prospecting.* USA: McGraw-Hill Inc..

Norman, C. & Howe, R. G., 2011. Impact of active faults on land-based engineered structures in the Gulf Coastal Zone. Houston, Texas, AAPG Annual Convention & Exhibition.

O'Neill, M. W. & Van Siclen, D. C., 1984. Activation of Gulf Coast faults by depressuring of aquifers and an engineering approach to siting structures along

their traces. *Bulletin of the Assocation of Engineering Geologists*, 21(1), pp. 73-87.

Optech Inc., 2006. *ILRIS Summary Specification Sheet.* [Online] Available at: http://www.optech.ca/pdf/ILRIS_SpecSheet_110309_Web.pdf [Accessed 2010].

Otoum, M. A., 2011. *An Integrated Geophysical Investigation to Map the Hockley Active Fault in Northwest Harris County, Texas.* Houston, Texas: Master Thesis, University of Houston.

Pepe, W. & Coutu, G., 2008. Beach morphology change study using ArcGIS spatial analyst. *Middle States Geographer,* Volume 41, pp. 91-97.

Pittman, D. W., 1994. *Growth History and Structural Analysis of Sugarland Dome, Fort Bend County, Texas.* Houston, Texas: Master Thesis, University of Houston.

Riegl Laser Measurement Systems, 2011. *Riegl VZ-400 Datasheet.* [Online] Available at: http://riegl.com/uploads/tx_pxpriegldownloads/10_DataSheet_VZ400_12-09-2011.pdf [Accessed January 2012].

Salvador, A., 1987. Late Triassic-Jurassic paleogeography and origin of Gulf of Mexico basin. *American Association of Petroleum Geologists Bulletin,* 71(4), pp. 419-451.

Salvador, A., 1991a. Introduction. In: A. Salvador, ed. *The Gulf of Mexico Basin.* Boulder, Colorado: Geological Society of America, pp. 1-12.

Salvador, A., 1991b. Triassic-Jurassic. In: A. Salvador, ed. *The Gulf of Mexico Basin.* Boulder, Colorado: Geological Society of America, pp. 131-180.

Sasaki, H., Mukoyama, N. & Namikawa, K., 2008. *Digital TerAnalysis Using Airborne Laser Scanner (LIDAR) Data for Natural Hazard Assessment.* Beijing, China, The International Archives of the Photogrammetry, Remote Sensing and Spatial Information Sciences. Vol. XXXVII. Part B8. pp. 1225-1228..k

Seigel, H. O., 1995. *A Guide to High Precision Land Graivmeter Surveys.* Concord, Ontario: Scintrex Limited.

Shah, S. D. & Lanning-Rush, J., 2005. Principal Faults in the Houston, Texas, Metropolitan Area. *U.S.Geological Survey Scientific Investigations Map 2874.*

Shrestha, R. L. et al., 1999. Airborne laser swath mapping: Accuracy assessment for surveying and mapping applications. *Journal of Amerian Congress on Surveying and Mapping,* 59(2), pp. 83-94.

Sorensen, K., 1986. Rim syncline volume estimation and salt diapirism. *Nature,* Volume 319, pp. 23-27.

Teas, L. P., 1935. Natural gas of Gulf Coast salt-dome area. In: *Geology of Natural Gas.* Tulsa , Oklahoma: America Accociation of Petroleum Geologists, pp. 683-740.

Trimble Navigation Limited, 2002. *Trimble Geomatics Office User Guide.* Version 1.6 ed. Dayton, Ohio: Trimble Navigation Limited.

Trusheim, F., 1960. Mechanism of salt migration in northern Germany. *American Association of Petroleum Geologists,* 44(9), pp. 1519-1540.

U.S. Census Bureau, 2010. *U.S. Census Bureau Delivers Texas' 2010 Census Population Totals, Including First Look at Race and Hispanic Origin Data for Legislative Redistricting.* [Online]
Available at: http://2010.census.gov/news/releases/operations/cb11-cn37.html
[Accessed October 2011].

UNAVCO, 2010. *UNAVCO Knowledgebase - Trimble 4700/5700/R7 - How to execute a real-time kinematic (RTK) survey from start to finish.* [Online]
Available at: http://facility.unavco.org/kb/questions/617/
[Accessed May 2010].

Verbeek, E., Ratzlaff, K. & Clanton, U., 1979. *Faults in parts of north-central and western Houston metropolitan area, Texas,* s.l.: U.S. Geological Survey Miscellaneous Field Studies Map, MF-1136.

Verbeek, E. R. & Clanton, U. S., 1978. *Map showing faults in the southeastern Houston metropolitan area, Texas,* s.l.: U.S. Geological Survey Open File Report 78-79.

Walper, J. L., 1980. Tectonic evolution of the Gulf of Mexico. In: R. H. Pilger Jr., ed. *The Origin of the Gulf of Mexico and the Early Opeining of the Central North Atlantic Ocean.* Baton Rouge, Louisiana: Louisiana State University, pp. 87-98.

Wang, G. & Soler, T., 2012. OPUS for horizontal subcentimeter-accuracy landslide monitoring: A case study in the Puerto Rico and Virgin Islands region. *Journal of Surveying Engineering,* Issue posted ahead of print January 2, 2012.

Wehr, A. & Lohr, U., 1999. Airborne Laser Scanning - An introduction and overview. *ISPRS Journal of Photogrammetry and Remote Sensing,* Volume 54, pp. 68-82.

White, S. A. & Wang, Y., 2003. Utilizing DEMs derived from LIDAR data to analyze morphologic change in the North Carolina coastline. *Remote Sensing of Environment,* Volume 85, pp. 39-47.

White, W. & Morton, R., 1997. Wetland losses related to fault movement and hydrocarbon production, Southeast Texas. *Journal of Coastal Research*, 13(4), pp. 1305-1320.

Zilkoski, D. et al., 2003. *The Harris-Galveston Coastal Subsidence District/National Geodetic Survey Automated GPS Subsidence Monitoring Project.* Proceedings of the U.S.Geological Survey Subsidence Interest Group Conference, OFR 03-308.